



Université Grenoble Alpes

Report

Mid-term

MIRA Anna

Supervisors:

Yohan Payan, TIMC-IMAG Lab, CNRS & Univ. Grenoble Alpes
Serge Muller, GE-Healthcare, France
Ann-Katherine Carton, GE-Healthcare, France

V2

Buc, 2017

CONTENTS

Contents	iii
List of Symbols	vii
5 General Problem statement	1
Technical approach	2
Thesis overview	3
Software	4
Ethics	5
10 1 Clinical background	7
1.1 Breast anatomy	8
1.1.1 Breast embryogenesis	8
1.1.2 Breast external appearance	9
1.1.3 Internal structures	10
1.1.4 Adult breast texture changes	13
15 1.2 Breast Cancer	14
1.2.1 Cancer classification	15
1.2.2 Breast cancer screening	16
20 1.3 Medical imaging	16
1.3.1 X-ray mammography	17
1.3.2 Ultrasounds	18
1.3.3 Magnetic resonance imaging	19
1.4 Conclusion	19
Report	iii

CONTENTS

2 Biomechanical breast modeling	21
25 <i>State of the art</i>	
2.1 Continuous mechanics	22
2.1.1 Deformation and strain	22
2.1.2 Stress measures	26
2.1.3 Conservation equations	28
30 2.1.4 Constitutive models	30
2.2 Finite Element Discretization	33
2.2.1 Eulerian and Lagrangian mesh description	33
2.2.2 Lagrangian mesh	34
35 2.3 Contact mechanics	37
2.3.1 Contact interface equations	38
2.3.2 Surface interaction models	39
2.3.3 Contact formulation algorithm: pure penalty model	40
40 2.4 Breast biomechanical model: overview	43
2.4.1 Breast reference configuration	43
2.4.2 Constitutive models	45
2.4.3 Boundary conditions	49
45 2.4.4 Summary	49
3 A new biomechanical breast model evaluated on real data	52
45 3.1 Geometry extraction	53
3.1.1 Data acquisition	53
3.1.2 Image segmentation	54
3.1.3 Image registration	55
3.1.4 Patient-specific 3D geometry	56
50 3.2 Finite Elements Mesh	57
55 3.3 Breast reference configuration	59
55 3.4 Boundary conditions	60
55 3.5 Materials constitutive models	63
55 3.5.1 Model simplification	63
55 3.5.2 Estimation of the optimal constitutive parameters	66
55 3.6 Model validation	69
55 3.7 Discussions and conclusion	70
4 Breast Compression	73
60 <i>State of the art</i>	
4.1 Mammographic positioning	74
4.2 Paddles designs	75
4.3 Compression mechanics	76
4.4 Compression quality metrics	78
4.4.1 Image quality	79
4.4.2 Average glandular dose	80

65	4.4.3 Pain and discomfort	81
	4.5 Summary	82
5	Breast compression & comfort	
	<i>A comparative study</i>	85
70	5.1 Breast compression modeling	86
	5.1.1 FE modeling of compression paddles	86
	5.1.2 Breast compression mechanics	87
	5.1.3 Updated material constitutive models	89
	5.2 Simulation of digital images	90
75	5.3 Compression quality metrics	93
	5.3.1 Patient comfort	93
	5.3.2 Image quality	93
	5.3.3 Average glandular dose	93
	5.4 Results	94
	5.5 Discussions and conclusion	99
80	Conclusion	101
	Key contributions	102
	Perspective	103
	Appendices	105
	A Distance measures	106
85	B Mesh Convergence	108
	C Boundary conditions <i>contact models</i>	110
	Bibliography	113

LIST OF SYMBOLS

α	multiplicative regularization factor
λ	Young's moduli
λ_{xx}	Youngs's moduli of the material xx
$\lambda_{xx}^{l/r}$	Young's modulus of the material xx for the left/right breast
\mathcal{B}	Body
μ	shear moduli
ν	Poisson ratio
Ω	Domain occupied by the body
Ω_0	Reference body configuration
Ω_1	Current or analyzed body configuration
D_i	position difference of the node i between the estimated and measured breast prone configurations
F	Deformation gradient
J	Jacobian determinant of the deformation gradient tensor
l	body stretch
m	Body mass
p	Particle or material point

CONTENTS

- u* Particle displacement
X Point position on the reference configuration
₁₁₀ *x* Point position on the current configuration
AEC automatic exposure control
AGD Average Glandular Dose
AOP automatic optimization of parameters
DgN normalized dose
₁₁₅ FDA Food and Drug Administration
FE Finite Element
FFDM Full Field Digital Mammography
GBM generalized momentum balance
ILC Invasive lobular carcinoma
₁₂₀ IQ Image Quality
K Bulk moduli
LIQ Lower Inner Quadrant
LOQ Lower Outer Quadrant
MRI Magnetic Resonance Imaging
₁₂₅ NRS numerical rating scale
PDE partial differential equations
RF Radio-Frequency waves
SFP standard flex paddles
SRP standard rigid paddle
₁₃₀ SWE Shear-Wave Elastography
UIQ Upper Inner Quadrant
UOQ Upper Outer Quadrant
US Ultrasound

CONTENTS

VAS visual analogue scale

¹³⁵ VRS verbal rating scale

GENERAL PROBLEM STATEMENT

Today, mammography is the primary imaging modality for breast cancer screening and plays an important role in cancer diagnosis. Subtle soft-tissue findings and microcalcifications that may represent early breast cancer are visualized by means of X-rays images.
140 After investigation, the abnormal findings are taken in charge for further evaluation. A standard mammographic protocol always includes breast compression prior to image acquisition. Women breast is compressed between two plates until a nearly uniform breast thickness is obtained. The breast flattening improves diagnostic image quality¹ and reduces the absorbed dose of ionizing photons². However, the discomfort and pain produced by this procedure sometimes might deter women from attending breast screening by mammography³. Fleming et al⁴ show in a study of 2500 women that 15% of those who skipped the second appointment cited an unpleasant or painful first mammogram. Nowadays, the European Commission recommends a force standardized breast compression, i.e. the compression stops at a level of force just below the subjects pain threshold or to the maximum setting of the machine (not to exceed 200 N). Some research⁵ indicates that with a reduced level of compression (10N vs 30N), 24% of women did not experience a difference in breast thickness. If breast thickness is not reduced when compression force is applied, then discomfort is increased with no benefit in image quality. An important improvement
150 concerning the patient comfort could be achieved with the emergence of Full-Field Digital Mammography (FFDM). Several studies have shown that digital mammography is better in terms of image quality^{6,7} and radiation dose^{2,8} than FilmScreen Mammography (FSM). Therefore, there is an opportunity to leverage the potential of the recent imaging technologies to investigate alternative breast compression techniques, considering the patient comfort in addition to an improved image quality and a reduced ionizing radiation dose.
160 The aim of this work is to develop and evaluate a biomechanical Finite Element (FE) breast model allowing to investigate alternative breast compression strategies.

TECHNICAL APPROACH

- ¹⁶⁵ Several studies showed that, the pain experienced by women during the mammographic exam depends on psychologic factor (Aro et al., 1996) (technician behavior, patient anxiety), sociologic factors (Dullum et al., 2000) (ethnicity, education level) as well as physiologic (Poulos et al., 2003) factors (compression level, breast size). Here, the psychologic and sociologic factors are neglected. The study focuses on physiological factors as the compression force or structural specifications of the compression paddle to characterize the patient comfort.
- ¹⁷⁰

THESIS OVERVIEW

SOFTWARE

ETHICS

1

CLINICAL BACKGROUND

¹⁸⁰ In France, in 2012, approximately 1.2 million new cases were diagnosed, and 400,000 women died from breast cancer. Early detection of cancer is a major condition to a fast and full recovery from breast cancer. Today, mammography is by far the primary imaging modality for breast cancer screening and plays an important role in cancer diagnosis. However, frequently this experience is described by women as unpleasant and sometimes painful.

¹⁸⁵ The aim of this chapter is to provide the required clinical background on breast cancer screening and diagnosis for a good understanding of the global aim and relevance of the present work.

¹⁹⁰ First the breast evolution from early to the adult ages is described, with a detailed characterization of internal and external adult breast structures. To explain the intra-individual variation of breast mechanical and structural properties, the hormonal changes during the menstrual cycle, pregnancy or menopause are presented. Next the cancer edogenesis is described and the most common types are characterized. Finally, different modalities for breast imaging are presented with their underlying technical principals as well as their utilization and relevance for breast cancer regular screening.

195 1.1 Breast anatomy

Internal and external breast structures will be repeatedly referenced in the following work, therefore their detailed description including mechanical properties and their localization is needed. Although the breast anatomy seems to be simple and easy to understand, a detailed analysis of breast embryogenesis is requested for a better localization the supporting 200 breast tissues. The breast support matrix is a structure of high interests when modeling breast mechanics.

1.1.1 Breast embryogenesis

The breast is a modified skin gland which starts to develop at the embryonic stage from the epidermis and dermis. During the sixth fetal month, from 12 to 20 solid cords of epithelial 205 cells are growing down into the dermis (Figure. 1.1.a-b). Later, these cords evolve into lactiferous ducts and alveoli (fig. 1.1.c-d). Thus, near birth, a simple network of branching ducts is already developed in the pectoral area (Skandalakis, 2009).

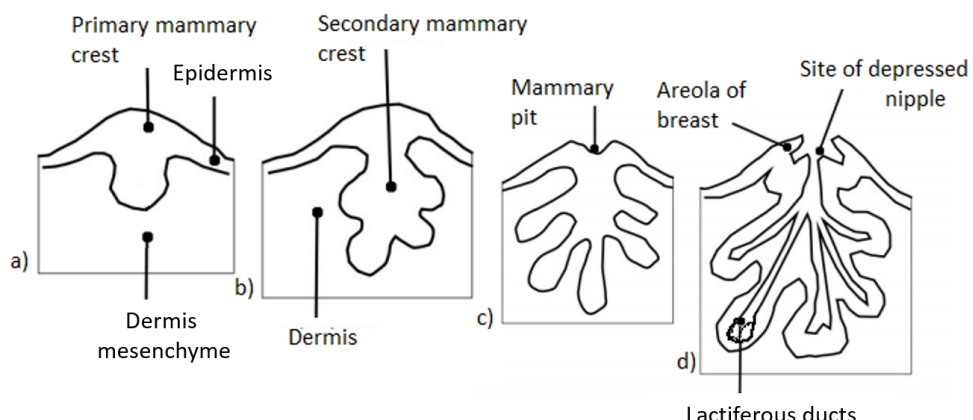


Figure 1.1: Breast embryogenesis: stages of formation pf the duct system. the ectoderm is responsible for duct system and alveoli, the mesenchyme is responsible for the connective tissue and vessels (Skandalakis, 2009).

The glandular lobes, generally remain underdeveloped until puberty (13 to 18 years). Under hormonal stimulation, the breast buds due to the development of the mammary 210 glands and increased deposition of fatty tissues, becoming palpable discs beneath the nipple. The ducts grow into the soft tissues and the lobular differentiation begins (Kopans, 2007).

Kopans (2007) analyzed breast development sequence in the subcutaneous tissues. According to the authors the evolution of breast within the fascial system is unclear, with 215 two possible evolution paths:

- (A) The superficial fascia splits in two layers forming the deep and the superficial fascia layers. The mammary glands appears between these two layers (Figure1.2.A).
- (B) The elongating ducts retracts the superficial fascia. The mammary glands is enveloped by the superficial fascia (Figure1.2.B)

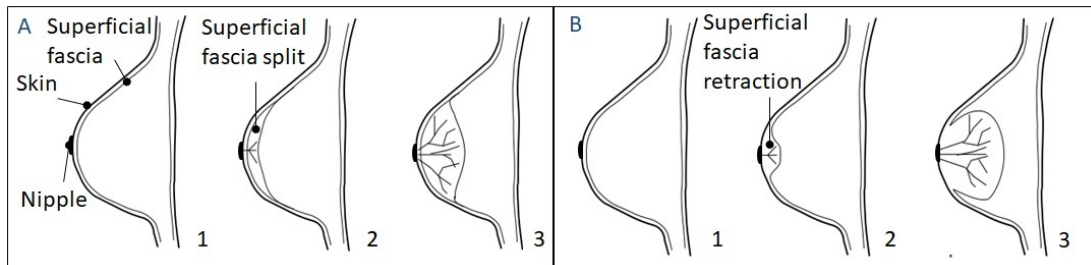


Figure 1.2: Breast development sequence in the subcutaneous tissues. A Mammary bud development by sleeting the superficial fascia in 2 layers. B Mammary bud development by fascia retracting, reproduced from (Kopans, 2007)

²²⁰ 1.1.2 Breast external appearance

In order to describe the breast appearance, several notions for localization into the breast volume and its vicinity are defined. Usually, the breast volume is divided into four quadrants: upper outer quadrant (UOQ), upper inner quadrant (UIQ), lower outer quadrant (LOQ), lower inner quadrant (LIQ)(see Figure1.3). On the other hand, the anatomical structures surrounding the breast are localized using the anatomical landmarks such as the inframammary fold, the clavicle, the sternal angle, the sternal line, the costal margin and the axilla.

²²⁵ Starting with the Warner Brother Corset Company in 1935 the underwear industry introduced a new unit to measure the breast volume, the cup. The cup size is computed using a relation between the circumference of the chest at the level of the nipples and the torso width (Pechter, 1998).

Anatomically, the adult breast is localized on top of the ribcage, between the clavicle superiorly and costal margin inferiorly. Its transverse boundaries are defined from the sternal line medially to the midaxillary line laterally (Figure1.3). The intra-individual ²³⁵ asymmetry (between left and right breasts) is considered as a normality for the young and the adult breast . The breast shape and contour are influenced by (Mugea and Shiffman, 2014):

- The volume of mammary gland in each breast quadrants.
- The amount of the subcutaneous and intra-lobular fat.
- The body contour of the chest wall.

²⁴⁰

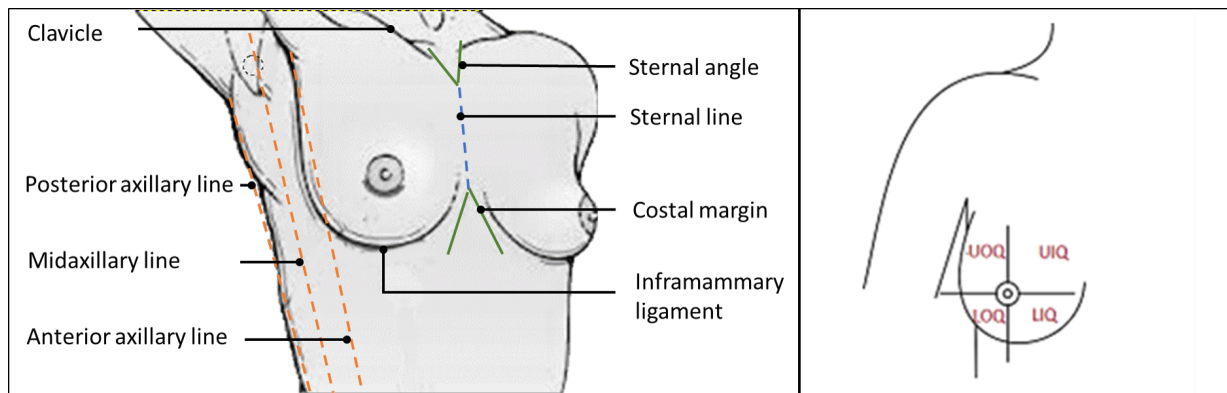


Figure 1.3: Left: thorax landmarks; Right: four breast quadrants (Vandeput and Nelissen, 2002)

- The muscular covering and thickness.
- The thickness and elasticity of the skin.

Anthropomorphic characteristics of women breast were studied almost for the aim of cosmetic and reconstructive surgery. Vandeput and Nelissen (2002) measured distances between anatomical landmarks of the thorax of 973 women with aesthetically near-perfect breasts. The authors proposed different relations as guidelines to compute the recommended breast size parameters (nipple-mid clavicle distance, nipple inframammary fold distance) as a relation of body parameters (body height, torso width). In their study, a poor correlation was found between body height or weight and breast volume. Contrariwise a high correlation was found between the nipple to inframammary fold distance or the nipple to mid clavicle distance and the thorax width. Catanuto et al. (2008) mentioned that the breast shape after surgery cannot be predicted by volumetric measurements only; they have proposed additional measures (areas, distances or angles) allowing unambiguous characterization of the breast shape. According to the authors, the curvature of the thoracic surface is the most relevant parameter to evaluate the outcome of a reconstructive breast surgery.

1.1.3 Internal structures

Breast heterogeneous structure includes a mixture of parenchyma and adipose tissue (Figure 1.4). The breast parenchyma consists of glandular components, lymphatic network and blood vessels (Clemente, 2011). Skin, Cooper's ligaments and fascias are the supporting system of the breast; their interconnection and intersections with the pectoral muscle fix and support the breast soft tissues (Mugea and Shiffman, 2014).

The **adipose tissue** is the predominant tissue of the breast that fills up depressions between the deep and superficial fascia. In the intra-fascial space, adipose tissue surrounds and is dispersed among the glandular structures. Fat properties and its spatial distribution

give the breast a soft consistency. The main aim of this tissue is to protect the lobes and lactiferous ducts.

The **glandular tissue** is represented by breast lobes. A healthy female breast is made up of 12-20 lobes. They are distributed centrally and laterally within the breast. The total amount of glandular tissue depends on the hormonal fluctuation, age and physical state. Mammary ducts arise from the lobes as branches and connect them to the female nipple. There are about 10 duct systems with a tree-like structure in each breast that carry the milk from the lobes to the nipple. The dark area of skin surrounding the nipple is called the areola. Huang et al. (2011) have studied the breast shape and fibro-glandular distribution using dedicated breast CT images. This study shows that the glandular tissues is situated in the central portion of the breast. In prone position about 60 % of glandular tissues is located near to the nipple. A mean percentage of glandular tissue was computed by Yaffe et al. (2009), the values varied from 13.7% to 25.6 % within different groups. They also mentioned a drop in glandular fraction with the advancing age.

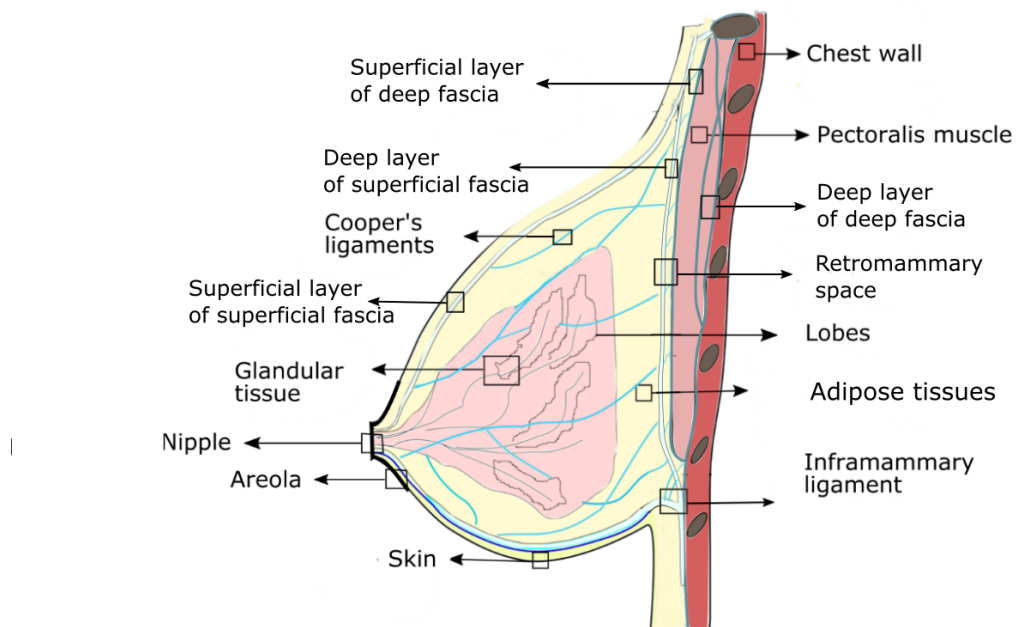


Figure 1.4: Breast anatomy, (Clemente, 2011)

280

A layer of adipose tissue and connective fascia separates the breast from the pectoral muscle forming a retro-mammary fat space.

The **skin** is the covering breast layer which provides protection and receives sensory stimuli from the external environment. It is a heterogeneous organ composed of 3 layers (see Figure 1.5 , (Kanitakis, 2002)): epidermis (dead cells) mainly composed of keratin, dermis composed of collagen and elastin fibers in a viscous matrix made of water and glycoproteins and hypodermis, mainly composed of adipocytes cells.

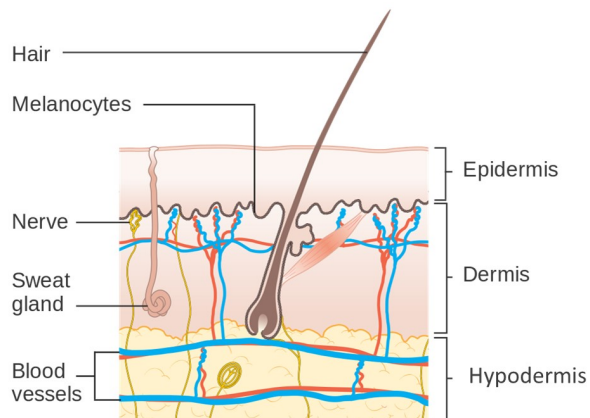


Figure 1.5: Skin anatomy, *Cancer Research UK*

The breast skin thickness vary from breast base to the nipple between $\sim 2\text{ mm}$ and $\sim 0.5\text{ mm}$. At the nipple areola region, the skin thickness measure $4\text{-}5\text{ mm}$. (Andolina and Lillé, 2011). Sutradhar and Miller (2013) studied the breast skin thickness of 16 different sectors radially oriented around the nipple. The thickness range proposed by the authors varies between 0.83mm and 2.35mm with a mean of $1.55 \pm 0.25\text{mm}$. According to this study the skin thickness varies as follows: the lateral region thickness is the thinnest among all the breast regions followed by superior/inferior and medial region; there is no significant difference between the inferior and superior breast regions; in the radially exterior region, the skin is thicker than in the radially interior region (close to the nipple). Ulger et al. (2003) found that, during the breast puberty, the breast volume increases and the skin thickness decreases in all regions.

The **connective tissue** is represented by Cooper's ligaments and fascial system. The breast fascial system is composed of deep fascia and superficial fascia. During puberty, breast is growing and the superficial fascia divides in two layers: the deep layer of the superficial fascia and the superficial layer of the superficial fascia (Kopans, 2007). Cooper's ligaments run throughout the breast tissue parenchyma from the deep layer of the superficial fascia beneath the breast to the superficial layer of superficial fascia where they are fixed (Figure 1.4). Because they are not taut, these ligaments allow the natural motion of the breast (Clemente, 2011). Between the deep layer of the superficial fascia and the superficial layer of the deep fascia, a layer of connective loose tissue forms the retro-mammary space, allowing the breast tissue to slide over the chest (Mugea and Shiffman, 2014). In regions where the superficial fascia meets the deep fascia, suspension ligaments are created. One of these ligaments is situated at the level of the sixth and seventh ribs and is called the **inframammary ligament** (Bayati and Seckel, 1995). It evolves into the **deep lateral ligament** and the **deep cranial ligament** that are respectively attached to the axillary fascia and to the clavicle. The second meeting point of the 2 fascias is situated on the sternal line and is called the **deep medial ligament** (Figure 1.6). On the upper pole of the breast, near the second rib space, the deep fascia tightly connects with the 2 layers of

the superficial fascia, here the third meeting point is created. The three ligaments are 3D structures, evolving from pectoral muscle toward the nipple underlying the skin surface.

The existence, the topography, and the thickness of the membranous layers of the superficial fascia have been studied in various regions of the body (Abu-Hijleh et al., 320 2006). According to the authors, the thickness of these superficial layers in both superior and inferior breast regions is equal to $88.12 \pm 7.70\mu m$ and $140.27 \pm 11.03\mu m$ respectively.

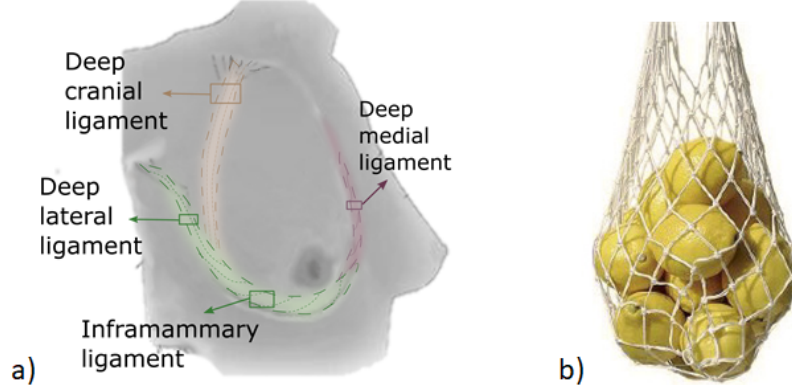


Figure 1.6: Suspensory ligaments. The suspensory ligaments together with the falcias constitute the breast support matrix and ensure their inter-connection. (Mugea and Shiffman, 2014)

The lymphatic system is a vessel network which insures the transportation of white blood cells from tissues into the bloodstream. The majority of intramammary nodes are associated with the upper outer breast tissue and the lower outer part of the breast (Kopans, 325 2007). All intramammary lymph nodes are located in the lateral half of the breast along the margin of the breast parenchyma. The lymphatic drainage of the breast extends from the subareolar plexus deep to and around the nipple (Figure 1.7).

The blood supply to the breast comes primarily from the internal mammary artery named successively subclavian, axillary, and brachial arteries (Figure 1.7), from which lateral and internal thoracic arteries run underneath the main breast tissue. 330

1.1.4 Adult breast texture changes

The female breast undergoes substantial changes during the woman's lifetime. Most changes are caused by hormones and by woman's physiological condition. Important changes in female breast stiffness and composition occur during the menstrual cycle, pregnancy and menopause. 335

There are 3 important changes during the menstrual cycle caused by hormonal changes (Andolina and Lillé, 2011). During the first phase, the estrogen (hormones) diffusion stimulates the epithelial cell multiplication and the enlargement of ductal structures. Next, during ovulation, epithelial cells begin to grow in the lobule due to progesterone hormone;

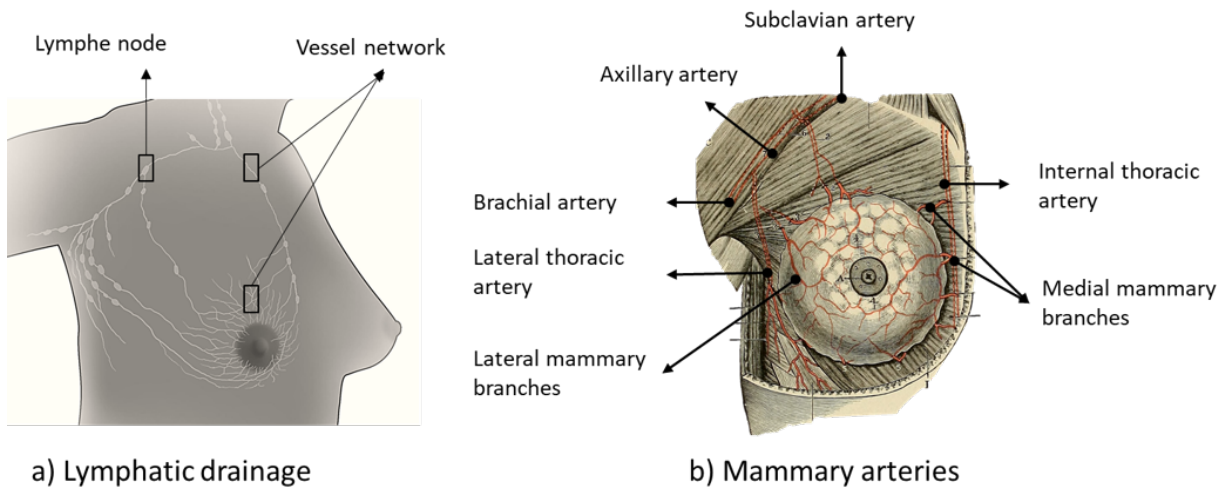


Figure 1.7: Lymphatic system and Mammary Arteries for adult female breast. Images reproduced from NCI (2012) and Pilcher (1917)

340 an increase in blood flow is also noticed. In the last phase, the ductal structures and the lobes support an involution and a regression process. It must be mentioned that not all lobules regress, therefore during menstrual cycle new lobules can be created. The work by Lorenzen et al. (2003) showed that during the premenstrual phase the stiffness of fibro-glandular tissue and glandular tissue can change by 30% and 14 % respectively. They also
 345 have shown that in the middle of the menstrual cycle, the parenchyma volume increases of 38% and the water content by 24.5%.

During pregnancy, under the influence of estrogen and progesterone, the breast enlarges in volume and density, the veins dilate and the proportion of parenchyma tissues increases. When lactation is weaned the breast returns to the pre-pregnancy state, and the atrophy
 350 of glandular, ductal, and stromal elements is observed (Pandya and Moore, 2011).

The menopausal breast contains a larger fraction of fatty tissues and reduce the number of ductal and lobular elements. During the first four years after menopause the breast is the subject of an atrophy process. The atrophy begins medially and posteriorly, then laterally, working its way to the nipple (Andolina and Lillé, 2011). In this period the breast loses progressively fat and stoma tissues, resulting in breast shrinkage and loss of contours.
 355

The breast support matrix can be stretched and attenuated by weight changes occurring during pregnancy and can relax with aging. These various changes can result in an excess of breast mobility over the chest and ptosis.

1.2 Breast Cancer

360 The first written description of breast cancer was on ancient Egyptian papyrus. At that time the treatment was considered futile and the woman was left without any medical assistance. Ancient Greeks, thought that the breast cancer was caused by an excess of

black bile. It was thought that the monthly menstrual flow naturally relieved women of this excess, which explained why breast cancer was more common after menopause (Andolina and Lillé, 2011).

Nowadays, several researches (Pike et al., 1993; Martin, 2017) have shown that the cancer is always caused by damages to a cell's DNA. The initiation of the mutagenic process that may result in various genetic errors requires cell division. A factor that increases cell proliferation will increase also the risk of cancer. The woman hormones, estrogen and progesterone, appear to impact the breast cell division rate (Ciocca and Fanelli, 1997; Fanelli et al., 1996), which explains the high rates of breast cancer in women (99% of breast cancer occurs in women). The risks of developing a cancer is increased by various factors like age, genetics, family history or life style. According to (Martin, 2017) the breast cancer risk factors can be explained by the exposure of women to the ovarian hormones during their lifetime.

The breast cancer is the second most frequent type of cancer and is the leading cause of death within women with cancer diagnosis (SPF, 2016). The Foundation for Medical Research (FRM, 2017) estimates the risk of developing breast cancer for french women as 1 in 8 with more than 47% of cases diagnosed on women within 65 years old. According to the French Public Health Agency (SPF, 2016) the incidence of breast cancer has increased by 138% between 1980 and 2005. In United Kingdom and United States by year 2000 the death rate from breast cancer was reduced by almost 20% and in 2005 was down by 25% (Peto et al., 2000). This significant improvement was attributable to the rise in the life expectancy and the upgrowth of screening technologies.

1.2.1 Cancer classification

Breast cancer type is determined by the specific cells that are affected. When a woman is developing a breast cancer, more frequently the primary tumor is developed in the epithelial cells, this type of tumor is called carcinomas. The primary tumor can also start in cells from other tissues such as muscle, fat or connective tissues. These types of tumors are called sarcomas, phyllodes, Paget disease and angiosarcomas but they are much rare (ACS, 2017).

The carcinomas are then classified based on their location and how far the cancerous cell have spread. When the cancerous cells remain within the milk ducts or lobules, the cancer is classified as a non-invasive cancer. Otherwise, the malignant cancerous cells break through normal breast tissue barriers and spread out through other body organs, they are classified as invasive cancer (Andolina and Lillé, 2011). The most common types of carcinomas characterized by their location are: ductal carcinoma and lobular carcinoma.

The invasive ductal carcinoma starts in the epithelial cells that line the milk ducts, whereas the invasive lobular carcinoma starts in the lobules. Both evolve through the surrounding tissues and may widespread to the other organs through bloodstream and lymph nodes (metastasize).

Although the non-invasive carcinomas are not malignant, they have a 40% chance to change to invasive carcinomas over a 30-year period. The non-invasive ductal carcinomas

start and stay inside the milk duct. The non-invasive lobular carcinoma overgrowth the
405 normal breast cells and stay inside the lobule.

Invasive lobular carcinoma (ILC) may be harder to detect on physical exam as well as imaging, like mammograms, than invasive ductal carcinoma. Moreover, compared to other kinds of invasive carcinomas, about 1 in 5 women with ILC might have cancer in both
410 breasts. Non-invasive ductal carcinoma is the more commonly detected form, making up 4% of symptomatic cancers and 20% of the cancer detected during a screening program. Its presence may be indicated on X-ray mammograms by microcalcifications (ACS, 2017).

1.2.2 Breast cancer screening

Early detection remains the primary defense available to prevent the development of breast cancer. Early detection of breast cancer is made possible by regular screening tests aimed
415 to find suspicious lesions before any symptoms can develop. The principal benefit of the regular screening is the potential to prevent the premature and often prolonged, painful death of the individual. Studies have shown that regular mammographic screening resulted in a 63% reduction in breast carcinoma death among women who actually underwent screening (Tabár et al., 2001). In 2012, the review of the UK screening program (NHSBSP,
420 2012) showed that it prevented 1300 deaths from breast cancer a year.

Secondary benefits include a reduction in the trauma by treating earlier-stage lesions. Indeed, earlier found invasive carcinoma better respond to treatment which means that the patient may avoid having a mastectomy or a chemotherapy.

Various worldwide countries have adopted organized breast cancer screening programs.
425 Depending on the regional statistics and the estimated risk factors (age group, breast density, family history etc) the population is invited to participate to a free screening examination. In 1994, the French National Authority for Health approved a national screening program (FNAH, 2016). Since then, every woman within 50 and 74 years old, is invited one in two years for a clinical exam and a mammography.

The individuals who are suspected of having breast cancer, will have additional diagnostic tests as: diagnostic mammography, ultrasound (US), Magnetic Resonance Imaging (MRI), biopsy, blood test etc. The diagnostic test not only helps to confirm or to infirm the screening result, but also, in case of positive test, to determine the stage and the type of the breast cancer.

435 1.3 Medical imaging

Medical images are the techniques used in medicine to achieve information on human body internal structures or internal tissues properties. This information is then processed and analyzed in order to diagnose, monitor, or treat medical conditions. This technology encompasses different imaging modalities and processes, each with their own advantages
440 and disadvantages. Next, the most relevant modalities for breast imaging are presented .

1.3.1 X-ray mammography

X-ray mammography is a type of medical imaging that uses x-rays to capture images of the internal structures of the breast (FDA definition). In digital mammography (also known as Full Field Digital Mammography, FFDM) x-rays are beamed through the breast to an image receptor (Figure 1.8). A detector converts X-rays to digital information.

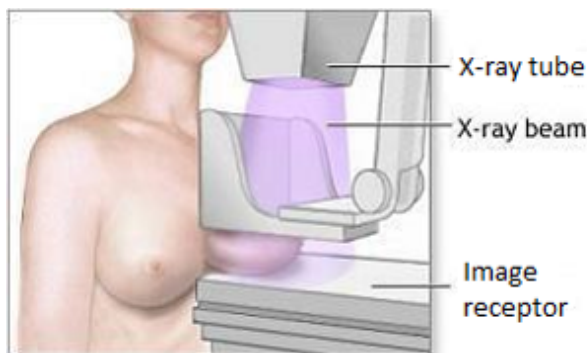


Figure 1.8: Mammographic exam

The mammography is used to detect parenchymal distortion, asymmetry, masses and clusters of microcalcifications within the breast. These findings are not pathogenic and require a tissue diagnosis to confirm the presence of an invasive cancer, in situ cancer, or a nonmalignant finding. Microcalcifications (*μcalc*) are small calcium deposits embedded in a protein matrix. They have x-ray attenuation coefficients substantially higher than breast tissue and therefore appear as bright spots in the x-ray images. The diameter of a microcalcification is typically inferior to 1mm (Henrot et al., 2014). In terms of form, breast microcalcifications can come in many shapes and sizes. So, they can be round, linear, coarse or granular. A mass is a radiological finding demonstrating an increased density versus the surrounding tissue. There is a large variation on mass size and shape, usually a suspicious mass is larger than 8mm and have irregular or speculated margins (McKenna, 1994). Asymmetry and parenchymal distortion are visualised as tethering or indentation of breast tissue. They are the third most common mammographic appearance of nonpalpable breast cancer, representing nearly 6% of abnormalities detected on screening mammography (Gaur et al., 2013).

A standard mammographic protocol always includes breast compression prior to image acquisition. Women breast is compressed between two plates until a nearly uniform breast thickness is obtained. Nowadays, the European Commission recommends a force standardized breast compression, i.e. the compression stops at a level of force just below the subjects pain threshold or to the maximum setting of the machine (not to exceed 200 N). Analog mammography used screen/film detector technology in order to display breast internal structures, thus a uniform breast compression was needed in order to ensure a uniform exposure over the breast volume. With digital mammography, the exposure variation could be corrected with post-processing, while the breast compression is still indispensable to hold the breast away from the chest wall, to reduce the blur due to physical motion, to

reduce the absorbed dose of ionizing photons, to separate overlapping structures, to reduce image degrading scatter (Kopans, 2007).

Studies in different countries have assessed mammography sensitivity and specificity. The obtained sensitivities ranges between 81 and 88 %, and the specificities between 83 and 475 98 % (Kemp Jacobsen et al., 2015; Hofvind et al., 2012). The mammography sensitivity is mostly affected by dense breasts. A dense breast is a breast for which the proportion of the fibroglandular tissues exceed greatly the proportion of fatty tissues. Fatty tissues are radiographically translucent, and lead to high intensity signal appearing on the mammographic images as dark areas. Meanwhile, the fibroglandular tissues and breast cancers 480 tend to absorb more x-rays photons, therefore they will appear as white areas. The lack of contrast between the cancer and dense regions of the background will make the detection more difficult.

1.3.2 Ultrasounds

Breast ultrasound uses high-frequency sound waves to image breast tissues. The ultrasound 485 technician put gel on the skin above the area of interest and moves the sound-emitting probe over the skin. The emitted waves are bounced by the breast soft tissues. The probe picks up the reflected waves and transforms them into a 2D image.

For asymptomatic women, a careful investigation of lateral and profound breast tissues is needed to identify the suspicious lesions. The limited field of view of the ultrasound 490 image prevents from seeing abnormalities that lie deeper in the breast. Consequently, the ultrasounds are not sufficient for regular screening and are used to complement other screening tests. However, it is widely used to investigate suspicious lesions found within mammography, clinical or self-examinations. Breast ultrasound is particularly effective in differentiating cysts from solid lesions, but has a low sensitivity for breast which are the 495 most common feature in addition to masses associated with breast cancer. Breast ultrasound can also be used for differential diagnosis, local staging and intervention guidance.

Ultrasound elastography is a sonographic imaging technique combining the ultrasound technology with the basic physical principles of elastography. Elastography assesses tissue deformability by providing information on the tissue elasticity. It consists of either an 500 image of strain in response to force or an image of estimated elastic moduli. This approach is somehow equivalent to clinical or self-examination, but with a higher precision.

Shear-wave elastography (SWE) uses focused pulses of ultrasound generated by the probe to induce soft tissues deformation. The tissues elasticity is assessed either by directly measuring soft tissues deformation or by measuring the speed of shear wave propagation. 505 The combination of SWE with conventional ultrasound increases the diagnostic performance for breast lesions, compared with conventional ultrasound alone (Youk et al., 2017). Elastography serves as a complementary tool to differentiate benign from malignant lesions by providing information about the lesion stiffness(Itoh et al., 2006; Olgun et al., 2014)

510 **1.3.3 Magnetic resonance imaging**

Magnetic resonance imaging (MRI) is a noninvasive procedure used in breast imaging for studying internal structure of the breast that cannot be properly imaged using standard x-ray imaging (dense breasts). It employs radio-frequency (RF) waves and intense magnetic fields to excite hydrogen atoms. Body parts that contain hydrogen atoms (e.g. in water) 515 are then imaged with contrasts depending on relaxation phenomenon characteristic of the tissues in the body. The quality of the image produced by MRI techniques depends, in part, on the strength of the received signal. For higher image quality, it is optimal to use an independent RF receiving coil placed in close proximity to the region of interest. For breast imaging, dedicated breast MRI coils can be used. The patient is placed in prone 520 position with the breast inside the coil and both arms by the sides of the body.

When the cancerous tumor develops, new vascularizations are created on the direct surrounding to provide oxygen. Thus, for breast cancer imaging, a contrast agent may be used to enhance highly vascularized regions. These regions corresponding to the lesions 525 are visualized due to their uptake of contrast agent. Contrast enhanced MRI is used as a screening modality for women with high risk of cancer.

Low specificity and high cost of MRI restricts its use in a routine screening (Peters et al., 2008). However, it is increasingly used for high-risk groups and for lesions that are difficult to detect with mammography or ultrasounds tests.

1.4 Conclusion

530 Today, mammography the primary imaging modality used in breast cancer screening and plays an important role in cancer diagnosis. Ultrasounds and Magnetic Resonance Imaging are complementary imaging techniques used mostly for dense breasts and high-risk women.

In order to obtain an accurate reading, the mammography machine needs to compress 535 the breasts. The discomfort and pain produced by breast compression might deter women from attending breast screening by mammography (Aro et al., 1999; Fleming et al., 2013). In a study by (Dullum et al., 2000) more than 50% of attendants (N= 1800) mentioned from moderate to extreme physical discomfort. It has been reported that the fear for pain itself can already be a reason to avoid getting the first mammogram (Andrews, 2001), and that 15% of those who skipped the second appointment cited as the main cause an 540 unpleasant or painful first mammogram (Fleming et al., 2013; Whelehan et al., 2013). Postpone the mammographic exam can lead to delayed breast cancer diagnoses and worse prognoses (expected outcomes) for some women.

The main direct cause of pain in mammography is the flattening of the breast which 545 is directly linked to the applied compression force. Latest researches indicate that with a reduced level of compression (10N vs 30N), 24% of women did not experience a difference in breast thickness. If breast thickness is not reduced when compression force is further applied, then discomfort increases with no benefit in image quality or average dose. Therefore, a detailed study on alternative breast compression techniques considering the patient

CHAPTER 1. CLINICAL BACKGROUND

comfort in addition to the image quality and ionizing radiation dose is needed.

550 The aim of this work is to provide a simulation framework capable to assess the patient physical comfort indicators, as well as the corresponding image quality and average glandular dose for breast compression with different paddles designs. The developed numerical methods would serve to build an optimal compression paddle in terms of latter listed parameters, and therefore increase the adherence to breast cancer screening.

555 In this scope, a subject-specific biomechanical Finite Element (FE) model is developed and evaluated on real deformations measured on MR images. The proposed model is then used to compute the tissues deformation associated to breast compression during mammography. The resulting internal stress/strain intensities are then used as a first estimate of the physical comfort. The deformed breast geometry is the subject of a Monte-
560 Carlo image simulation allowing to assess the image quality (IQ) and average glandular dose (AGD), in order to validate the image quality for the different strategies of compression we are considering.

2

BIOMECHANICAL BREAST MODELING *State of the art*

565 Finite elements models are widely used to estimate body parts deformation under pre-defined boundary conditions. Several biomechanical models of the breast were recently developed providing physics-based predictions of tissue motion and internal stress and strain intensity. In our work, we assume that the strain intensity obtained during the tissues deformation may be correlated with the patient discomfort. Thus, a biomechanical model obtained from the patient's MRI volume can be subsequently used to mimic 570 breast compression during the mammographic acquisition. The resulting tissues strain cartography can be used as a first quantification of the patient inconfort.

575 This chapter provide theoretical background on continuous mechanic theory applied to soft tissues modeling. The principle of finite elements theory is defined including solid bodies and contact mechanics. A review of the existing biomechanical breast model is given describing the main challenges in the field and the proposed solution. These works proved the core foundation for the next developed patient specific breast model.

2.1 Continuous mechanics

Continuum mechanics is a branch of mechanics that deals with the analysis of the kinematics and the mechanical behavior of materials modeled as a continuous mass. Continuum mechanics is based on the continuum hypothesis: the matter is continuously distributed throughout the space occupied by the matter. The basis for the hypothesis is how physical quantities, as for example pressure, temperature, and velocity, are measured macroscopically.

In this section the continuous mechanis theory applied to solids bodys was discribed using the following sources: Belytschko et al. (2013); Abeyaratne (2012).

2.1.1 Deformation and strain

Continuous mechanics is the mathematical description of how physical objects that occur in nature respond to the application of forces.

A **body** is the mathematical abstraction of an *object* and is defined by its geometric and constitutive properties. At a macroscopic level, a solid *object* is described as homogeneous and continuous body, i.e. the substance of the object has a unique composition and completely fills the space it occupies thus, ignoring the granular (atomic) nature of matter. In continuous mechanics, a body \mathcal{B} is composed of a set of **particles** p (or material points). Each particle is located at some defined **point** x in three dimensional space. The set of all the points in space, corresponding to the locations of all the particles, is the **domain** Ω occupied by the body in a given configuration, here also named *geometry*. A particular body can change its configuration and therefore the occupied region in the space when exposed to some external stimuli like force, pressure or heat.

The **configuration** of a body is defined as a one-to-one mapping between the particle p and position x , $\Omega_0 = \chi_0(\mathcal{B})$ (see figure 2.1). To describe the solid's respond to external stimuli one needs to know the changes in geometrical characteristics between at least two configurations: the configuration that one wishes to analyze Ω_1 , and the **reference configuration** relative to which the changes are to be measured Ω_0 . Here, see figure 2.1, the mappings χ_0 and χ_1 take $p \rightarrow X$ and $p \rightarrow x$, thus X and x are the positions of particle p in the two configurations under consideration.

Frequently, the reference configuration is fixed for a given study and is chosen arbitrary in a the most convenient way among all the configurations that the body can sustain.

The **deformation** of the body from the reference configuration Ω_0 is characterized by the next defined mapping Φ :

$$x = \Phi(X) = \chi_1(\chi_0^{-1}(X)), \quad \text{where } X \in \Omega_0 \text{ and } x \in \Omega_1 \quad (2.1)$$

The **displacement** u of a particle is the difference between its position in the analyzed configuration (or current configuration) and its position in the reference configuration.

$$u(X) = \Phi(X) - X \quad (2.2)$$

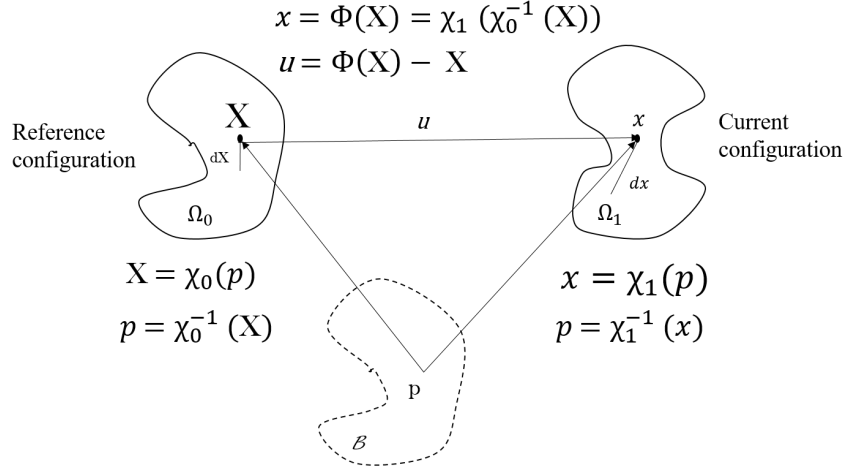


Figure 2.1: The position of a particle in the reference and current body configurations.

Suppose that $G(\Omega_1)$ is the value of some extensive physical property associated with the body \mathcal{B} in the current configuration (such as the body mass m). There exists a density $g(x)$ such that:

$$G(\Omega_1) = \int_{\Omega_1} g(x) dv$$

where dv is the volume of the material element. Thus, the property $G(\Omega_1)$ is related to the body while the density $g(x)$ is related to the position of the body particle.

615 Eulerian and Lagrangian formulations

There are two classical techniques used to describe the body physical characteristics depending on the choice of independent variables. Some physical characteristics, such as mass density, can be defined for each individual particle. In such cases, the body characteristics are defined by the function

$$m = \mathcal{M}(p)$$

for all $p \in \mathcal{B}$. Here the coordinate system remains consistent and moves with the particle. Therefore, the coordinates of both, the particle and the attached variable, do not change along the deformation. A particle is an abstract entity and cannot be used in numerical calculations, thus it is described by its location in reference configuration $p = \chi_0^{-1}(X)$.

$$m = \mathcal{M}(p) = \mathcal{M}(\chi_0^{-1}(X))$$

We call X Lagrangian or material coordinates and their application is called Lagrangian or material description.

Instead of defining body characteristics as a function of body particles, one can define it directly as a function of particle location in current configuration by using the relation

$x = \chi_1(p)$, and therefore

$$m = \tilde{\mathcal{M}}(x) = \mathcal{M}(\chi_1^{-1}(x))$$

Here the coordinate system is fixed and the particles coordinate are changing. Therefore, the position of particle and any related quantity changes during the deformation. We
620 call x Eulerian or spatial coordinates and their application is called Eulerian or spatial description.

These approaches are distinguished by three important aspects: the mesh description, the stress tensor and momentum equilibrium and the strain measure. The advantages and
625 drawback of these two formulations will be discussed later in this chapter. Further, only Lagrangian formulation is used to describe the continuous deformation of soft tissues.

Deformation gradient

In mathematical formulation the deformation gradient tensor F is the Jacobian matrix of the deformation $\Phi(X)$:

$$F = \frac{\partial \Phi(X)}{\partial X} = \frac{\partial x}{\partial X} \quad (2.3)$$

Considering infinitesimal quantities, the deformation gradient relates the segment dX
630 in the reference configuration to the corresponding deformed segment dx in the current configuration (Figure 2.1)

$$dx = F \cdot dX. \quad (2.4)$$

In addition to the mapping of such vectors, the deformation gradient tensor allows also the mapping of differential volumes as:

$$dv = \det(F)dV = JdV \quad (2.5)$$

The Jacobian determinant of the deformation gradient tensor J is a measure of the
635 volume variation during the deformation. It can be used to relate extensive physical properties in the current and reference configurations:

$$\int_{\Omega_1} g(x)dv = \int_{\Omega_0} g(\Phi(X))JdV \quad (2.6)$$

Decomposition of the deformation gradient tensor into rotation and stretch

The deformation gradient tensor F completely characterizes the body deformation in the vicinity of a particle p . This deformation consists of a rigid body rotation and body *stretch*
640 (see Figure 2.2). As dX and dx are differential segments, the map F is not affected by rigid-body translations.

Generally, the body stretch is defined as the ratio of the deformed line elements to the length of the corresponding undeformed line element

$$l = \frac{|dx|}{|dX|}, \quad (2.7)$$

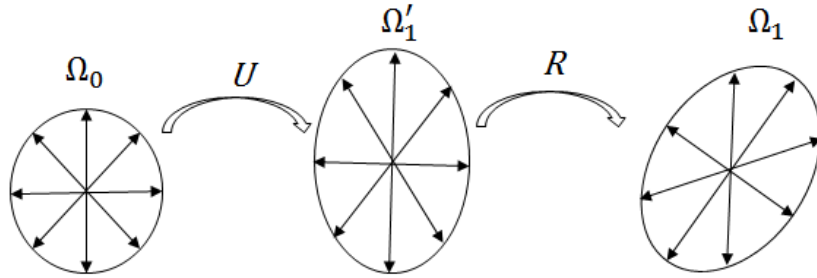


Figure 2.2: Decomposition by rotation and a stretch of a material particle.

and consists locally on three mutually orthogonal stretches named **the principal stretches**.

According to the polar decomposition theorem, the deformation tensor can be written as the product of a proper orthogonal tensor R representing the rotational part, and a symmetric positive defined tensor U representing the body distortion.

$$F = R \cdot U. \quad (2.8)$$

where U and R are given by the relations $U = (F^T \cdot F)^{\frac{1}{2}}$ and $R = F \cdot U^{-1}$. The essential property of tensor U is that it is symmetric and positive, therefor it has three real positive eigenvalues $\lambda_1, \lambda_2, \lambda_3$ and a corresponding triplet of orthonormal eigenvectors r_1, r_2, r_3 . Thus then an infinitesimal segment dx is stretched by the tensor U , the segment is distorted in the principal direction of U by amounts of the corresponding eigenvalues of U .

The tensor U is also called the **right stretch tensor**. Since there is a one-to-one relation between U and U^2 , for the simplification of numerical calculus the stretch tensor can be replaced by the **Green deformation tensor** $C = F^T \cdot F$.

There are three particular functions of C called the principal invariants.

$$I_1(C) = \text{tr}C, \quad I_2(C) = \frac{1}{2} [\text{tr}C^2 - (\text{tr}C)^2], \quad I_3(C) = \det(C). \quad (2.9)$$

These functions are related to the three principal stretches by the next relations:

$$I_1(C) = \lambda_1^2 + \lambda_2^2 + \lambda_3^2, \quad I_2(C) = \lambda_1^2\lambda_2^2 + \lambda_2^2\lambda_3^2 + \lambda_3^2\lambda_1^2, \quad I_3(C) = \lambda_1^2\lambda_2^2\lambda_3^2 \quad (2.10)$$

The essential property of the principal invariants is that they don't change under coordinate transformations for a given body configuration. Their use to compute the body stretch will be an essential part of constitutive modeling, because the behavior of a material should not depend on the coordinate system.

It can be also shown that:

$$\det(C - \mu I) = -\mu^3 + I_1(C)\mu^2 - I_2(C)\mu + I_3(C) \quad (2.11)$$

Strain measures

665 Referring to small deformations, the engineering nominal strain is defined as the ratio of the change in length of the deformed line element to the length of the corresponding undeformed line element:

$$\epsilon = \frac{dx - dX}{dX} \quad (2.12)$$

When the body is not deformed, the deformation gradient F and therefore the right stretch tensor U is equal to identity tensor I . The strain in such a case is equal to zero.

670 For most biological soft tissues, large deformation has to be considered. In that case, the previously defined strain is no more applicable. For large deformations, a measure of strain can be any monotonically increasing function related to stretch in a one-to-one manner, this function has to vanish in the reference configuration.

In orthogonal coordinate system, an admissible function is

$$f(x) = \frac{1}{m}(x^m - 1) \text{ for } (m \neq 0) \text{ and } \ln(x) \text{ for } (m = 0) \quad (2.13)$$

675 For $m = 0$ the function represents the Hencky strain tensor,

$$E = \ln(U), \quad (2.14)$$

for $m = 1$ the function represents the Biot strain tensor

$$E = U - I, \quad (2.15)$$

and for $m = 2$ the Green-Lagrangian stain tensor:

$$E = \frac{1}{2}(U^2 - I) = \frac{1}{2}(C - I) \quad (2.16)$$

The Green-Lagrangian tensor is commonly used in practice as, by using the relation 2.11, it can be computed without prior knowledge of the eigenvectors of the Green deformation tensor C .

2.1.2 Stress measures

Generally, forces are categorized as internal and external forces. An **external force** is a force caused by an external agent outside of the system, and contrariwise an **internal force** is a force exchanged by the particle in the system. The external forces, in turn, 685 are categorized in **body forces** (acting at the distance) and **contact forces** (acting on the body surface). The relation between body forces per unit undeformed volume $\tilde{b}(X)$ (Lagrangian coordinates) and body forces per unit deformed volume $b(x)$ is given by the following relation:

$$\tilde{b} = \frac{dv}{dV} b = Jb. \quad (2.17)$$

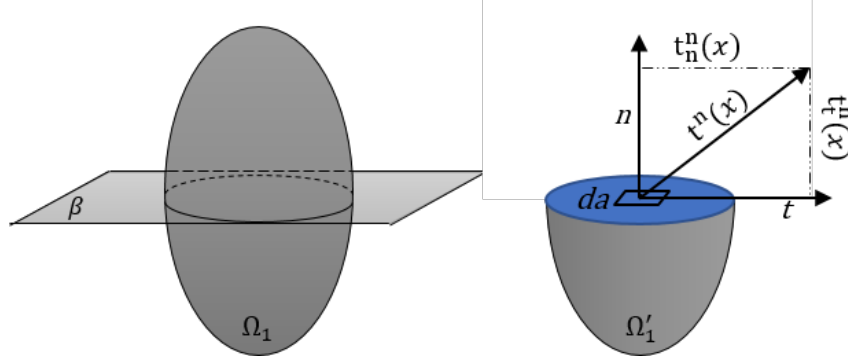


Figure 2.3: True stress vector $t^n(x)$ at point x on the fictitious surface created by the cutting plane β of normal \vec{n} passing through the point x .

The contact forces can act on the external surface of the body or on a imaginary internal surface enclosing a volume element (Fig. 2.3). In general terms, the stress (or the **traction vector**) $t^n(x)$ is defined as contact force per unit area da in the limit as $da \rightarrow 0$. Therefore $t^n(x)$ varies from point to point in intensity and orientation depending on the $da(n)$ orientation. The stress vector projection on normal axis n defines the **normal stress vector** and its projection on the tangential axis define the **shear stress vector**.

The stress on the boundary $\partial\Omega_1$ of the region occupied by the body is applied by external forces through physical contacts along the boundary. When formulating and solving a boundary-value problem, this stress defines the boundary conditions.

Cauchy's lemma

Cauchy's lemma states that traction vectors acting on opposite sides of a surface are equal and opposite.

$$t^{-n}(x) = -t^n(x) \quad (2.18)$$

Cauchy's Law

Cauchys law states that there exists a Cauchy stress tensor σ which maps linearly the normal to a surface to the stress vector acting on that surface, according to the next relation

$$t^n = \sigma \cdot n \quad \text{where} \quad t_i^n = \sigma_{i,j} n_j \quad (2.19)$$

When large deformations are considered, the reference and current configurations of the body are significantly different and a clear distinction has to be made between them. The traction vector t^n is defined in Eulerian coordinates (body current configuration) and is also called the **true stress**. Accordingly, the Cauchy stress tensor σ is called the true stress tensor.

The definition of any measure with respect to the deformed configuration is less practical as it is usually unknown a priori. For the simplification of mathematical formulation, a

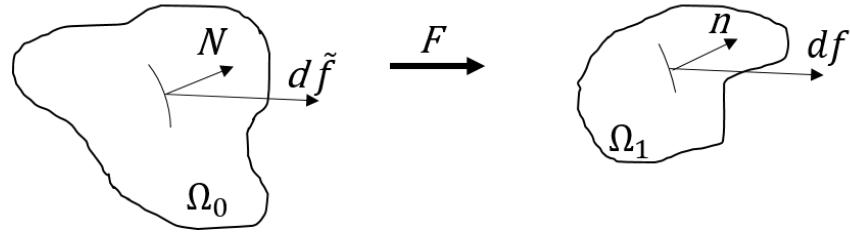


Figure 2.4: Deformation of area dA into area da . The force df acting on deformed area da and the pseudoforce $d\tilde{f}$ acting on undeformed area dA

new pseudostress is defined in the Lagrangian coordinate space named the **engineering stress**. The engineering stress has no physical meaning and has to be converted in to true stress for any interpretations.

⁷¹⁵ Next, two pseudostress vectors are defined (Fig. 2.4):

- T^N defined as the contact force df per unit area dA in reference configuration.
- \tilde{T}^N defined as the contact pseudoforce $d\tilde{f}$ per unit area dA in reference configuration.

Accordingly, two pseudostress tensors are defined based on pseudostress vectors:

- ⁷²⁰
- $T^N = P \cdot N$, P is called **first Piola-Kirchhoff stress tensor**,
 - $\tilde{T}^N = S \cdot N$, S is called **second Piola-Kirchhoff stress tensor**.

were N is the normal vector of unit area dA .

The three stress tensors are linked by the next relation

$$\sigma = J^{-1}F \cdot P = J^{-1}F \cdot S \cdot F^T \quad (2.20)$$

2.1.3 Conservation equations

Three conservation laws must be satisfied by physical system subject to any applied boundary conditions: **conservation of mass**, **conservation of linear momentum** and **conservation of angular momentum**. The resulting equations describe partially the mechanical behavior of a continuous body.

Conservation of mass

The mass m of a body with the density ρ , that infills the space region Ω_1 is given by :

$$m(\Omega) = \int_{\Omega} \rho(X) dV \quad (2.21)$$

The mass conservation law requires that the body mass remains constant throughout all possible body configurations. For a Lagrangian formulation, this results in a relation

between the body density in the reference configuration ρ_1 and the body density in the current configuration ρ .

$$\int_{\Omega_1} \rho_1 dv = \int_{\Omega_0} \rho_0 dV = \text{const.}$$

⁷³⁰ Using the relation 2.6 one can deduce that:

$$\int_{\Omega_0} (\rho_1 J - \rho_0) dv = 0 \quad \text{and} \quad \rho_1 J = \rho_0 \quad (2.22)$$

Conservation of the linear momentum

Assume that a body \mathcal{B} is defined on a arbitrary region Ω_0 with boundary Γ_0 , and is subjected to a body-force $\rho_0 b$ and the surface traction T^N . And let X be the particle location in the undeformed solid. The total force acting on the body \mathcal{B} is defined as:

$$f = \int_{\Omega_1} \rho_0 b(X) dV + \int_{\Gamma_0} T^N(X) dA \quad (2.23)$$

⁷³⁵ The conservation of the linear momentum requires that the total forces acting on the body to be equal to the time rate change of the linear momentum. In a static problem the time rate change of the linear momentum is neglected and thus an equilibrium equation is obtained.

$$\rho_0 b + \nabla_0 \cdot P = 0 \quad (2.24)$$

⁷⁴⁰ Where the P_{ji} are the components of first Piola-Kircchoff stress tensor. The equilibrium equation can be formulated in terms of the second Piola-Kircchoff stress tensor by using 2.20 relations.

Conservation of angular momentum

The conservation of angular momentum requires that the resultant momentum on any part of the body about a fixed point \mathcal{O} equals the rate of increasing of its angular momentum (about \mathcal{O}). For a static problem, the integral form of the conservation of angular momentum is defined as:

$$\int_{\Omega_0} X \times \rho_0 b(X) dV + \int_{\partial\Omega_0} X \times T^N(X) dA = 0 \quad (2.25)$$

The relation 2.25 requires that the second Piola-Kircchoff stress tensor is a symmetric tensor:

$$S = S^T \quad (2.26)$$

⁷⁵⁰ In summary, the conservation equations are fulfilled if and only if the following local conditions are fulfilled at each point in the body:

$$\rho_1 J = \rho_0, \quad \nabla_0 \cdot S \cdot F^T + \rho_0 b = 0, \quad S = S^T \quad (2.27)$$

with the traction on the surface related to the stress through $\tilde{T}^n = S \cdot N$. For the simplification of mathematical calculus, the constitutive equations are formulated in terms of the second Piola-Kircchoff stress tensor using the relations 2.20.

2.1.4 Constitutive models

⁷⁵⁵ The constitutive models, called also material models, define the relation between stress and strain of a physical system under the action of external stimuli. It is almost impossible to define a universal material behavior capable to model the material response to all possible conditions. Thus, for a given material, several constitutive models can be defined depending on the studied characteristics.

⁷⁶⁰ Biological materials are classified into:

- *Isotropic or anisotropic materials*: in a isotropic (anisotropic) material the values of a property is constant (vary) with respect to the direction.
- *Compressible or incompressible materials*: in a compressible (incompressible) material the volume changes (remains constant) during the deformation and the density remains constant. For a incompressible material the Jacobian determinant of the deformation tensor J is equal to 1.
- *Homogeneous or heterogeneous materials* in a homogeneous (heterogeneous) material the values of a property is constant (vary) with respect to the position within the body.

⁷⁷⁰ Biological soft tissues are modeled using elastic materials model. The elasticity is the property of a solid material to return to its original size and shape when the influence of an external force is removed. In this case the strains are said to be reversible.

Considering small deformations, the stress-strain law of a linear material is given by the **Hook's law**

$$\sigma = \lambda \epsilon,$$

where the coefficient of proportionality λ is named **Young's moduli**.

Elastic materials may be defined also with a non-linear stress-strain relationship. In such cases the elastic moduli (λ) is defined in function of strain ϵ

$$\lambda = \frac{\partial \sigma}{\partial \epsilon} = f(\epsilon).$$

⁷⁷⁵ For example, for an elastic exponential material (Azar et al., 2002) the elastic moduli is computed using the function

$$f(\epsilon) = b e^{m\epsilon}, \quad (2.28)$$

where b and m are material parameters.

For large deformation the stress-strain relationship is deduced from a potential function. A **hyperelastic** material is an elastic material for which the work is independent of the deformation path. The material reversibility and path-independent behavior implies the absence of energy dissipation during the deformation. Thus there exist a **potential** function $W(E)$ such that

$$S = \frac{\partial W(E)}{\partial E} = 2 \frac{\partial \psi(C)}{\partial C}$$

Moreover, if the material is isotropic, the stored strain energy W of a hyperelastic material can be written as a function of principal invariants (I_1, I_2, I_3) of the Green deformation tensor C previously defined in equation 2.9.

⁷⁸⁰ We introduce below the most used potential functions for the characterization of biological soft tissues.

For the simplification of potential expressions, we define the first and the second deviatoric strain invariants:

$$785 \quad \bar{I}_1 = \frac{I_1}{I_3^{2/3}}; \quad \bar{I}_2 = \frac{I_2}{I_3^{4/3}}$$

We also define the **Bulk moduli** as measure of a material's resistance to compression; the **shear moduli** as the ratio of shear stress to the shear strain; and the **Poisson ratio** as the ratio between longitudinal strain to the transverse strain describing the body shape change. For small deformation the Bulk moduli and shear moduli are linked to the Young's moduli and Poisson ratio by the next relations:

$$K = \frac{\lambda}{3(1 - 2\nu)} \quad \text{and} \quad \mu = \frac{\lambda}{2(1 + \nu)} \quad (2.29)$$

Neo-Hookean potential function

The Neo-Hookean (Treloar, 1943) law is an extension of the Hook's law to large deformations. The potential function is based only on the first invariant and is given by

$$790 \quad W = \frac{\mu}{2}(\bar{I}_1 - 3) + \frac{K}{2}(J - 1)^2, \quad (2.30)$$

where μ and K are initial shear moduli and initial Bulk moduli respectively.

⁷⁹⁵ Mooney-Rivlin potential function

The potential function of a Mooney-Rivlin (Rivlin and Saunders, 1951) material is defined as:

$$W = \frac{\mu_1}{2}(\bar{I}_1 - 3) + \frac{\mu_2}{2}(\bar{I}_2 - 3) + \frac{K}{2}(J - 2)^2, \quad (2.31)$$

where the constants μ_1 and μ_2 describing the material properties are linked to the initial shear moduli $\mu = (\mu_1 + \mu_2)$. And the constant K is the initial Bulk moduli.

⁸⁰⁰ Gent potential function

The potential function of a Gent (Gent and Thomas, 1958) material model is defined as:

$$W = -\frac{\mu J_m}{2} \ln \left(1 - \frac{\bar{I}_1 - 3}{J_m} \right) + \frac{K}{2} \left(\frac{J^2 - 1}{2} - \ln J \right), \quad (2.32)$$

where μ and K constants are the initial shear moduli and the initial Bulk moduli respectively. And J_m is a parameter limiting the value of $(\bar{I}_1 - 3)$

Ogden model

- 805 The Ogden (Ogden, 1972) material model is based on the three principal stretches ($\lambda_1, \lambda_2, \lambda_3$) and $2N$ material constants, where N is the number of polynomials that constitute the potential function:

$$W = \sum_{i=1}^N \frac{\mu_i}{\alpha_i} (\lambda_1^{\alpha_i} + \lambda_2^{\alpha_i} + \lambda_3^{\alpha_i} - 3) + \sum_{k=1}^N \frac{K}{2} (J - 1)^{2k}, \quad (2.33)$$

where μ_i and α_i are material constants, and K is the Bulk moduli.

Yeoh model

- 810 The potential function of Yeoh (Yeoh, 1990) model is based on the first invariant:

$$W = \sum_{i=1}^N \mu_i (\bar{I}_1 - 3)^i + \sum_{k=1}^N \frac{K}{2} (J - 1)^{2k}, \quad (2.34)$$

where the μ_i are material constants and K is the Bulk moduli.

Governing equations of Lagrangian formulation

- We consider a body \mathcal{B} which occupies in the reference configuration the domain Ω_0 with a boundary Γ_0 . The governing equations for the mechanical behavior of a continuous body
815 are:

1. Conservation of mass $\rho_1 J = \rho_0$
2. Conservation of linear momentum $\nabla \cdot P + \rho b = 0$
3. Conservation of angular momentum $F \cdot P = P^T \cdot F^T$
4. Constitutive equations
- 820 5. Measure of strain $E = \frac{1}{2}(C - I)$
6. Boundary condition: $e_i \cdot N \cdot P = e_i \cdot \bar{t}$ on $\Gamma_0^{t_i}$
7. Internal continuity condition: $\llbracket e_i \cdot N \cdot P \rrbracket = 0$ on Γ_0^{int}

- Where we note $\Gamma_0^{t_i}$ the set of prescribed traction \bar{t} on the body boundary Γ_0 ; and
825 Γ_0^{int} is the union of all surfaces where the stresses are discontinuous in the body (material interfaces).

The momentum equation together with the traction boundary condition and interior traction continuity condition are called generalized momentum balance (GMB).

2.2 Finite Element Discretization

In continuous mechanics the body deformation is expressed in terms of partial differential equations (PDE). For the majority of problems, the PDEs cannot be solved analytically, therefore approximation methods are developed. To this end, the finite element (FE) method has become the standard numerical calculation to compute such approximations. The computational domain, the unknown solution, and its partial derivatives are discretized, so as to obtain a set of algebraic equations for the function values at a finite number of discrete locations. The unknowns of the discrete problem are associated with a computational mesh which represents a subdivision of the domain Ω_0 into many small control volumes Ω_k

2.2.1 Eulerian and Lagrangian mesh description

The mesh description depends on the chosen independent variables (Eulerian or Lagrangian formulation). An Eulerian mesh formulation is usually used to solve problems linked to fluid like materials and a Lagrangian mesh for solid like materials. In an Eulerian mesh, the Eulerian coordinates of nodes are fixed (coincident with spatial points) and the material point change in time (see Figure 2.5.b). In this case the mesh has to be large enough to contain the body in its current configuration. Throughout the deformation, the material points will belong to different elements. On the contrary, in a Lagrangian mesh, the Lagrangian coordinates of nodes are time invariant, nodal trajectory corresponds with material points trajectory and no material passes between elements (see Figure 2.5.a).

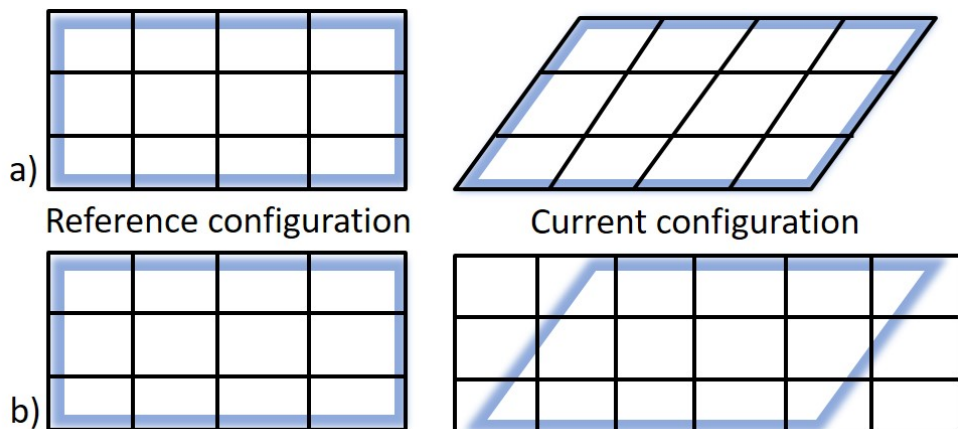


Figure 2.5: a) Lagrangian mesh formulation. b) Euler mesh formulation

In a Lagrangian mesh, the boundary and interface nodes remain coincident with body boundaries and material interfaces throughout the entire deformation. Thus, the boundary conditions are defined directly on the respective nodes. On the other hand, in a Eulerian mesh the boundary and interface conditions have to be defined on point which are not nodes. This implies important complications in multi-dimensional problems.

An important drawback of a Lagrangian mesh affect mainly the large deformation domain. As the nodes are coincident with the material points, the elements deform with materials. Therefore, the magnitude of deformation is limited because of element distortion.
855 The limited distortion that most elements can sustain without performance degradation or failure is a important factor in nonlinear analysis with Lagrangian formulation.

2.2.2 Lagrangian mesh

The general approach of the FE method in Lagrangian formulation is shown in Fig. 2.6.
860 First the momentum equations with given boundary conditions are multiplied by a set of appropriate test functions. The test functions have to satisfy all displacement boundary conditions and to be smooth enough so that all derivatives in momentum equations are well defined. Then performing an integration by parts, the week formulation of GMB is obtained, also called the principle of virtual work (Belytschko et al., 2013).

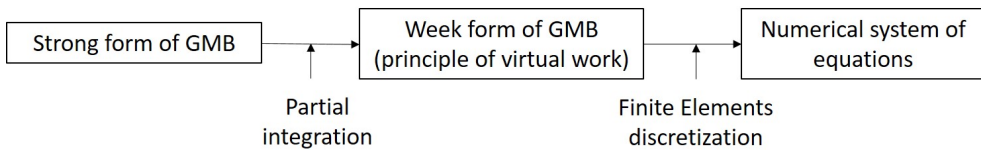


Figure 2.6: From strong formulation of the generalized momentum balance (GMB) to numerical equations.

865 The momentum equations and the traction boundary conditions, usually called the strong form, cannot be directly discretized by FE method. The strong formulation of the GMB equations impose the C_1 continuity conditions on the field variables. Therefore, the solution of this problem does not always exist. This is true especially in the case of complex domains with different material interfaces. In order to overcome these difficulties,
870 weak formulations are preferred. The week formulation of GMB reduces the continuity requirements thereby allowing the use of easy-to-construct and implement polynomials. Because of the reduction in the requirements of function smoothness, the weak forms never give an exact solution but one can obtain a relatively accurate solution with the discretization refinement.

875 From the week form of the GMB equations, the numerical system of equations is formulated by using finite elements interpolants for the mechanical displacement and the test functions. The whole domain is discretization into a number of smaller areas or volumes which are called **finite elements** and their assembly is called a **mesh**. Elements can be of various shapes (as shown in Figure 2.7.b), quadrilateral or triangular in two dimensions, and tetrahedral or hexahedron in three-dimensions.

880 The mechanical displacement is approximated at the discretization points called finite element **nodes**. The nodes are at the vertices of the elements for a linear type, and at the vertices and midsides of the elements edges for a quadratic type (figure 2.7.b). The displacement of each point within an element is interpolated from the values of the displace-

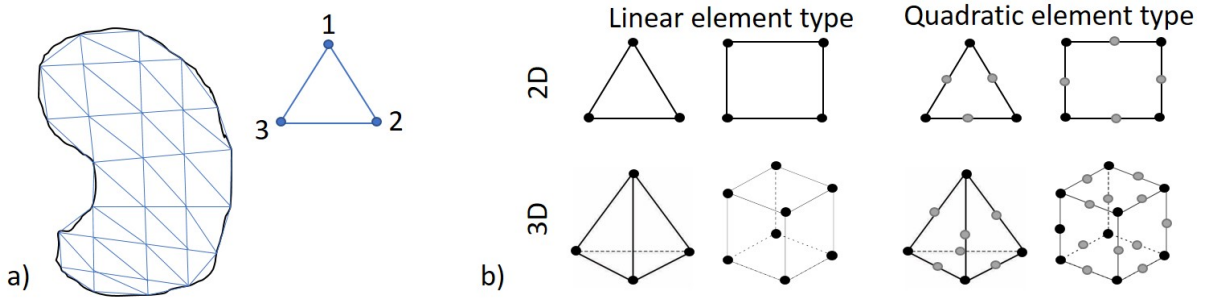


Figure 2.7: a) Discretization of a 2D domain with triangular finite elements :Lagrangian mesh . b) Different types of finite elements

885 ments of the nodes of the element. In this way, the problem of finding the displacement of every point within the body is replaced by the problem of finding the displacements of a finite number of nodes.

As in a Lagrangian mesh the nodes are following the motions, for large deformation the 890 finite elements can be highly distorted. Therefore, the elements shape quality is generally checked all along the deformation process. Several shape parameters for each element type have been proposed such as: aspect ratio, maximum corner angle, Jacobian ratio, skewness, parallel deviation, warping factor. The acceptable limit values of these shape factors are proper to the elements types.

In the following, only the shape parameters of the linear triangular elements are presented 895 (ANSYS, 2017b).

Triangle aspect ratio

The element's shape aspect ratio is computed using only the vertices corner nodes of the 900 element (Figure 2.8). First, two lines are created: one through a node (K) and the midpoint of the opposite edge (K'), the second through the midpoint of the others two edges (J' and I'). Then two rectangles are created, each rectangle have a pair of edges parallel to one of previously defined lines. The rectangle edges have to pass through the nodes and the triangle's edges midpoints. This construction is repeated for each triangle's node resulting in 6 rectangles. The aspect ratio of a rectangle is defined as the ratio between the longer and shorter side. Thus, the triangle's aspect ratio is defined as the maximal aspect ratio 905 over the 6 rectangles divided by squared root of 3.

The best possible aspect ratio is 1 and is represented by an equilateral triangle. An element with an aspect ratio larger than 20 is considered as bad aspect element, large aspect ratio may degrade solution performance.

Triangle maximum corner angle

910 The maximum corner angle is computed using nodes position in 3D space. The best possible maximum corner angle is 60° . An element having a maximal corner angle larger

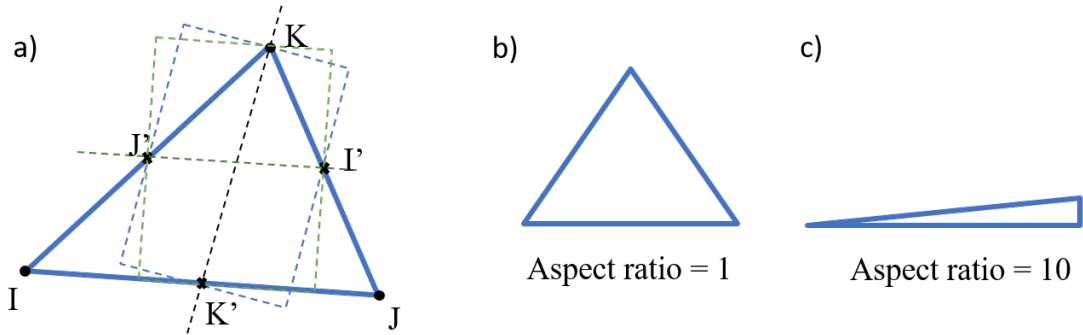


Figure 2.8: Computation of the aspect ratio for a triangle

than 165° is considered as bad shape element, large corner angles may degrade the solution performance. Figure 2.9 shows a triangle with a good (60°) and bad (165°) quality.

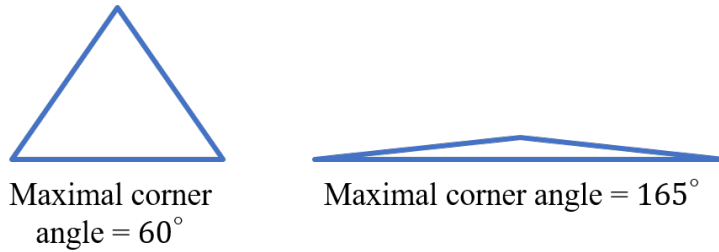


Figure 2.9: Example of triangles with different maximal corner angles.

The aspect ratio and the maximal corner deviation of a tetrahedra is computed using the definition of the same measure on a triangle. The elements shape parameter is assigned as the worst value over the triangles defined by the tetrahedra's faces and cross-sections.

Skewness

The skewness of a triangular element is computed using the equivalent volume deviation method. It is defined as the difference between the optimal and real cell size over the optimal cell size. The optimal size is the size of an equilateral cell with the same circum radius. According to its definition, the value of 0 indicates an ideal cell, from 0 to 0.75 the cell is considered to have a good quality, from 0.75 to 1 the cell is considered to have a bad quality and a value of 1 indicates a completely degenerated cell (Figure 2.10).

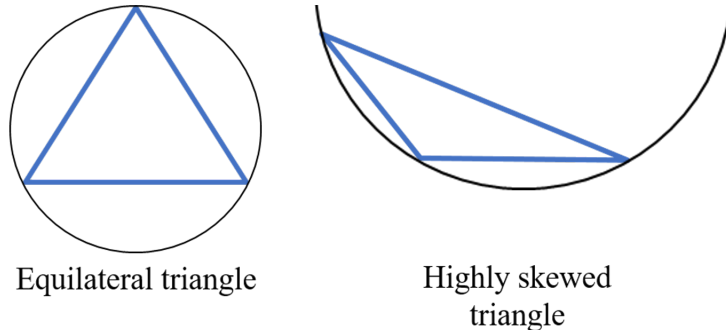


Figure 2.10: Example of triangles with different skewness with the corresponding circum radius.

2.3 Contact mechanics

925 In order to transfer the loads between elements, the nodes have to be connected together. If two bodies are separated with no common nodes, no interaction will occur during the deformation and the bodies will pass through each other. Here, an asymmetric surface-to-surface contact method is used to solve the multi-body interaction problems.

Let's consider two different bodies \mathcal{A} and \mathcal{B} and their occupied domains Ω_A and Ω_B with boundaries Γ_A and Γ_B respectively (see Figure 2.11). Also, we note Ω the domain of intersection of two bodies. The contact interface is the intersection of the surfaces of the two bodies:

$$\Gamma = \Gamma_A \cap \Gamma_B.$$

930 The intersection consists of two surfaces, usually distinguished as **target** and **contact** surfaces. For an asymmetric contact each surface has a single designation and the choice of the surfaces type is made following these next guidelines (the target surface property are enumerated in their priority order):

- if the body \mathcal{A} is stiffer than the body \mathcal{B} , the surface Γ_A defines the target and Γ_B the contact surface;
- if Γ_A is a concave surface getting in contact with the convex surface Γ_B , the surface Γ_A defines the target and Γ_B the contact surface.
- if the surface Γ_A is larger than Γ_B , the surface Γ_A denotes the target and the Γ_B the contact surfaces.

940 For the following, we identify Γ_A as the target surface and Γ_B as the contact surface (Figure 2.11).

Sometimes, the asymmetric contact does not perform satisfactory results and a symmetric contact is needed. When defining a symmetric contact each surface coming in contact is designated to be both, contact and target surface type. Therefore, two set of contact

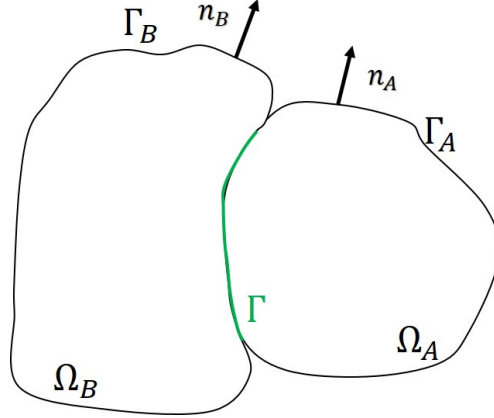


Figure 2.11: Multi-body contact problem.

pairs are defined. The symmetric contact may be used then the distinction between the
945 contact and the target surfaces is not clear or to reduce the contact penetration, however it usually results in a more time-consuming solution.

2.3.1 Contact interface equations

In the case of multi-body interaction, in addition to the standard mechanical governing
950 equations, two more contact conditions have to be fulfilled: the two bodies cannot interpenetrate and the traction must satisfy momentum conservation on the contact interfaces.

Traction conditions

Traction conditions must follow the balance of momentum across the contact interface:

$$t_A + t_B = 0 \quad (2.35)$$

On the contact boundary surface Γ the traction vector is decomposed into its normal and
955 tangential components:

$$t_A^n = t_A \cdot n_A, \quad t_B^n = t_B \cdot n_B$$

$$t_A^t = t_A - t_A^n n_A, \quad t_B^t = t_B - t_B^n n_B$$

Therefore the momentum balance requires:

$$t_A^n + t_B^n = 0, \quad t_A^t + t_B^t = 0 \quad (2.36)$$

Inter-penetrability condition

The bodies implied in a multi-body problem must fulfill the inter-penetrability condition:

$$\Omega_A \cap \Omega_B = \emptyset \quad (2.37)$$

Decomposing the displacement u into its normal and tangential components u^n and u^t respectively the inter-penetrability condition can be written as:

$$t^n \leq 0, \quad u^n - gn_a \leq 0, \quad t^n(u^n - gn_a) = 0 \quad (2.38)$$

Where g is the gap between the two bodies and n_a is the normal to the target surface.

2.3.2 Surface interaction models

When two solid bodies are placed together under a nonzero normal force and acted upon by another with a tangential force, a **friction force** $f_{friction}$ tangential to the interface and opposite to the applied force is created. Depending on whether the applied force can overcome the friction force opposing it, the bodies may or may not move relative to each other. The body motion along the interface is called **sliding**. The **sliding force**, $f_{sliding}$ is the applied tangential force which causes the sliding motion between the two bodies.

Determining whether relative motion will or will not occur requires balancing the involved forces. According to the allowed relative body motion in tangential or normal directions, five types of surface interaction models are distinguished: bonded, rough, no-separation, frictional and frictionless. Table 2.1 resumes each corresponding mechanical behavior. If the body motion is not allowed in normal or tangential direction, once the bodies get in contact, the respective components of traction are equals ($t_A = t_B$), which means that, for a pure **bonded** contact, the two bodies are considered as a unique solid body.

Name	body motion in normal direction	body motion in tangential direction
Bonded	No	No
Rough	Yes	$f_{friction} \gg f_{sliding}$
No-separation	No	$f_{friction} = 0$
Frictionless	Yes	$f_{friction} = 0$
Frictional	Yes	$f_{sliding} > f_{friction}$

Table 2.1: Surface interaction models and corresponding mechanical behaviors

The *frictional* contact behavior is defined using Coulomb friction law. For a continuous body the Coulomb friction model is applied at each point of the contact interface. Considering that bodies \mathcal{A} and \mathcal{B} which are in contact within the surface Γ , then for all $x \in \Gamma$:

$$if \quad \|t^t(x)\| < -\mu_f t^n(x), \quad \Delta u^t = 0 \quad (2.39)$$

$$if \quad \|t^t(x)\| = -\mu_f t^n(x), \quad \Delta u^t = -k(x)t^t(x), \quad k(x) > 0 \quad (2.40)$$

Where μ_f is the material property named **friction coefficient**, Δu^t is the slip incremental in the tangential direction and $k(x)$ is a variable computed from the momentum equation. The condition 2.39 is known as the sticking condition: the tangential traction is less than the critical value, thus no sliding occurs. Reciprocally, condition 2.40 is called the sliding condition.

When a frictionless contact model is used, $\mu_f = 0$, the tangential tractions vanish completely: $t_A^t = t_B^t = 0$. On the contrary, when a rough contact is modeled, the friction coefficient μ_f is equal to infinity, so that the sticking condition is always fulfilled.

In practice, several contact models can be combined to model a physical contact between two bodies.

2.3.3 Contact formulation algorithm: pure penalty model

Pinball region

Contact formulation presents two primary difficulties from a computational point of view. First, the traction conditions have to be estimated for each considered frictional model. And second is the unpredictability of regions which will get in contact with each other during the deformation process.

The region of contact depends on materials properties and imposed boundary conditions; therefore, it is difficult to know a priori where the surfaces will be in contact. To formulate analytic equations, one has to know exactly the nodes involved in the contact process. Therefore, during body deformation, the program calculates if the contact is *opened* or *closed*. The status is defined using a sliding pinball (Figure 2.12). The pinball slides over the contact surface nodes and searches for the target surface. If the node to surface distance is smaller than the pinball radius, the contact is considered to be closed (Figure 2.12, green nodes) otherwise the contact is considered to be opened (Figure 2.12, gray nodes).

Gap and penetration measures

Let's consider a point x_B bellowing to the body surface Γ_B and x_A the intersection point of the surface normal n_B with the surface Γ_A (Figure 2.13). The point to surface distance $d_1(x_B, \mathcal{A})$ is defined as:

$$d_1(x_B, \mathcal{A}) = \|x_B - x_A\| = \left[\sum_{i=1,2,3} (x_B^i - x_A^i)^2 \right]^{\frac{1}{2}} \quad (2.41)$$

If the intersection point x_A is located inside the pinball area, the node to surface distance define the amount of **gap** or **penetration** of the respective node (Figure 2.13).

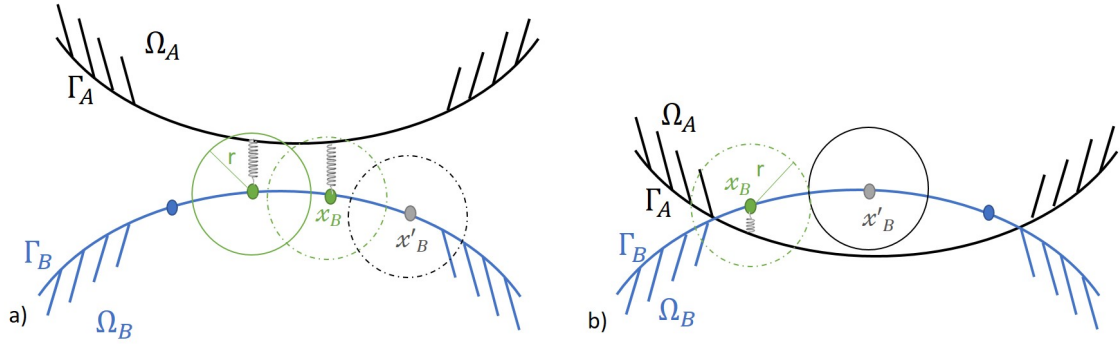


Figure 2.12: Contact status update using a pinball of radius r . Green nodes - updated nodes to closed contact status; gray nodes - updated nodes to open contact status; blue nodes - nodes which contact status need to be updated

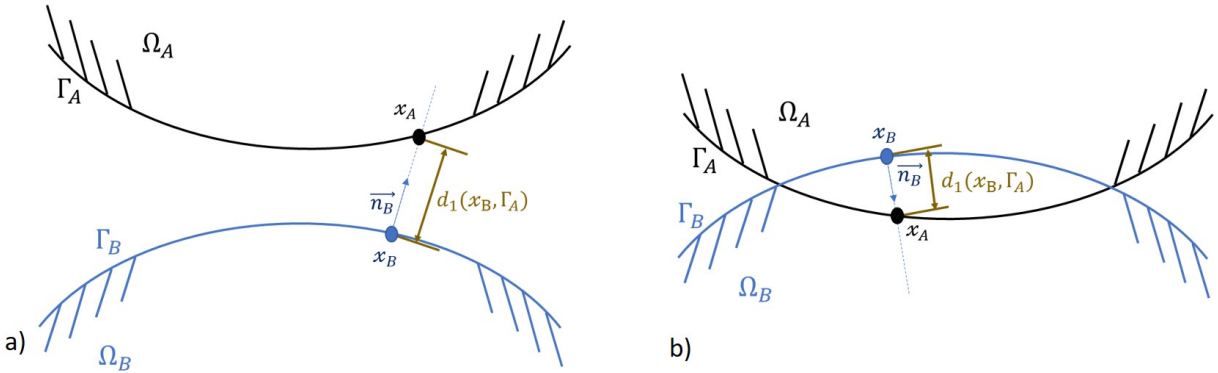


Figure 2.13: a) Body \mathcal{A} and body \mathcal{B} are close but not in contact. The $d_1(x_B, \mathcal{A})$ measure define the gap between the bodies at point x_B . b) Body \mathcal{B} have penetrated the body \mathcal{A} . The $d_1(x_B, \mathcal{A})$ measure gives the penetration at point x_B .

Computing the gap or penetration at single points increase numerical instabilities.
 1015 Therefore, in this work, the gap and penetration are computed in an averaged manner over the projected surface areas. Figure 2.14 show the projected surface areas (c) obtained by the intersection of the target surface areas (a) with the projected contact surface areas (b) over the target areas (a).

1020 The interested reader is referred to ANSYS contact technology guide (ANSYS, 2017a) for more details on the contact modeling.

Finite element mesh

For the finite element computation, contact and target surfaces have to be discretized with 2D linear or quadratic elements (Figure 2.7) consistent with the underling 3D element

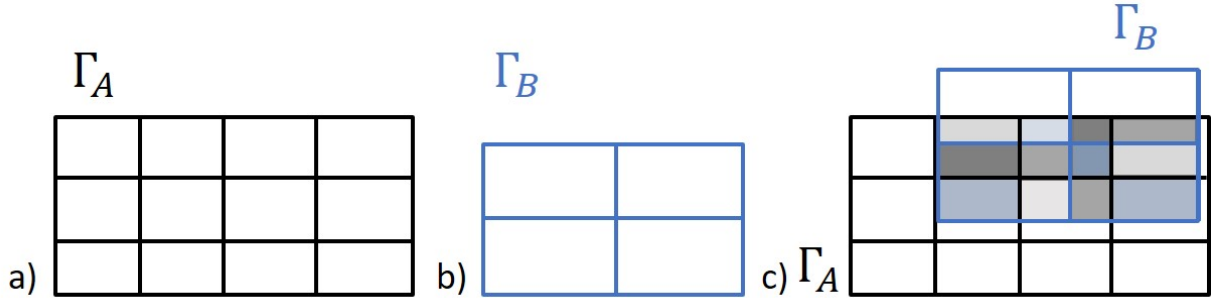


Figure 2.14: The contact surface projection over the target surface: a) Target discretized area; b) contact discretized area; c) intersection of the projected surfaces.

1025 mesh. The elements are named contact and target elements respectively. They have no material properties apart the friction coefficient μ_f . The stress-strain as well as the gap or penetration measures are computed for each mesh node of the discretized surface.

Pure Penalty method

1030 In this manuscript, one of the most popular mathematical expression of contact compatibility conditions is used, namely the penalty method. With such a method, additional contact properties are defined to manage contact behavior: a normal stiffness factor, opening stiffness factor, and a tangential stiffness factor. Such factors play an important role in the numerical computation but have no physical meaning.

1035 The penalty method uses a spring like relationship to introduce a force for all nodes pairs (contact-target) that are defined to be in closed contact (Figure 2.41). The contact force is computed using the following expression:

$$f_c = k_c d \quad (2.42)$$

1040 where d represents the penetration or gap amount and k_c is the normal stiffness factor or the opening stiffness factor respectively. The tangential stiffness factor works in the same way enforcing the responding frictional force. Even if physical contacting bodies do not interpenetrate ($d = 0$), some finite amount of penetration, $d > 0$, is required mathematically to maintain equilibrium.

1045 The biggest challenge here is that the magnitude of the stiffness contact factors is completely unknown beforehand. The contact force at each node have to be large enough to push the contact surface back to the target surface and eliminate unwanted penetration or gap. In the same time, if the contact force is too large, it pushes the contact surface far away from the pinball region causing error and solution instabilities.

2.4 Breast biomechanical model: overview

Biomechanical modelling of breast tissues has been widely investigated for various medical applications such as surgical procedure training, pre-operative planning, diagnosis and clinical biopsy, image guided surgery, image registration, and material parameter estimation 1050 (Table 2.3). For the last 20 years, several research groups have presented their breast models based on finite elements modeling. The complexity and relevance to breast anatomy of each model depend on the research purposes for which it was designed.

Several groups have proposed biomechanical breast models to register uncompressed 1055 volumetric breast data to the compressed one (Han et al., 2012; Ruiter et al., 2006; Sturgeon et al., 2016) or to compressed projection mammographic data (Kellner et al., 2007). Within this framework, the authors modeled the breast deformation from prone to compressed prone position assuming linear elastic materials, zero residual stress and Dirichlet boundary conditions. However, compression-like breast deformation is too limited to characterize 1060 global breast mechanics.

Applications such as image guided surgery or preoperative planning imply a wider range of deformations. Therefore biomechanical breast models capable of estimating gravity induced deformation between different body position were proposed, for example from supine to prone positions (named also multi-loading gravity simulations) (Gamage et al., 1065 2012; Georgii et al., 2016; Eiben et al., 2016c). Considering the involved large deformation, these models need to be more accurate with respect to mechanical and anatomical breast properties. In this respect, a patient-specific model is needed considering more personalized boundary conditions, material models and a better representation of breast anatomy.

As described in Section 2.1, to build such a mechanical breast model, one need to 1070 provide the breast geometry in a **reference configuration**, the **constitutive models** of tissues composing the volume and the **boundary conditions**. The definition of all these variables has a significant impact on model accuracy.

2.4.1 Breast reference configuration

A large number of existing patient specific models are using volumetric data from MR 1075 images Carter (2009b), Kellner et al. (2007), Conley et al. (2015) Eiben et al. (2016b), Martínez-Martínez et al. (2017) or CT images Palomar et al. (2008), Sturgeon et al. (2016) to design the breast geometry. During such exams, the acquired breast tissues are already deformed with deformation that significantly change breast geometries, for example if the patient is in a supine or in a prone position. Moreover, the deformed breast configurations 1080 include already the initial pre-stresses which are generally unknown and are extremely difficult to measure in clinical conditions.

To model the breast tissues deformation under gravity loading, the reference state is chosen to be the breast geometry in a stress-free configuration, i.e. without being deformed by any force, including gravity. The breast stress-free geometry is practically impossible to 1085 measure; therefore, several estimation methods have been proposed. The four most used

ones are described below.

Inverse gravity

(Palomar et al., 2008; Sturgeon et al., 2016) used the inverse gravity method to estimate the stress-free geometry from the prone position measured during the exam. In their work, the authors just reversed the gravity effects without considering the initial stresses already included in the breast prone configuration. According to Eiben et al. (2014) the inverse gravity methods gives a poor approximation of the breast reference state and can be used only with small deformations or highly constrained models.

Breast neutral buoyancy configuration

Assuming that breast density is equal to water density, Rajagopal et al. (2008) compute the breast stress-free configuration by imaging the breast immersed in water. Following the same physical assumptions, Kuhlmann et al. (2013) proposed to estimate the stress-free configuration by applying a hydro-static distributed load on the breast surface collected in a prone configuration. Even though the estimated geometries are accurate enough, these methods are time-consuming and is difficult to transpose in a clinical framework.

Prediction-correction iterative algorithm

The prediction-correction iterative method was first proposed by (Govindjee and Mihalic, 1998) and adapted later by Carter (2009b) and Eiben et al. (2014). The original method is based on the prediction-correction iterative scheme represented in Figure 2.15. The first approximation of the breast reference configuration is estimated by applying the inverse gravity method on the prone breast configuration (see above). Then, a numerical breast prone configuration is computed and compared to the corresponding measured one. The difference between the two prone geometries (The measured one and the simulated one) is used to update the reference breast configuration. The process is repeated until the convergence is achieved (i.e. then the difference is minimal). These methods were validated using the neutral buoyancy breast shape.

Inverse FE algorithm

Pathmanathan et al. (2008) and later Vavourakis et al. (2016) proposed an analytic computation of the breast reference state by reparametrizing the equilibrium equation and by solving a finite element formulation of the inverse motion. The model provides good estimates of breast reference configurations but needs large numerical resources. Eiben et al. (2014) showed that the prediction-correction iterative algorithm and the inverse FE algorithm are similar in terms of resulting accuracy.

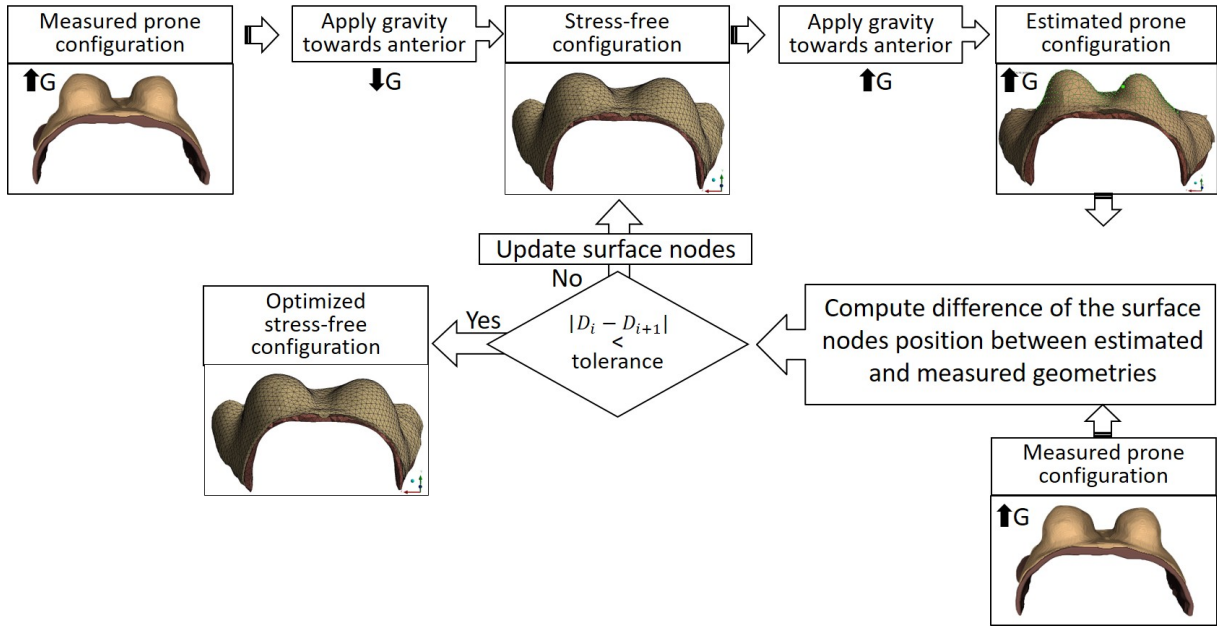


Figure 2.15: Prediction-correction algorithm

2.4.2 Constitutive models

¹¹²⁰ Global breast mechanics is governed by breast tissue compositions and their individual mechanical properties. The breast soft tissues are known to be incompressible, nonlinear, anisotropic, and viscous materials. However, according to Wellman et al. (1999) the breast tissues viscosity can be neglected when the mechanical load is applied within short time scales.

¹¹²⁵ Under large compression and body position changes, the breast volume can vary due to blood flows. Thus, soft tissues are frequently modeled as quasi-incompressible materials with a Poisson ratio ranging between $\nu = 0.45 - 0.5$. The influence of the Poisson ratio within linear constitutive models was studied for breast by Tanner et al. (2006); according to the authors, the best estimates are obtained with high Poisson ratio ($\nu = 0.495, 0.499$).
¹¹³⁰ The breast tissues are predominately composed of water; therefore, the density is considered to be equal to 981 kg/m^3 .

For the last decades several constitutive models were used to model the breast tissues response to an external force: exponential elastic (Azar et al., 2002), Neo-Hookean hyperelastic (Carter, 2009b; Rajagopal et al., 2010b; Sturgeon et al., 2016; Eiben et al., 2016a; Han et al., 2014; Garcia et al., 2017), Money-Rivlin (Samani et al., 2007; Tanner et al., 2006; Carter et al., 2012; Martínez-Martínez et al., 2017). Eder et al. (2014) compared the most popular models in a multi-loading gravity simulation; according to the authors, the Neo-Hookean model proposed by Rajagopal et al. (2008) gives the best estimates.

Glandular and adipose tissues biomechanical properties

1140 Multiple studies have shown that breast composition, and so its mechanical behavior undergo substantial changes during woman lifetime (section 1.1.4). The first studies on mechanical proprieties estimation of breast tissues were done in diagnosis purposes. When the breast is developing benign or malign disorders, its mechanical properties differ from the ones of the normal breast tissues. In a study of 142 samples, bellowing to 4 type of
1145 tissues, Krouskop et al. (1998) found that depending on the pre-compression level, Young moduli of invasive carcinoma is from 5 to 25 times larger than the one of normal adipose tissue (from 5% to 20% strain levels).

Later, several research groups (Table 2.2) have studied the elastic moduli of adipose and glandular tissues. The breast tissues elastic parameters range between 0.1 kPa and
1150 271.8 kPa. Such huge variation may be explained by the differences in the experimental set-up used to estimate stiffness, but also by the participant's physical condition, age or period of the menstrual cycle. For example, Han et al. (2012), though using the same FE method, found significantly inter-individual variability, with the shear moduli ranging between 0.22 – 43.64kPa. Lorenzen et al. (2003) showed that during the menstrual cycle,
1155 due to the hormonal changes, the elastic properties of the glandular tissues can change by about 30%.

An important difference in estimated values of breast elastic moduli is observed between the linear elastic and hyperelastic models. If only in-vivo studies with Neo-Hookean material models are considered, the range of the adipose and glandular shear moduli is significantly lower than 50kPa.
1160

Carter (2009b) compared a one parameter Neo-Hookean potential function with a five parameters Money-Rivlin potential function for various material properties. The multi-loading gravity simulations were thus performed on 3 subjects. According to the authors, even for parameters 10 times softer than the literature (Samani et al., 2001), the Money-
1165 Rivlin model underestimates the tissues deformation by at least 75% when the subject is re-positioned from the supine to the prone positions. The best estimates were given by the Neo-Hookean model with the initial shear moduli equal to 0.2kPa.

Previously listed researches clearly showed the variability of elastic moduli of the same tissue between and within individuals. Eder et al. (2014) made a larger analysis including
1170 all material models proposed in the literature. According to authors, many of them are too stiff permitting not enough deformation within the gravity loading. This study has shown that the most reliable elastic moduli values are the ones given by Rajagopal et al. (2008) (Table 2.2).

Muscle biomechanical properties.

1175 Muscle is a kinematically, geometrically, and materially complex tissue. Muscle mechanical behavior depends on its contractile active and passive elastic properties (Nordez and Hug, 2010). In biomechanics the muscle is modeled using complex models as Hill-type models (Zajac, 1989), Feldmans lambda model (Feldman, 1986) which are considering the variation

Ex-vivo estimation				
Author	Method	Material model	material properties	
			Adipose kPa	Glandular kPa
Krouskop et al. (1998)	Indentation-5%	Linear elastic	$\lambda = 19 \pm 7 \text{ kPa}$	$\lambda = 33 \pm 11 \text{ kPa}$
Krouskop et al. (1998)	Indentation-20%	Linear elastic	$\lambda = 20 \pm 6 \text{ kPa}$	$\lambda = 57 \pm 19 \text{ kPa}$
Wellman et al. (1999)	Indentation - 5%	Linear elastic	$\lambda = 6.6 \text{ kPa}$	$\lambda = 33 \text{ kPa}$
Wellman et al. (1999)	Indentation - 15%	Linear elastic	$\lambda = 17.4 \text{ kPa}$	$\lambda = 271.8 \text{ kPa}$
Azar et al. (2002)	Indentation	Exp. elastic	$b = 4.46 \text{ kPa}; m = 7.4$	$b = 15.1 \text{ kPa}; m = 10$
Samani and Plewes (2004)	Indentation	Linear elastic	$\lambda = 3.25 \pm 0.91 \text{ kPa}$	$\lambda = 3.24 \pm 0.61 \text{ kPa}$

In-vivo estimation				
	MRE	Linear elastic	$\lambda = 17 - 26 \text{ kPa}$	$\lambda = 26 - 30 \text{ kPa}$
Van Houten et al. (2003)	MRE	Visco-elastic	$\mu = 2.9 \pm 0.3 \text{ kPa}$	
Sinkus et al. (2005)	MRI-FEM	Neo-Hookean	$\mu = 0.16 \text{ kPa}$	$\mu = 0.26 \text{ kPa}$
Rajagopal et al. (2008)	MRI-FEM	Neo-Hookean	$\mu = 0.25 \text{ kPa}$	$\mu = 0.4 \text{ kPa}$
Carter (2009a)	MRI-FEM	Neo-Hookean	$\lambda = 1 \text{ kPa}$	$\lambda = 0.22 - 43.64 \text{ kPa}$
Han et al. (2012)	MRI-FEM	Neo-Hookean	$\mu = 0.1 \text{ kPa}$	
Gamage et al. (2012)	MRI-FEM	Hooke's law	$\lambda = 0.25 \text{ kPa}$	$\lambda = 2 \text{ kPa}$
Griesenauer et al. (2017)	MRI-FEM			

Table 2.2: Material properties for adipose and glandular tissues.

of muscle elasticity in function of muscle state. In breast biomechanical models the muscle is combined with the thoracic cage and is frequently considered as a rigid breast support. In most of models, the pectoral muscle is modeled by imposing zero-displacement conditions on nodes closer to the chest wall (Samani et al., 2001; Chung et al., 2008; Rajagopal et al., 2010a) or by allowing them to slide along the chest wall line (Han et al., 2014; Georgii et al., 2016).

The muscle is nonlinear, anisotropic, incompressible material. The bibliographic data

on static mechanical properties of the muscle-tendon unit assessed by supersonic shear wave imaging elastography state a Young's modulus in range of $20kPa$ to $300kPa$ depending on the muscle location and subject's physical condition (Lima et al., 2018). The muscle shear moduli on the upper trapezius was studied by Leong et al. (2013), according to authors the muscle shear elasticity at rest was $17.11 \pm 5.82kPa$, and this increased to $26.56 \pm 12.32kPa$ during active arm holding at 30° abduction.

Skin biomechanical properties

Several studies have shown the importance of skin in biomechanical breast modeling. According to Carter (2009b), a model which includes the skin estimates better the tissues deformation under gravity loading.

Sutradhar and Miller (2013) published a complete study of breast skin estimating its elasticity for 16 different breast regions. The study was done on 23 female volunteers aging from 29 to 75 years. The authors found that the skin elastic moduli range between 15 – $480kPa$ with an average of $334 \pm 88kPa$. The elastic moduli in the lateral region (mean $370kPa$) has the highest value followed by the superior region (mean $355kPa$); the inferior region (mean $331kPa$) follows next, with the medial region having the lowest value (mean $316kPa$). However, no significant variation of elastic moduli in radial direction was found.

Other researches on skin elasticity are available, but they are not specific to the breast skin. Hendriks et al. (2006) estimated in-vivo skin properties by suction testing. The skin was considered as a homogeneous, isotropic, incompressible, hyperelastic material. The study was performed on 14 subjects and the obtained average of elastic moduli for skin was $58.4kPa$.

The estimation of the breast skin elasticity by the means of finite elements using Neo-Hookean potential function has resulted in softer materials model. Carter (2009a) found an initial shear modulus equal to $16kPa$, whereas Han et al. (2014) found that for the five studied subjects the skin shear moduli ranged between $2.47kPa$ and $5.78kPa$.

Fascias and ligaments biomechanical properties

The surrounding breast fascias and the supervisory ligament form the breast support matrix. These structures are well described for surgical purposes (thickness, location etc), however little is known about their mechanical properties. The first biomechanical breast model taking into account the effect of Cooper's ligaments was proposed by Azar et al. (2002) and took up later by Pathmanathan et al. (2008) and Han et al. (2012). The authors designed a new material model for fatty tissues including the anisotropic behavior of breast ligaments. Later, Georgii et al. (2016) come up with a spring-mass generic model for the breast support matrix. According to the authors, including the ligaments into the finite elements breast model have increased the robustness of the prone-supine simulation with respect to the input parameters.

To our knowledge, there are no experimental data describing the mechanical properties

1225 of breast superficial fascia. An approximation of the elastic moduli of Cooper's ligaments is given by Gefen and Dilmoney (2007) by extrapolating from known ligamentous structure in the human body. The authors estimated the elastic moduli of suspensory ligaments to relay between $80 - 400 \text{ MPa}$

1230 Fibrous tissues get their elasticity from elastin elastic fibers and their structural support from collagen fibers. As reported by Riggio et al. (2000), the superficial fascia is made up of both collagen and elastin fibers. In contrast, the Cooper's ligaments appeared to be composed almost of collagen fibers. The mechanical properties of a single collagen fiber from a rat tail were studied by Wenger et al. (2007); according to the authors the corresponding elastic moduli range between 5 GPa and 11 GPa . Other studies on biomechanical 1235 characterization of human body superficial fascia are available in the literature. The most frequently studied structures are the plantar fascia and foot ligaments, with a Young's moduli ranging between $0.1e^{-3} \text{ MPa}$ (Gefen, 2003) and 700 MPa (Cheung et al., 2004).

2.4.3 Boundary conditions

Dirichlet conditions are usually used to constrain the sternum/axilla ends and the posterior 1240 surface of the breast or the thoracic cage if the muscular tissues are considered (Griesenauer et al., 2017; Rajagopal et al., 2008; Pathmanathan et al., 2008; Gamage et al., 2012; Griesenauer et al., 2017). As reported by Carter (2009b) the zero-displacement boundary conditions in a multi-gravity loading framework result in an over-constrained model; in that case sliding conditions on the mesh nodes corresponding to the chest wall have to be 1245 considered.

Later, several teams using biomechanical breast models for multy modality image registration or surgical planing showed that including the sliding boundary conditions (Georgii et al., 2016; Han et al., 2014) improves the registration accuracy. However the most studies in which the biomechanical model is designed for breast compression, the tissues sliding 1250 over the chest wall is neglected and fixed boundary conditions are usually assumed (Sturgeon et al., 2016; Martínez-Martínez et al., 2017).

2.4.4 Summary

During the last decades, several breast biomechanical models were proposed. However, only a small part of them (Carter, 2009b; Gamage et al., 2012; Han et al., 2014) were evaluated 1255 with respect to real tissues deformations. As we intend to build-up a subject specific breast biomechanical model capable of estimating multi-loading gravity deformations, we will only consider as relevant the biomechanical models that were evaluated and compared with real data. In this chapter, three biggest challenges were identified: the estimation of the breast reference geometry, the estimation of patient specific material properties and 1260 the definition of the boundary condition and namely the breast-muscle interface. Today's outstanding breast biomechanical models are represented by the next three models: Eiben et al. (2016c), Han et al. (2014), Gamage et al. (2012).

Gamage et al. (2012) proposed a finite elements model capable to estimate the supine breast configuration from the prone one. The breast stress-free configuration was estimated using a prediction-correction iterative algorithm optimization process, in this purpose the skin surfaces on prone configuration was used as ground-truth. Contrariwise, the material constitutive parameters were identified using the skin surface on supine breast configuration by applying a non-linear optimization algorithm. Breast tissues sliding over the chest wall was considered partially by modeling the pectoral muscle as a soft structure and including it into the optimization process. The models were evaluated for the supine breast configuration by computing the root-mean-squared error (RMSE) from the point to surface distance between the estimated and measured data. Conform to the authors, the breast supine geometry was estimated within an RMSE of 5mm (maximal distance of 9.3 mm).

In the same time, Han et al. (2014) developed a breast biomechanical model for image registration. The estimates of supine breast configuration were computed for five subjects, and the accuracy was assessed by computing the Euclidian distance between anatomical landmarks. The mean Euclidian distance range between 11.5 mm and 39.2 mm (maximal Euclidian distance ranged between 20.3mm and 61.7mm). The authors modelled the elongation of the pectoral muscle using a contact sliding model. Only the material constitutive parameters were adapted to the patients breast mechanics, the stress-free breast geometry being estimated by inverse gravity.

Finally, Eiben et al. (2016c) proposed a new model to estimate the up-standing breast configuration from the prone one. The model was evaluated on 3 subject. The patient specific stress-free geometry was computed using an inverse finite elements u-p formulation. The material parameters were optimized such that the best fit in supine configuration is obtained. The estimates quality was measured in terms of the mean Eulerian Distance between manually selected internal landmarks. Thus, the supine breast configuration was estimated within a mean distance ranging between 12.2mm and 19.8mm. The model evaluation for the up-standing configuration was not presented.

A new biomechanical breast model is proposed in the next chapter considering the patient specific breast geometry and elastic properties as proposed by the previous models. In addition, the breast tissues sliding over the chest wall is modeled by including new anatomical structures as superficial fascia and suspensory ligaments. We believe that global breast mechanics are driven by these stiff structures. Finally, the model will be evaluated by confrontation with real data collected from MR images.

CHAPTER 2. BIOMECHANICAL BREAST MODELING
STATE OF THE ART

Authors	Application	FE mesh	Material models	Boundary conditions	Stress-free config.
Azar et al. (2002)	Computer assisted breast surgery	8-Node hexahedrons (trilinear isotropic elements)	Skin-elastic adipose/glandular-hyperelastic polynomial	Sliding between breast - thorax and breast-paddle	Prone breast geometry
Rajagopal et al. (2007)	Breast compression	8-Node hexahedrons (tricubic Hermite elements)	Homogeneous , Neo-Hookean model	Zero-displacement BC	Buoyant breast in water
Pathmanathan et al. (2008)	Image registration	8-Node hexahedrons (trilinear elements)	Homogeneous polynomial Skin exponential hyperelastic	Zero-displacement on muscle; Compression with imposed displacement	Inverse FE algorithm
Han et al. (2014)	Image registration	4-Node tetrahedrons	Muscle, glandular, fatty, skin - Neo-Hookean model	Sliding on pectoral muscle	Inverse gravity
Gamage et al. (2012)	Computer assisted breast surgery	8-Node hexahedrons (tricubic Hermite elements)	Homogeneous+ Neo-Hookean incompressible model	Zero-displacement BC on rib cage surface, Sternum, axilla ends, shoulder	PC iterative algorithm
Patete et al. (2013)	Computer assisted breast surgery	4-Node tetrahedrons (trilinear isotropic elements)	Adipose , glandular, skin	Zero-displacement BC on the chest wall	PC iterative algorithm
Kuhlmann et al. (2013)	image registration	4-Node tetrahedrons	Adipose, glandular-linear gel-like (Eulerian formulation); Skin - hyperelastic material (Lagrangian formulation)	Zero-displacement chest wall	PC iterative algorithm
Georgii et al. (2016)	Surgery simulation	8-Node hexahedrons, 2-node 3D spars	homogeneous elastic material, Cooper's ligaments-generic mass-spring model	sliding BC (breast on the pectoral muscle)	NA
Eiben et al. (2016c)	Surgery outcome prediction	4-Node tetrahedrons	Fatty , Hookean model; skin-exponential hyperelastic	Zero-displacement BC	Inverse FE algorithm
(Garcia et al., 2017)	3D breast lesion localization	4-Node tetrahedrons	adipose, glandular - Neo-Hookean models	zero-displacement BC	Prone breast configuration

Table 2.3: Breast biomechanical models

A NEW BIOMECHANICAL BREAST MODEL EVALUATED ON REAL DATA

The state of the art in breast finite element modeling was provided previously. Three models were identified representing the cutting-edge technologies in the field. The authors used prone MRI to estimate the breast reference geometry, then the patient-specific constitutive parameters are chosen such that the best fit between the supine configuration estimate and the corresponding measured breast geometry is obtained. The models were evaluated using the measured and the estimated positions of superficial fiducial landmarks or internal anatomical landmarks in the supine breast configuration. As the optimization and evaluation processes are based on the same data, the model limitations may be underestimated. For a better assessment of the model accuracy the evaluation on a third breast configuration is suitable

This chapter introduces a new biomechanical model developed by combining the best practices and concepts proved by previous works. To be as realistic as possible, our model considered breast heterogeneity, sliding boundary conditions, initial pre-stresses and personalized hyper-elastic properties of breast tissue. In addition, new types of soft tissue were included representing the breast support matrix composed of suspensory ligaments and fascias. Moreover, our model was built using prone and supine breast configurations and was evaluated in supine tilted configuration (45 deg) of the same volunteer.

In the first part of this chapter the data acquisition protocol is described and details on numerical methods and softwares used to extract the patient-specific breast geometry are given. Next, the different components of the finite element mesh are presented and the mesh quality is assessed using shape parameters. Then, the assumptions on boundary conditions and materials models are explained. Finally, the model optimization process is detailed and results on patient-specific parameters and breast reference configuration are presented.

3.1 Geometry extraction

Geometry extraction is the first step in FE analysis, and it consists of obtaining the 3D surfaces of the breast. We use the MR images to obtain the patient-specific breast volumes and the surrounding soft tissues distribution. Prior to surface extraction, the MRI volume is segmented and mapped to a single reference system. The next section describes the imaging acquisition protocol and the numerical method used to generate the 3D patient-specific breast geometry.

3.1.1 Data acquisition

The images were acquired with a Siemens 3T scanner with T2 weighted image sequences. The in-plane image resolution was 0.5x0.5 mm, and the slice thickness was 0.6 mm. During this acquisition, the contact between the breasts and the contours of the relatively narrow MRI scanner tunnel, or with the patient body (arms, thorax), was minimized. Three different positioning configurations are considered: prone, supine and supine titled (45 deg). These positions were chosen to assess the largest possible deformations

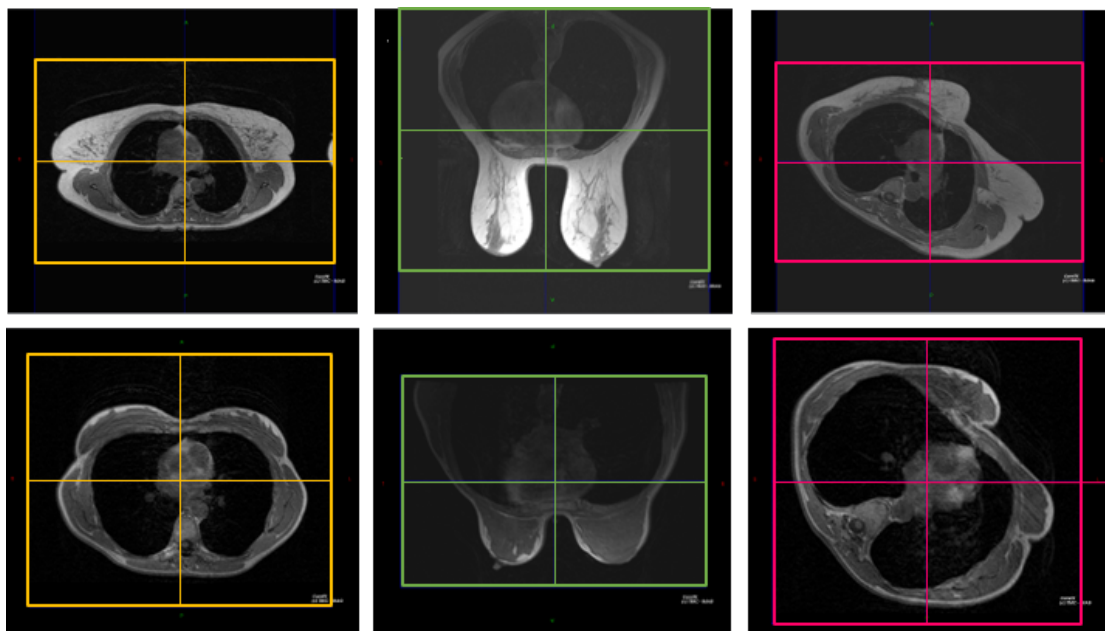


Figure 3.1: MRI images in three breast configuration: first line- subject 1; second line- subject 2

Two volunteers agreed to participate in a pilot study approved by an ethical committee (MammoBio MAP-VS pilot study). The volunteers are 59 and 58 years old and have A-cup (subject 1) and F-cup (subject 2) breast size respectively.

The volunteers were also asked to provide the compression force and breast thickness as measured on their most recent mammograms. Such data are summarized in Table 3.1.

	Subject 1		Subject 2	
	Right breast	Left breast	Right breast	Left breast
Force (N)	21.9	40.9	94.8	56.6
Breast thickness (mm)	47	42	50	49

Table 3.1: Compression force and breast thickness for both subjects for a cranio-caudal mammogram

3.1.2 Image segmentation

A semi-automated active contour method proposed by ITK-Snap software was used to segment the pectoral muscle and the breast tissues from MR images (Yushkevich et al., 2006). The segmentation process for one tissue type is performed progressively by small regions of interest (ROI, see Figure 3.2.a). For each ROI the segmentation of one tissue takes place in 3 steps (Figure 3.2):

1. Firstly, the random forest algorithm (Ho, 1995) is used to compute a new synthetic volume consisting of the probability of each pixel to belong or not to the segmented tissue. The training data set is manually selected by the user and include state and space characteristics such as voxel grey intensity, voxel's neighbors intensity (with variable radius of neighboring) and voxel position ($x; y; z$) (Figure 3.2.c).
2. Secondly, spherical seeds point with variable radius are placed on the new synthetic volume to mark the connected components bellowing to the segmented tissue (Figure 3.2.d).
3. Finally, the placed seed point will evolve in the 3D space with a speed and direction derived from the pixel intensity and sign in the synthetic volume (Figure 3.2.d).

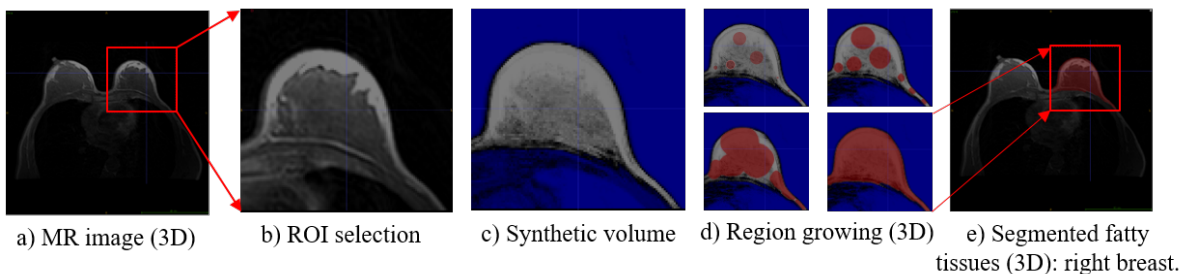


Figure 3.2: Breast tissues segmentation on the breast MRI of the second volunteer. Prone breast configuration. White voxel - the voxel belongs to breast tissue ; blue voxel - the voxel don't belongs to fatty tissue

After segmentation, an additional manual correction was performed to refine components boundaries. Simple erosion and dilatation operations were applied on breast and

1360 muscle segmented volumes in order to obtain smoother connected components. Then, to avoid tissues overlapping at muscle-breast juncture border binary operations were used.

The process was repeated for both volunteers and for each breast configuration: supine, prone and supine tilted. The extracted surfaces in supine and prone configurations are used for model definition and optimization, the last surface, in supine tilted configuration, is
1365 used for model evaluation.

3.1.3 Image registration

During the imaging acquisition process, the subject is moved in and outside the MRI scanner tunnel. Therefore, the breast not only undergoes an elastic deformation, but also a rigid transformation. Prior to image acquisition, four landmarks are fixed on the chest
1370 wall. The landmarks are placed on sternum and inframammary fold lines; these regions are indeed known to be rich in fibrous ligaments limiting the soft tissue elastic deformation. To assess the body position changes, a rigid transform is computed by minimizing the Euclidian distance between the two configurations of the four points defined by the four landmarks. The transformation is estimated using the iterative closest point (ICP)
1375 algorithm proposed by ITK library.

However, because of the small local deformations of skin soft tissues in the chest wall region, the computed rigid transformation is not accurate enough. Therefore, a second registration step is performed by aligning the bone structures of the anterior part of thoracic cage from prone and supine tilted positions to the supine one. The muscular tissues mask
1380 previously segmented are used in order to remove body soft tissues. The image registration is implemented using the gradient descent based algorithm minimizing the images cross correlation (ITK library).

Figure 3.3 shows overlapping prone-supine and supine tilted-supine breast images in the transversal plane after registration. The anterior part of the chest line is well aligned,
1385 however there are some differences because of elastic thoracic cage deformations due to hand positions or body-mass force repartition.

In a multi-gravity loading finite element simulation, the gravity force is applied to the whole model as a body force. The gravity force orientation can be broken down into three components of the Cartesian coordinate system labeled X, Y, and Z directions (Figure 3.4).
1390 The supine configuration was chosen as a reference state, therefore the gravity loading direction was set in that configuration to be oriented on the inverse direction of the Y axis (postero-anterior direction, Figure 3.4): $\gamma_s = (0, -1, 0)$. The gravity loading direction for the two other positions are given by the rigid transformation computed by images registration: $\gamma_p = (0.037, 0.985, -0.165)$ direction vector for gravity in prone position and
1395 $\gamma_{st} = (-0.744, -0.667, 0.023)$ direction vector for supine tilted position for the second volunteer.

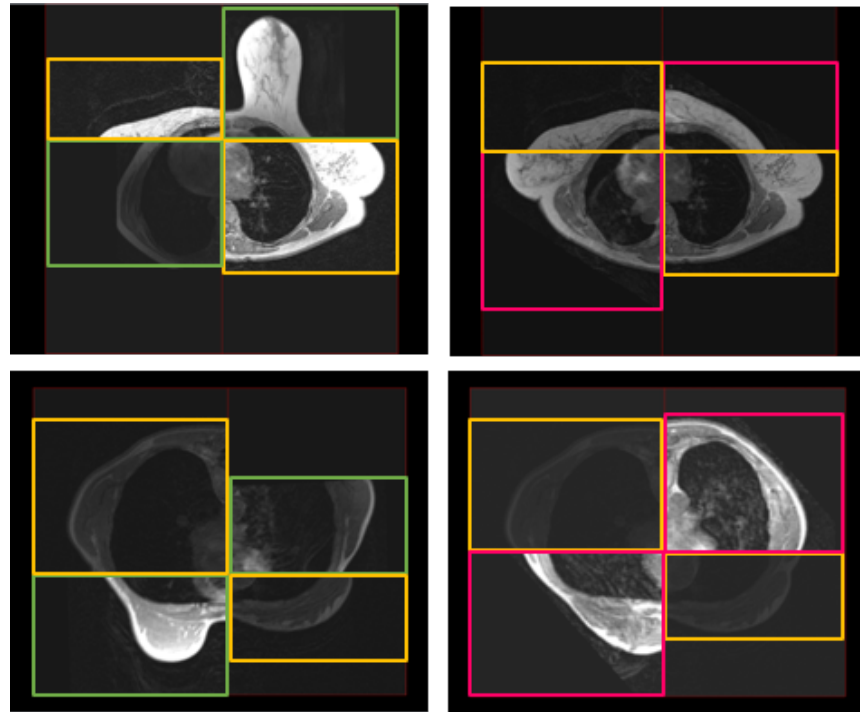


Figure 3.3: Registered MRI images: first line- subject 1; second line- subject 2; first column - prone configuration versus supine; second column - supine tilted versus supine

3.1.4 Patient-specific 3D geometry

The breast patient-specific geometry was created based on the MR images in supine configuration. Following image segmentation (Figure 3.5.b), the outer shape of labeled regions are subsequently discretized by 2D triangular elements. We used the semi-automatic Skin Surface module proposed by SpaceClaim Direct Modeler to convert the mesh surfaces to non-uniform rational basis spline (NURBS) surfaces. The NURBS are averaging curves between points, therefore they are smoother and easier to use in mechanical applications. The resulting two surfaces represent the 3D geometries of the breast and the thoracic cage with muscle (Figure 3.5.c).

1400

1405

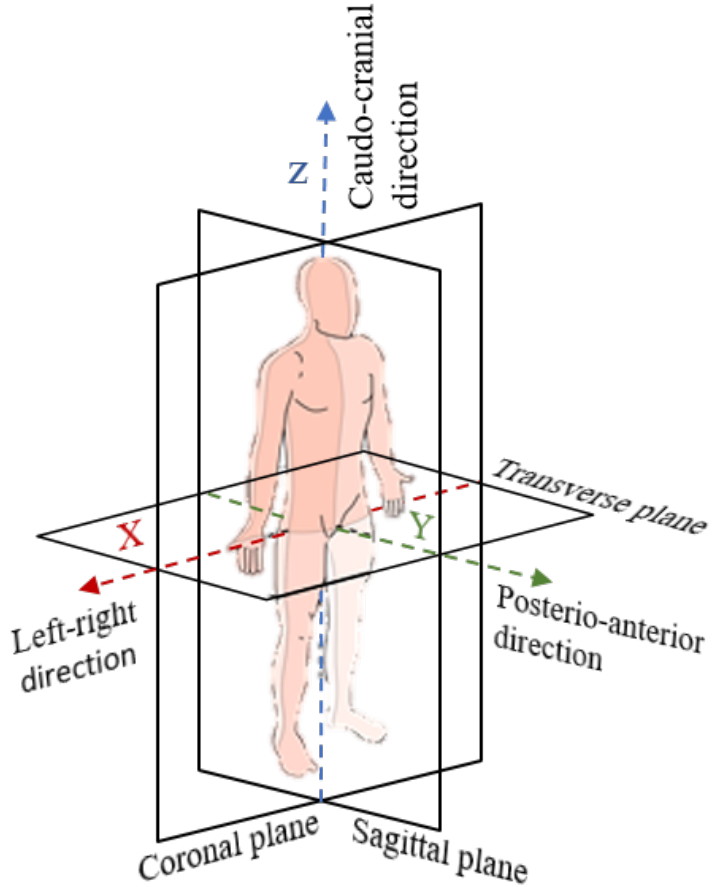


Figure 3.4: Anatomical planes and nominal Cartesian axis directions.

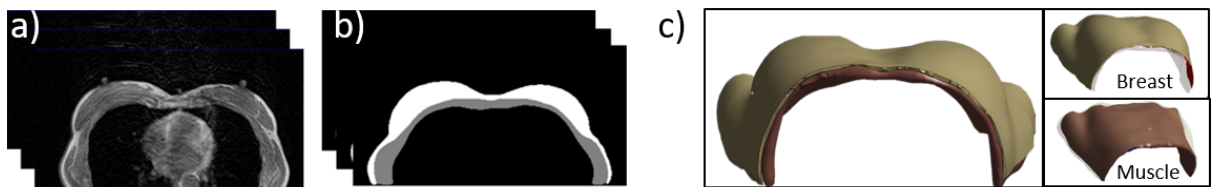


Figure 3.5: 3D geometries generation. a) MR images; b) segmented image; c) corresponding 3D geometries

3.2 Finite Elements Mesh

After computing the NURBS surfaces, the internal spatial information needs to be encoded using a volumetric mesh. The optimal elements type or mesh density in the simulation of FE models is still an open question and topic of debate. The use of hexahedral ele-

1410 ments is usually assumed to result in a more accurate solution, especially when expecting high strain/stress gradients. However, in the literature, because of the large computational time, such meshes are used mostly with a reduced number of elements (Ruiter et al., 2006; Gamage et al., 2012). Tetrahedral elements are widely used due to their geometrical flexibility and because they provide a good trade-off between computation time and
1415 displacement accuracy (Han et al., 2014; Palomar et al., 2008; Griesenauer et al., 2017).

In our case, an iterative optimization process is being considered to estimate the constitutive parameters. Therefore, to reduce the computation time, only linear tetrahedral elements are used. The first order elements are known to bear volumetric locking problems when used to model large strain for quasi-incompressible materials, (Fung et al.,
1420 2017). When volumetric locking occurs, the displacements calculated by the finite element method are orders of magnitude smaller than they should be. It has been shown that a linear element with a mixed U-P formulation can avoid these problems (Rohan et al., 2014). Therefore, in our work, the geometries are meshed using the solid element solid285 (ANSYS Mechanical) which provides a mixed U-P formulation option.

1425 On the other hand, the mesh density has also an impact on model accuracy, a finer mesh resulting in a more accurate and stable solution, but also increasing the computational time. To our knowledge, no studies have determined the optimal resolution of the volumetric mesh for simulating breast tissues deformations. To determinate the appropriate mesh size, a mesh convergence study was performed. The details can be found in Appendix B.
1430 According to these results the optimal elements sizes range between 7 and 10mm. The mesh that was chosen for the second volunteer thus consists in 18453 tetrahedral elements with 9625 elements assigned to the pectoral muscle and the thoracic cage and 8828 elements assigned to breast tissues (Figure 3.6).

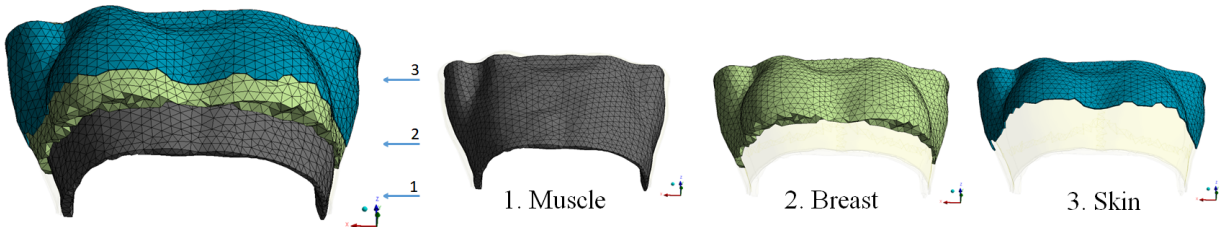


Figure 3.6: Finite element mesh components. The tissues components are cropped for visualization purposes.

The mesh quality is measured using three criteria: element skewness, aspect ratio
1435 and maximal corner angle. The Figure 3.7 shows the ranges of values for these shape parameters. The element's aspect ratio and maximal corner angle range between the nominal limits defining a good mesh quality (Section 2.2). There is a small number of elements with a skewness larger than the maximal theoretical quality limit (0.75) , however there are no degenerated elements (skewness = 1).

1440 The breast skin layer is added a posteriori as a 2mm thick single layer of shell elements (1980 elements). Shell elements and the underlying solid elements are sharing the same

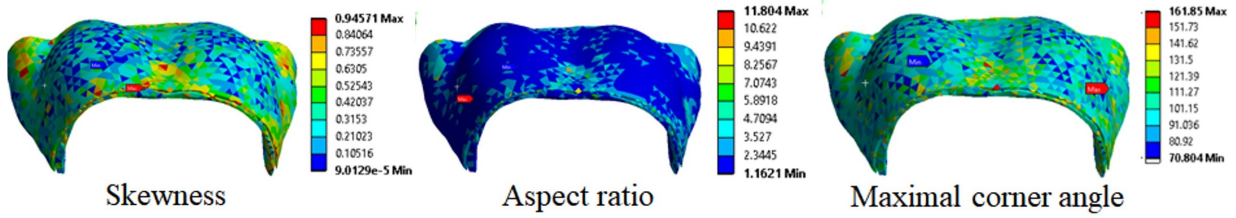


Figure 3.7: Finite elements mesh quality.

nodes (Figure 3.7.a).

3.3 Breast reference configuration

To estimate the reference configuration of the breast (*stress-free* configuration), an adapted prediction-correction iterative approach was implemented (Eiben et al., 2014) using prone and supine image data sets. The overall iterative process is presented in Figure 3.8. The first estimate of stress-free breast configuration is computed by applying an inverse gravity on the supine geometry. Then, at each iteration, the estimated stress-free configuration is used to simulate breast deformation due to gravity in a prone position. The differences between result of this simulation and the real shape of the breast in prone position is quantified by computing the Euclidian distances D_i between the *active nodes* defined at the breast external surface. These distances are then used in the next iteration of the process to simulate imposed displacements (Dirichlet condition) to the active nodes i in the stress-free configuration. To limit any mesh distortion, the displacements are only partially imposed using a multiplicative regularization factor ($\alpha < 1$). The process repeats as long as the new transformation improves the similarity between the two geometries in prone configuration by more than 1mm on average. The similarity between the estimated and measured configurations is given by the mean Euclidean distance over the active nodes.

During fitting process, the active nodes are chosen to be the ones corresponding only to the breast surface. The skin nodes bellowing to the arms and the lateral thoracic areas are excluded in order to neglect as much as possible the error due to rigid body changes.

To compute the position difference D_i of the nodes i between the estimated and the measured breast configurations, the positions of the active surface nodes on prone configuration have to be known. Thus, an additional mesh registration step is performed at each iteration: the active nodes are morphed into prone configuration using the elastic deformation method proposed by Bucki et al. (2010). The method estimates a C1-diffeomorphic, non-folding and one-to-one transformation to register a source point cloud onto a target data set D, which can either be a point cloud or a surface mesh. The input source points set is initially embedded in a deformable virtual hexahedral elastic grid. Then an iterative registration technique is performed by successive elementary grid deformations and at different grid refinement levels.

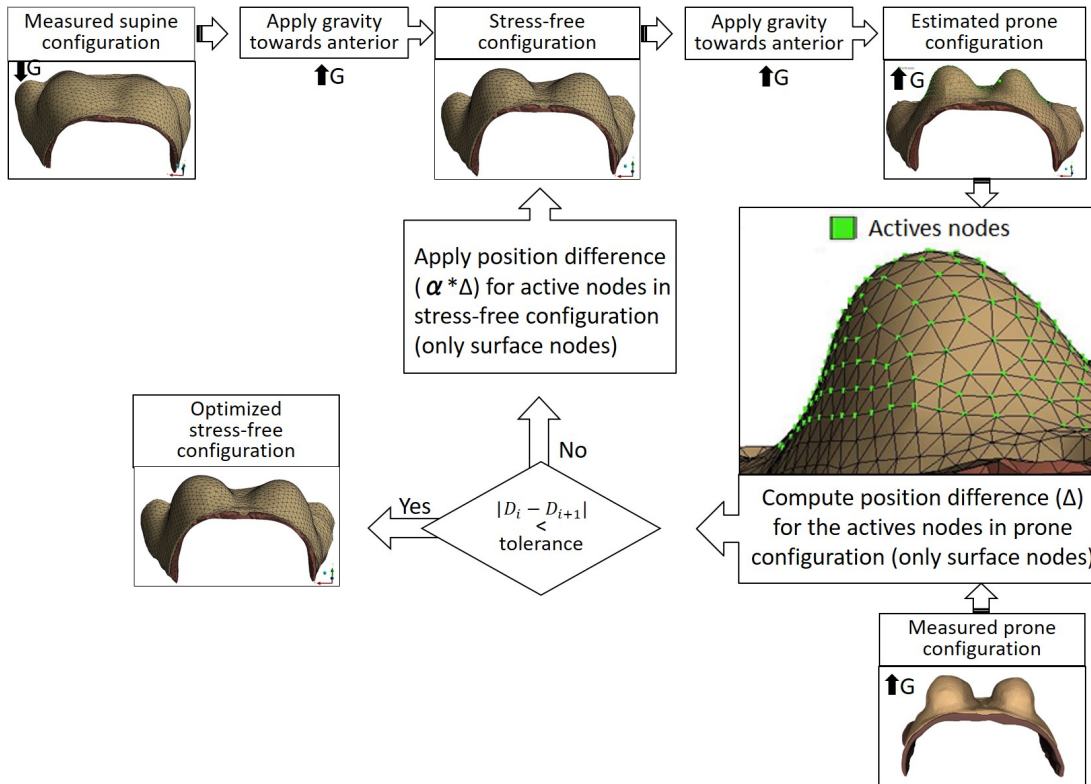


Figure 3.8: Fixed point type iterative algorithm for stress-free geometry approximation. D_i - mean node to node distance over the active nodes at iteration i , G - gravity force

3.4 Boundary conditions

Breast deformations can be modeled by solving the motion equations using two different types of boundary conditions, regarding either displacements (Dirichlet conditions) or forces (Neumann conditions).

First, to provide a rigid support for the muscle mesh component, zero displacement conditions are imposed to its posterior face, assumed to be attached to the rib cage (figure 3.9). Next, the interface between the breast mesh and muscle mesh is models using contact mechanics. The muscle is stiffer than the adipose tissues, thus its anterior face represents the target surface and the posterior breast face represents the contact surface (see Section 2.3 for a reminder of these target and source surfaces).

Previous works have shown that modeling breast deformations from prone to supine configurations requires to take into account breast tissues sliding over the chest wall (Carter et al., 2012; Han et al., 2014). Moreover, anatomical books (Mugea and Shiffman, 2014; Clemente, 2011) describe that the breast soft tissues are firmly attached to the deep fascia via suspensory ligaments but can move freely over the pectoralis muscle. Therefore, the juncture surface is modeled as a no-separation contact with a frictional behavior proposed by the ANSYS Contact Technologies (see Section 2.3.2). The penalty algorithm is used

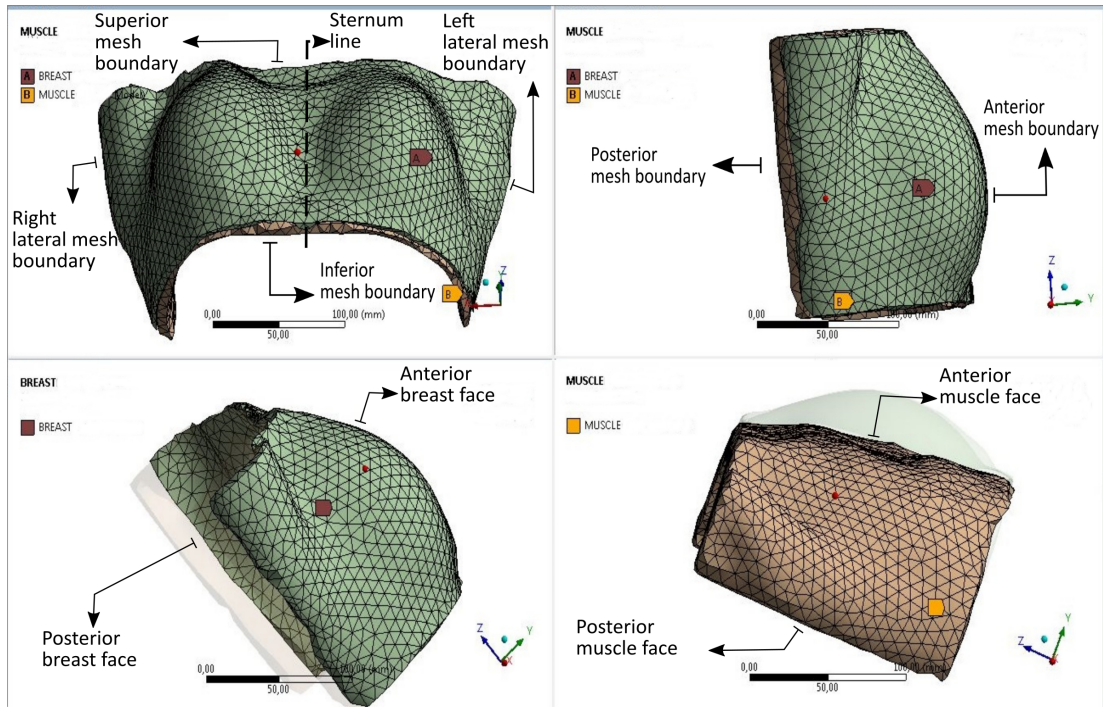


Figure 3.9: Finite elements mesh boundaries

with a meticulous control of contact normal and opening stiffness parameters. Stiffness parameters don't have a physical meaning and have to be identified by *trial and error* methods. Since these parameters are extremely sensitive to the underlying elements stiffness and to the local deformation direction, new values have to be identified for each new simulation case.

To study the impact of the friction coefficient μ_f on tissues sliding, several simulations have been performed at different values of μ_f . We found that, with the Coulomb friction law, even for a high value of μ_f , the tissues sliding is overestimated when estimating the prone breast configuration. When simulating prone breast configuration from the supine one, the sliding overestimation results also in an unconvex solution due to element distortion. At the contact surface, because of excessive sliding, the tissue accumulation in the region of the sternum line results in a sinuous surface (Figure 3.10) ; the finite element mesh undergo important distortions and the solution is compromised. Therefore, different strategies based on anatomical breast structures were investigated to limit the amount of sliding and to overcome solution instabilities (Annex 2). However, it seems that a small amount of friction improves the solution convergence capabilities (see ANSYS (2017a)); therefore the friction coefficient is kept to $\mu_f = 0.1$.

The strategy chosen to control the amount of tissues sliding relies on ligamentous breast structures described on Section 1.1.3. As concerns breast support matrix, only the largest structures are modeled, i.e. fascias and suspensory ligaments. The superficial layer of superficial fascia is integrated in the skin layer, assuming a higher material stiffness. In

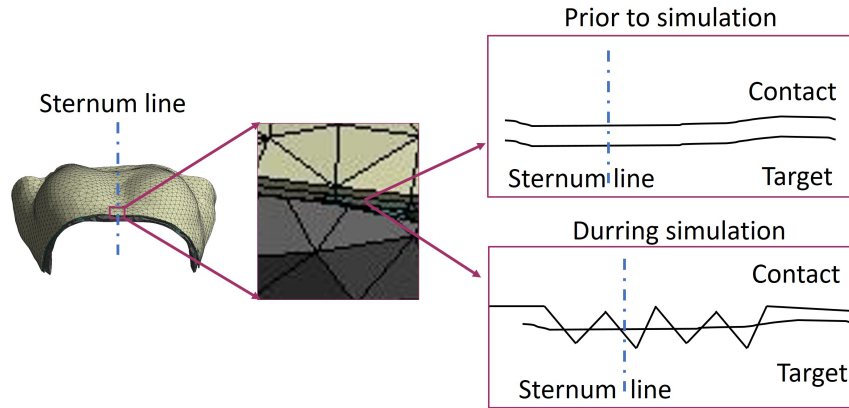


Figure 3.10: Tissues accumulation on the sternum line with excessive sliding

addition, a new layer of 0.1mm thick shell elements is added at the juncture surface between muscle and breast tissue to model the deep layer of the superficial fascia. Shell elements and the underlying breast elements are sharing the same nodes. Since the deep fascia and muscle tissues are supposed to present similar elastic properties, the deep fascia is not explicitly modeled. In addition, two ligamentous structures (inframammary ligament and deep medial ligament) are modeled using Ansys link type elements connecting breast posterior surface nodes to anterior muscle surface nodes (Figure 3.11).

Several additional Dirichlet conditions are set on the mesh boundaries: the superior and inferior ends of the deep fascia layer are constrained in Z direction; the superior and inferior ends of the skin layer are constrained in Y direction. For left and right lateral breast boundaries (Figure 3.9), Dirichlet conditions are too strong and preclude breast tissue to slide laterally. Therefore, in these regions new ligamentous structures are included with a cable-like behavior (Figure 3.11).

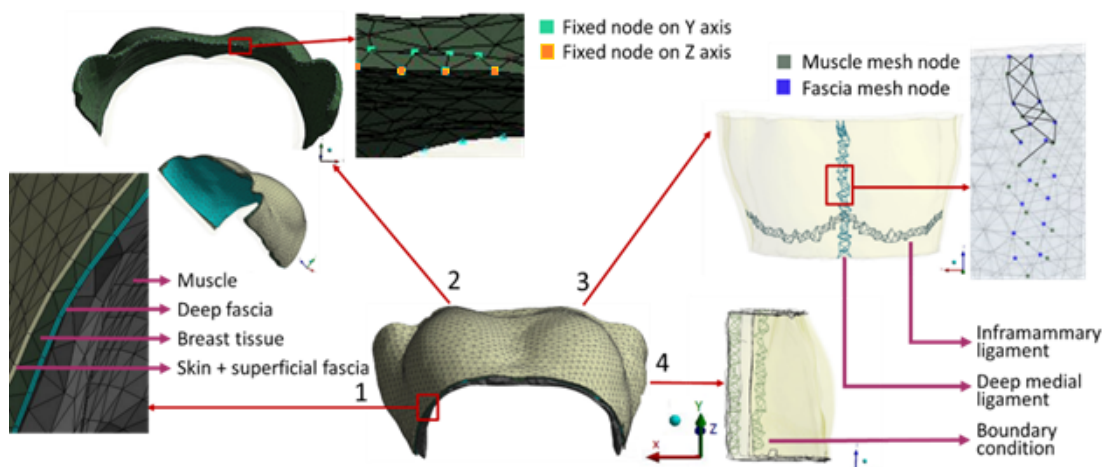


Figure 3.11: Components of the finite element mesh.

The deep layer of superficial fascia is much stiffer than the underlying adipose tissues. Due to imposed boundary conditions, the amount of sliding depends on fascia's elasticity.
1525 The suspensory ligaments define regions where the breast sliding is minimal regardless of the applied deformations. These additional stiff structures reduce the tissues sliding and improve the solution convergence capability.

3.5 Materials constitutive models

The final model consists of 6 types of tissues, wherein 4 tissues (glandular, fatty, muscle and skin) are well described and regularly used for biomechanical modeling and 2 of them (fascia and suspension ligaments) are with limited use and poorly described in the literature. A large range of constitutive parameters are available for each tissue. However because of an inconsistent interindividual variability, patient-specific parameters have to be identified.
1530

Here, all materials except the suspensory ligaments are modeled using the Neo-Hookean strain energy. Breast suspensory ligaments are assumed to undergo only small deformations, thus they are considered as linear materials. Patient-specific mechanical tissue properties are computed using an optimization process based on a multi-gravity loading simulation procedure (Figure 3.12). First, for a given set of parameters ($\lambda_{glandular}$, $\lambda_{adipose}$, λ_{muscle} , λ_{skin} , λ_{fascia} , λ_{ligam} , ν) the stress-free configuration is estimated by minimizing the difference between the simulated and the measured breast geometry in prone configuration. Then, from the new estimated stress-free geometry, the supine breast configuration is derived. The estimated supine geometry is compared to the measured one using modified Hausdorff distance, thus representing the estimation error. To avoid taking into account the geometry dissimilarity due to arms position, the modified Hausdorff distance is computed
1540 only on breast skin surface. The process implies multiple simulation based on imposed nodes displacement; therefore the FE mesh can be significantly altered (with convergence issues) before reaching an optimal stress-free geometry. Mainly for that reason, we chose to perform an exhaustive manual rather than an automatic research of the optimal set of constitutive parameters.
1545

An optimization process including finite element simulations with 6 parameters results is a complex and time-consuming problem. The model simplification is then performed in two steps. First, the parameters which variations have non-significant effects on simulation results are identified and set to an optimal fixed value. Next, for parameters which variations have a high impact, a sensitivity study is performed to redefine the search intervals
1550 and interval's discretization step.
1555

3.5.1 Model simplification

The breast tissues are mainly composed of water; a usual assumption is to consider them as nearly incompressible materials (Fung, 2013). However, previous works proposed a Poisson's ratio value ranging between $\nu = 0.3$ (Hopp et al., 2013) and $\nu = 0.5$ (Gamage et al., 2012). In a multi-loading gravity simulation, the breast volume is nearly constant,
1560

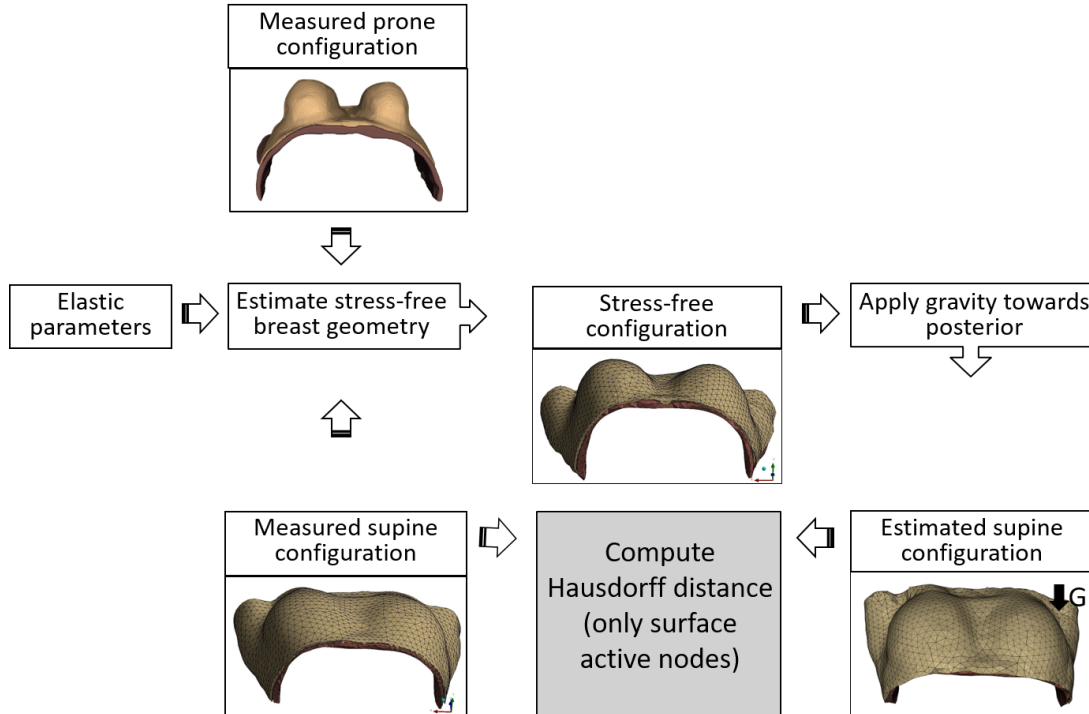


Figure 3.12: Process to estimate optimal material parameters

thus, the influence of Poisson's ratio on nodes displacements is studied only for values laying between $\nu = [0.45, 0.495]$ (Figure 3.13).

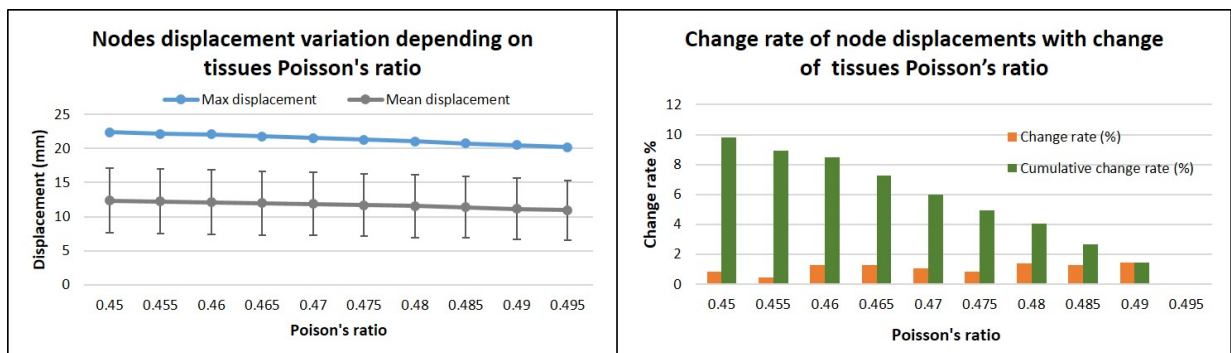


Figure 3.13: Process to estimate optimal material parameters

The simulations were performed by applying the gravity force in postero-anterior direction on breast geometry from supine configuration. On the right-hand side (Figure 3.13), the mean and the maximal displacements of the skin nodes are given for each values of ν . On the left-hand side of the figure, the maximal difference of nodal displacements between two consecutive simulations (change rate) and the maximal difference of node displacements between the actual and the less deformed geometry (cumulative change rate) are

plotted. The change rate is computed within the assumption that the maximal displacement over the simulations set represents 100% change rate. Non-significant variations are observed on the mean and maximal displacements of skin nodes, thus a constant value of $\nu = 0.49$ was chosen.

The pectoral muscle together with the thoracic cage are the breast tissues support. The deformation of the muscle under gravity loading is neglected. Therefore, its Young's modulus was not included on the parametric study and was chosen so that only minimal deformations occur ($\lambda_{muscle} = 10kPa$).

The ligamentous breast structures are added with a cable-like behavior to reduce tissues sliding. Their Young's modulus is also not included in the optimization process and is set sufficiently high ($\lambda_{ligam} = 500kPa$) to preclude their elastic deformation.

The adipose and glandular tissues are known to be extremely soft and to undergo large deformations under gravity loading. Calvo-Gallego et al. (2015) proposed a uniform polynomial material model for the mixture of adipose and glandular tissues. The authors have also shown that the breast outer shape deformation does not depend on glandular distribution but is highly dependent on its volumetric ratio. It was also chosen here to model the glandular and fatty tissues as a single homogeneous material with an equivalent Young's modulus λ_{breast} . The mechanical properties of the equivalent breast tissue are in direct relation with glandular and adipose volumes ratios. Because the left and right breasts may have different granularities, two different parameters are considered (λ_{breast}^l , λ_{breast}^r).

Breast skin and superficial fascia are an essential part of the breast support matrix. The two layers are much stiffer than breast tissues and are the structures governing the amount of deformations. Their elastic behavior was included on the optimization process.

Based on existing publications, an interval of possible values are given in Table 3.2 for each parameter included in the optimization process (λ_{breast}^l , λ_{breast}^r , λ_{skin} , λ_{fascia}). To characterize model sensitivity to parameters variations, a set of simulations were performed. The defined interval was discretized by steps of 10% and at each step the skin nodes displacement were computed. Results of the corresponding simulations are shown on Figure 3.14. As previously, the first column represents the variation of mean and maximal displacements of skin nodes in function of the elastic parameter of each material; the second column represents the change rate and the cumulative change rate of skin nodes displacements.

	Search intervals from bibliographic data			Search intervals after model simplification		
	Breast	Skin	Fascia	Breast	Skin	Fascia
Min (kPa)	0.3	7.4	100	0.3	2	50
Max (kPa)	6	58.4	5000	4	20	250

Table 3.2: Minimal and maximal value (in kPa) for Young's moduli.

The figure shows that the model is very sensitive to the variation of Youngs modulus

of breast tissue, skin and fascia (Figure 3.14). However, beyond some values, the materials become too stiff and do not change significantly the breast deformations under gravity loadings. Therefore, the search intervals for breast tissue and skin Young's moduli are reduced so that a larger value impacts the cumulative change rate less than 20% (max displacement less than $\sim 5mm$). As the fascia stiffness governs the lateral displacement and shows a smaller variation over the search interval, a threshold of 10 % ($\sim 2.5mm$) is chosen. The obtained search intervals are summarized in Table 3.2

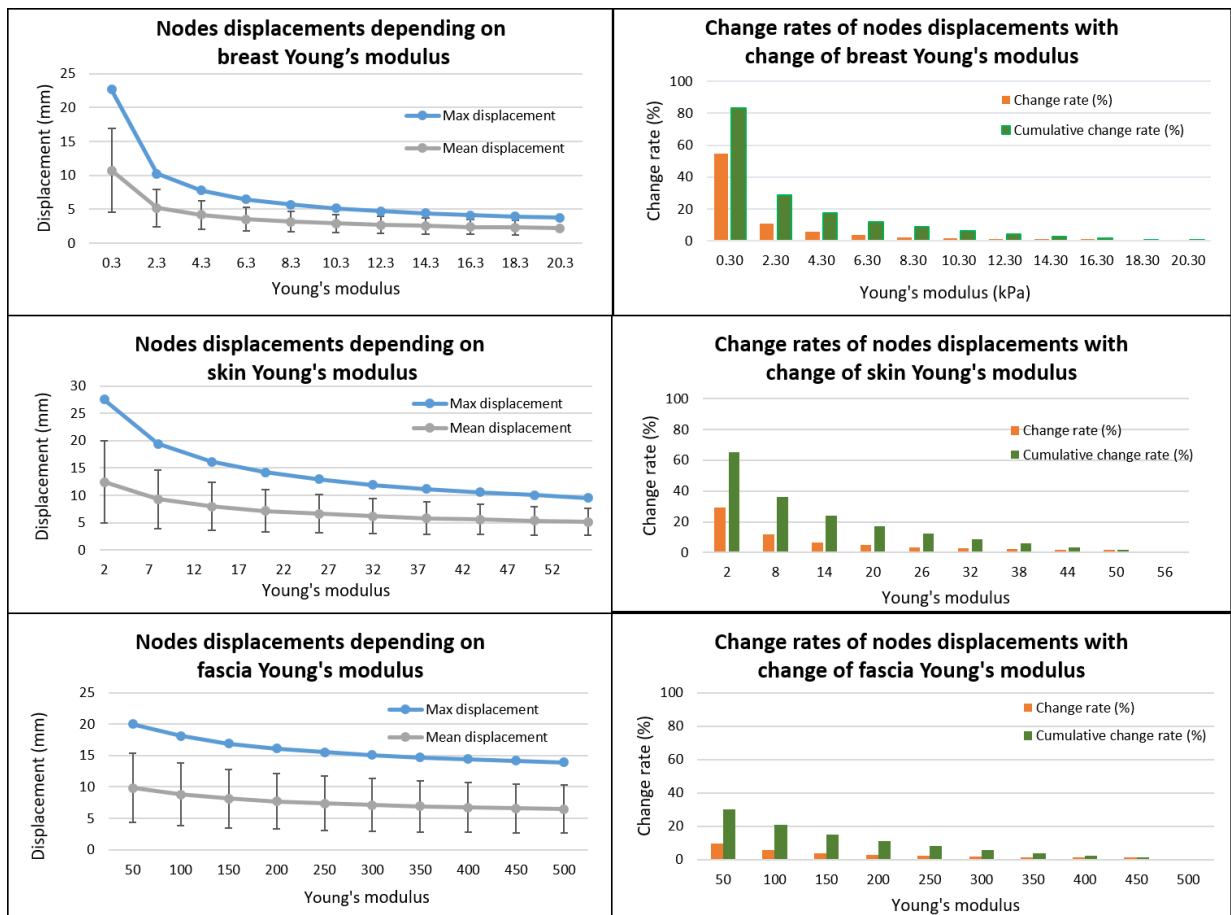


Figure 3.14: First column: relation between maximal and mean nodes displacement and the equivalent Young's moduli variation for different tissues. Second column: rate and cumulative change rate of node displacement in function of quivalent Young's modulus

3.5.2 Estimation of the optimal constitutive parameters

To perform the optimization process, the new intervals defined by the above sensitive analysis are discretized by steps of $0.1kPa$, $1kPa$ and $40kPa$ respectively for breast, skin and fascia tissues. The discretization step is chosen such that the change rate between two consecutive simulations is less than 10%.

1615

The previously described multi-loading gravity process was performed for each parameters set and the corresponding model error distribution is shown in Figure 3.16. The contour lines are estimated by linear interpolation between two consecutive simulations.

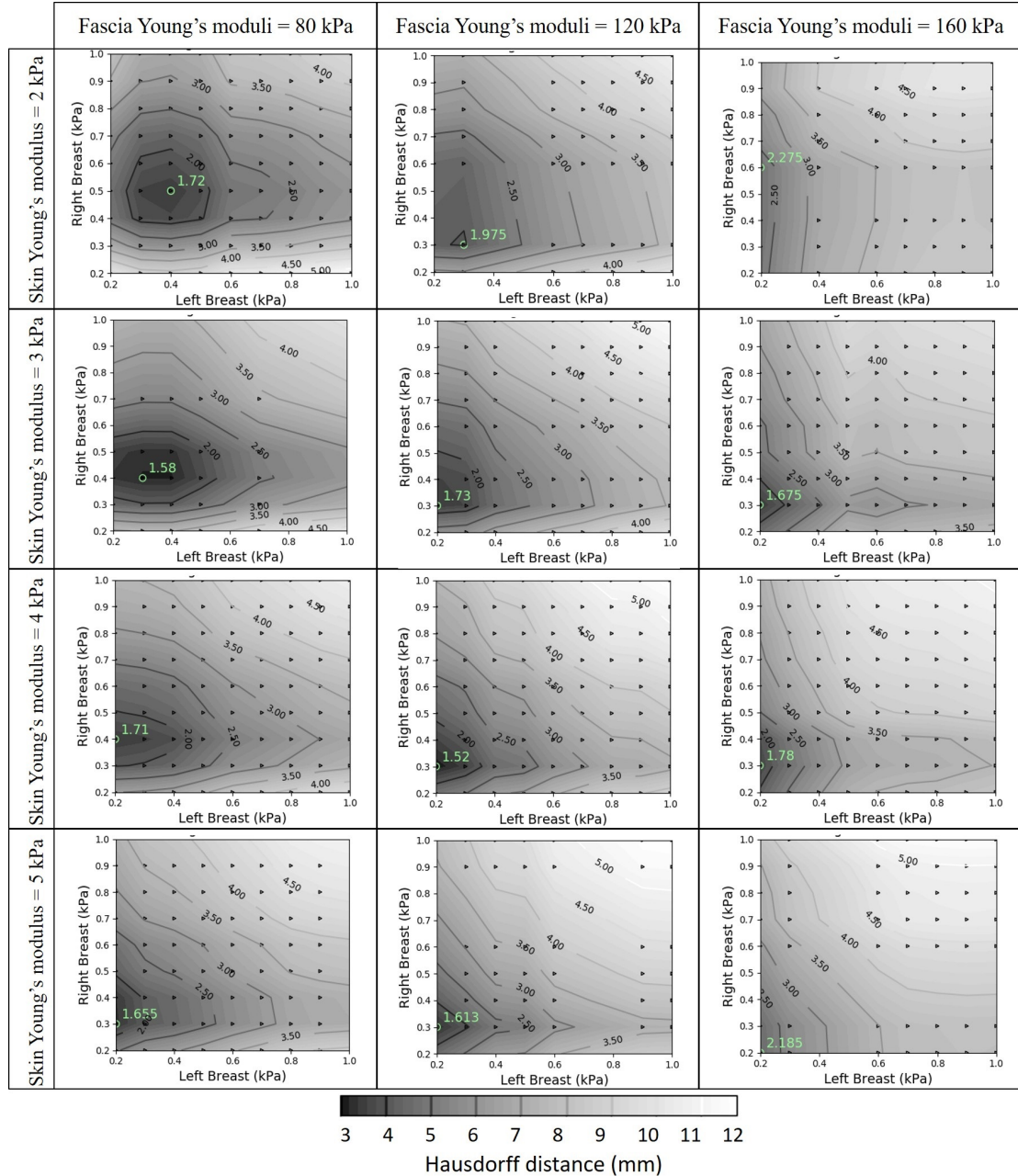


Figure 3.15: Hausdorff distance on the skin surface over the constitutive parameters space

1620

It was found that the breast tissues Young's modulus is lower than the ones proposed in the bibliography, therefore more simulations were done outside the defined intervals. However, for very low values, below 0.2 kPa, 2 kPa and 80 kPa for breast, skin and fascia's

Young's moduli respectively, the tissues deformation is too large and the finite element mesh becomes degenerated at the first step of the multi-loading simulation. For values above 1 kPa, 5 kPa and 160 kPa, tissues deformation is too small compared to the ones measured on the MR images and the simulations were excluded. All other missing values correspond to failed simulations due to a non-converging force, specifically in the region of the contact surface between the breast and the muscle.

For soft fascia ($\lambda_{fascia} = 80\text{kPa}$), the lateral displacement of breast tissues is more important than the one measured on MR images. Contrary, for stiff fascia material ($\lambda_{fascia} = 160\text{kPa}$) the amount of sliding is too small. To match the breast geometry in supine configuration, very low values for Young modulus are required ($\lambda_{breast} < 0.2\text{kPa}$). For such low values, the breast tissues are highly deformed, thus the elements undergo distortions. Because of such errors in elements formulation the simulations giving the minimal Hausdorff distance have not succeeded.

The set of parameters giving the best match between simulated and measured supine breast configurations is ($\lambda_{breast}^r = 0.3\text{kPa}$, $\lambda_{breast}^l = 0.2\text{kPa}$, $\lambda_{skin} = 4\text{kPa}$, $\lambda_{fascia} = 120\text{kPa}$).

Figure 3.16 shows the differences between the measured and estimated breast geometries in prone(left) and supine(right) configurations . Each distance was computed over the skin active nodes used also for the model optimization.

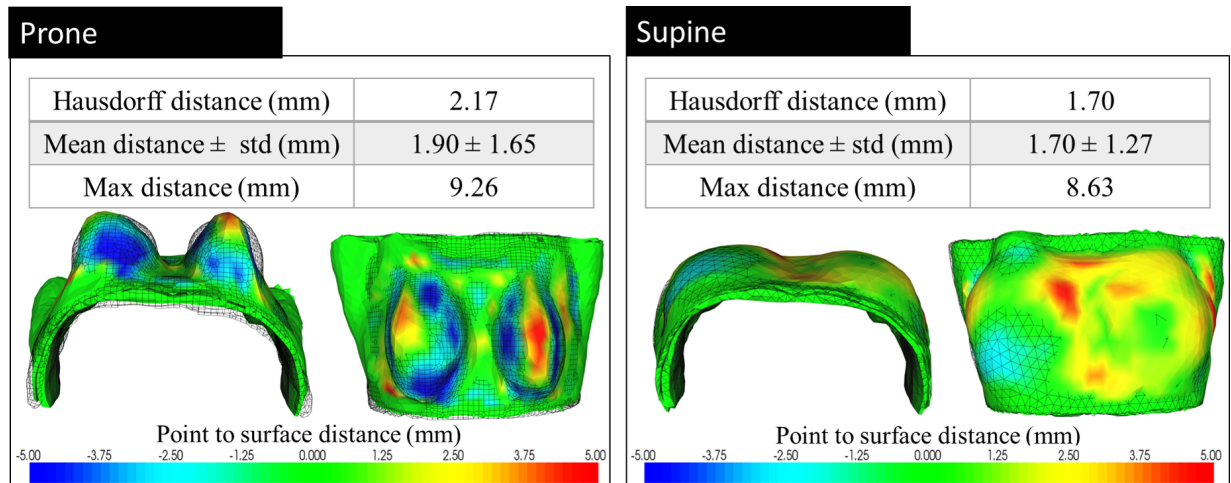


Figure 3.16: Difference between estimated and measured data, in prone and supine geometries, obtained with optimal Young's moduli and stress-free geometry.

The breast geometry is better estimated in supine configuration with an Hausdorff distance equal to 1.72 mm. This is probably due to a better representation of the boundary conditions in supine configuration, as this configuration was used to create the initial finite element mesh. The breast geometry in prone configuration is also well estimated with a modified Hausdorff distance equal to 2.17 mm. The maximal node to surface distance is obtained on the breast lateral parts. Considering a non uniform skin thickness or elastic

properties over the breast surface as described by Sutradhar and Miller (2013) should improve the obtained results in prone configuration.

3.6 Model validation

MRI-based biomechanical models already published in the literature have used the same 1650 breast configurations for the optimization and the evaluation process. In such cases, the model accuracy is assessed for a single deformation case, namely the one used during the optimization process. Therefore good estimation errors are expected. However, there is a high probability that the same model will fail in computing the global breast deformations within different conditions, for example different gravity orientation or breast compression.

The developed breast model is needed to model soft tissues deformation under compression, thus the model error have to be assessed in a more general framework. The supine tilted breast configuration was not used during the optimization process, therefore the difference between the estimated and measured data in this position was computed to evaluate the model capabilities. 1655

To compute the breast deformation under gravity loading on supine tilted configuration, the reference geometry together with previously defined materials models were used. The body force direction was defined conform to the vector obtained by image registration (section 3.1.3). The model accuracy in reference with the real deformations was assessed using 4 measures of distance based on the skin nodes spatial location (Appendix A). As 1660 previously only the active nodes subset was considered for distances computation. Figure 3.17 shows the respective node to surface distance magnitude, mean and maximal node to surface distance and modified Hausdorff distance. 1665

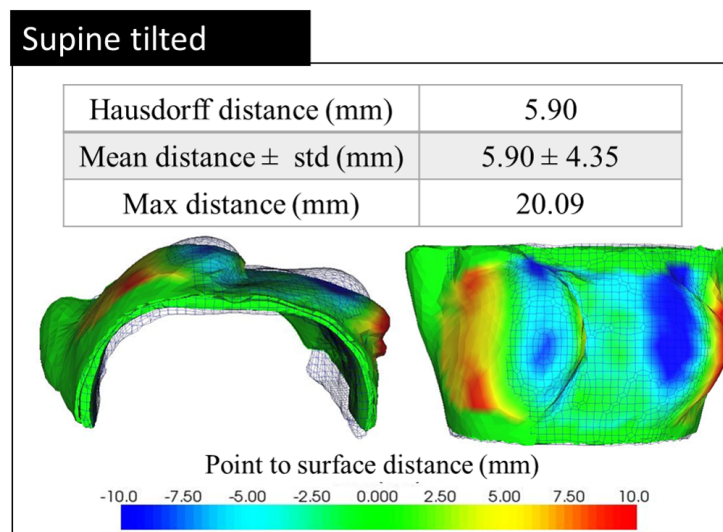


Figure 3.17: Difference between estimated and measured breast geometries in supine tilted configuration.

One may see that the supine tilted breast configuration is unwell described by the breast biomechanical model (Hausdorff distance equal to 5.90 mm). Large difference between simulated and measured breast surfaces is caused by the excessive sliding of breast tissues over the chest wall. Numerical or structural modeling choices could explain such a behavior.

Firstly, the fascial and ligamentous tissues are usually characterized by a cable-like behavior. The strain-energy density function must behave asymptotically in order to limit the fascia stretch and thus to reduce non-linearly the breast sliding over the chest wall. Limitations of the neo-Hookean model to capture the mechanical response of some non-linear materials is well known (Kaliske and Rothert, 1997). For large strain rates, the Neo-Hookean material may undergo a relaxation and therefore becomes easier to deform. Our numerical results have shown that the maximal strain at the fascia level is significantly higher in supine tilted position (about 140%) than in supine or prone positions (about 50%). Therefore, an asymptotic behavior of fascia mechanical response must be considered. The Gent form of the strain-energy function characterizes better such mechanical response (Gent, 1996) and will be considered as an alternative choice .

Secondly, the breast support matrix is composed of 4 suspensory ligaments, however only three of them were partially modeled: inframammary, deep medial and deep lateral ligaments. The 3D structures connecting the skin to some muscular areas, namely the cranial ligament, were neglected. The particularity of the cranial ligament consists in its position. Indeed, almost its entire structure underlies the skin and the only attachments to the thorax are situated at the clavicle and seventh rib levels (inframammary ligament). Including such structures at the skin surface may result in local high strain gradient rates causing solution instability and anesthetic surface deformations.

3.7 Discussions and conclusion

In this chapter, a new finite element breast model was proposed and evaluated with real tissues deformations measured on MR images. To this end, MR images of two volunteers were acquired in three different configurations: supine, prone and supine tilted. The supine and prone MRI volumes were used to adapt the biomechanical model to the volunteer individual breast geometry and its respective tissues mechanical properties. The optimal mechanical properties were found by exhaustive search over a predefined parameters domain. For each combination of tissues elastic properties, the breast reference configuration was computed using an adapted prediction-correction iterative scheme. The parameters set giving the best fit between estimated and measured breast configurations was selected. Using these optimal estimates, the supine, prone and supine tilted breast configurations were computed and compared to the MRI volumes.

It was found that, extremely soft materials laws (0.2-0.3kPa for breast tissues and 4kPa for skin) have to be used in order to obtain the same tissues displacements rate as measured on MR images. Moreover, the breast tissues sliding have to be considered when computing such large deformations. However, because of tissues hyper-elasticity, the model boundary conditions have to be revisited in order to ensure the convergence capability of the solution.

With such soft tissues, the finite element mesh may become highly distorted. Therefore to limit elements distortion a stiffer layer was added between the breast tissues and muscle
₁₇₁₀ representing the deep layer of the superficial fascia. The excessive sliding was prevented by using ligamentous structures fixing the soft tissues on the pectoral muscle.

Contrary to the previous works, our model is evaluated in 3 breast configurations. Among the 3 geometries, two of them were used for the model optimization and evaluation, and the last one (supine tilted geometry) was used for the evaluation only. Good
₁₇₁₅ estimates were obtained in prone and supine configurations with a Hausdorff distance equal to 2.17mm and 1.72mm respectively. The estimate of the supine tilted breast geometry pointed out the limitations of the Neo-Hookean model to assess rich mechanical behavior of breast soft tissues for large strains. These limitations were not identified in the previous works.

₁₇₂₀ The model optimization if a tough and time consuming process. It was extremely difficult to obtain the solutions convergence when combining the tissues large deformations with the sliding contact conditions. Because of the large computation time, the reference breast configuration and the optimal constitutive parameters were computed only for the first volunteer. The model optimization of the second volunteer is considered for future
₁₇₂₅ work.

Assuming that our model describes well the breast mechanical behavior, it can be used to compute breast tissues deformation under compression. In that case, internal tissues strains and the pressure distribution over the skin surface will be used to quantify the patient comfort during a mammography exam.

4

1730

BREAST COMPRESSION *State of the art*

Mammography is the sole screening method recognized by the European Commission for women aged 50-69 years. Its morphological method enables examination of the breast in its entirety and offers a high sensitivity for early-stage tumors. However, the mammographic exam is known to be awkward and unpleasant for the patient, the main source of discomfort lying in its operating principle. The perceived pain is related to the breast compression between the image receiver and the compression paddle.

For such a standard and wide-used procedure good conditions and patient comfort should be ensured. Therefore, a study on the relevance of breast compression methodology in mammography is of a potential interest. The next chapter describes a standard mammographic procedure including the breast positioning methods and the most used paddles designs. The need of compression is explained in terms of image quality, average glandular dose and patient comfort and the respective today's gold standards are introduced. Finally, the interest of developing a simulation environment to assess the breast compression quality is explained.

4.1 Mammographic positioning

During mammography, a qualified radiologic technologist positions the breast of the patient between the stationary bucky (X-ray detector housing) and a movable paddle. A routine mammographic exam consists of two views: cranio-caudal (CC) and mediolateral oblique (MLO) projections.

In a regular workflow, the breast compression is performed in the up-right body position. In the CC view (Figure 4.1 left) the breast is placed on the bucky, which is initially positioned at the inframammary folder level or a few cm higher depending on breast mobility in the corresponding direction. Then the technologist lowers the compression paddle using a foot switch and gently pull the breast onto the bucky to correctly position the breast and to maximize the amount of projected tissues. In the MLO view (Figure 4.1 right), the bucky is rotated to an angle between 40 to 55 deg. The woman rests the lateral oblique site of her breast against the bucky. In this view the pectoral muscle is located between the detector and the compression paddle; as the muscle is stiffer than the breast tissues, the woman have to stay relaxed in order to have better breast flattening. When lowering the compression paddle, the technologist has to pull the breast up and forward to prevent drooping of the breast, and again smoothen out any skin folds.

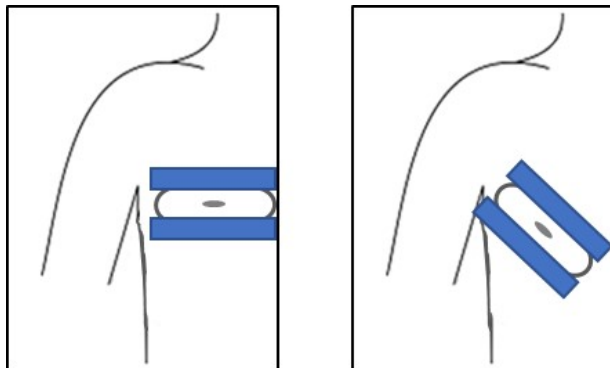


Figure 4.1: left: cranio-caudal breast compression; right - mediolateral oblique breast compression

The two views are complementary. The MLO view covers more tissue and provide better visualization of the upper juxtathoracic part of the breast, while CC-view suffers less from overlapping dense tissues and provide a better visualization on the central part of the breast (Chan et al., 1987; Kim et al., 2006). Further incidences or magnification views may be needed for diagnostic mammography (Groot et al., 2015).

The mammography devices are equipped with paddle position and force sensors to measure and display the compressed breast thickness and the amount of force applied to the breast.

4.2 Paddles designs

Nowadays, a wide range of compression paddles are available for breast clinical examination. Their shape and dimensions vary in function of the purpose for which it was designed but also on the manufacturer. According to their specific indications for use, three categories can be distinguished: **standard paddle** used for regular screening, **spot paddles** used mostly for diagnosis purposes and **biopsy paddles** used for breast compression during biopsy (Figure 4.2).

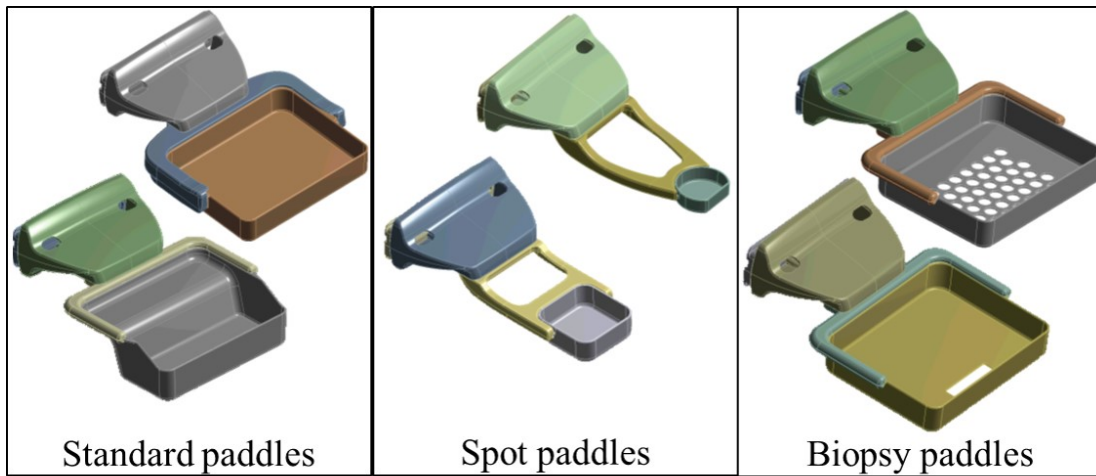


Figure 4.2: Different breast compression paddles for GE-Healthcare mammography unit .

The standard compression paddles have usually a rectangular shape with a flat compression plate. Depending on the industrial manufacturer, they can have different size of the lateral and longitudinal paddle edges and of the paddle front edge height. In their turn, the standard paddles are classified into rigid and flexible paddles. The standard rigid paddle (SRP) is fixed to its frame and is constrained to move in the up-down direction only. This paddle has some flexibility because of material mechanical properties and can slightly bend when compressing the breast, while remaining globally parallel to the image receptor. On the other hand, the standard flex paddle (SFP) is attached to its frame by flexible joints and therefore, presents an additional degree of freedom enabling the paddle to tilt with respect to the image receptor plane (Figure 3.c). During compression the paddle remains parallel to the detector at first, tilts towards nipple side and ends with the highest point at thorax level. Depending on the breast position, the paddle may also slightly tilt in the medio-lateral direction.

Spot paddles apply the compression to a smaller area of tissue using a small compression plate or cone. By applying compression to only a specific area of the breast, the effective pressure is increased on that spot. This results in better tissue separation and allows better visualization of the small area in question. It is used to distinguish between the presence of a true lesion and an overlap of tissues, as well to better show the borders of an abnormality or questionable area or a little cluster of faint microcalcifications in a dense breast.

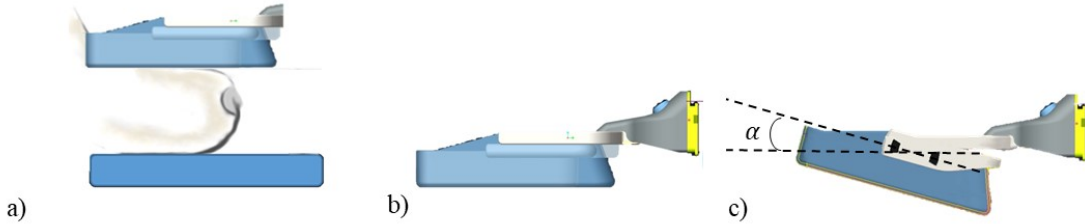


Figure 4.3: Breast compression between the paddle (up) and the receiver (down): a) Rigid paddle; b) Flex paddle with flexion angle α

Biopsy exam requires that the patient's breast remain immobile and in compression during the entire procedure. The biopsy paddles have the same shape as the standard rigid paddles. However, to allow the needle insertion and the accessibility to the biopsied area the paddle plate contains multiple holes with various diameter or a single aperture.

In this chapter, only breast compression with the rigid paddles in the two main view (MLO and CC) are considered.

4.3 Compression mechanics

Nowadays, the European Commission recommends a force standardized breast compression, i.e. the compression stops at a level of force just below the subjects pain threshold or to the maximum setting of the machine. The compression guidelines state that force should be firm but tolerable with a maximum applied compression of 130-200 N (Perry et al., 2008). As there is no exact specification for the application of breast compression, the applied force may vary between radiologists. Mercer et al. (2013) have analyzed the variation of the applied force within 14 trained practitioners. Both views, CC and MLO, were included. The authors found a significant difference between the average applied forces and have highlighted three groups of radiologists depending on the mean force intensity. Between the consecutive groups a mean difference of 1.6daN was found.

The global breast compression cycle is characterized by two phases: flattening and clapping (de Groot et al., 2015). During the flattening phase, the breast is gradually deformed by increasing the compression force, the deformation last about $7.5 \pm 2.6\text{ s}$. By contrast, during the clamping phase which last approximately $12.8 \pm 3.6\text{ s}$, the compression paddle is immobilized holding the breast in a stationary position.

Figure 4.4 shows a typical compression cycle for a CC breast compression described by de Groot et al. (2015). One can see that, during the compression phase the breast thickness and contact area evolve non-linearly; meanwhile, the compression force and pressure increase quasi-linearly. During the clamping phase, the breast thickness and compression force remain constant; however, the skin pressure slightly decreases in the first 10s. This phenomenon may be explained by breast volume changes because of the viscous effusion of blood and lymph into the central systems.

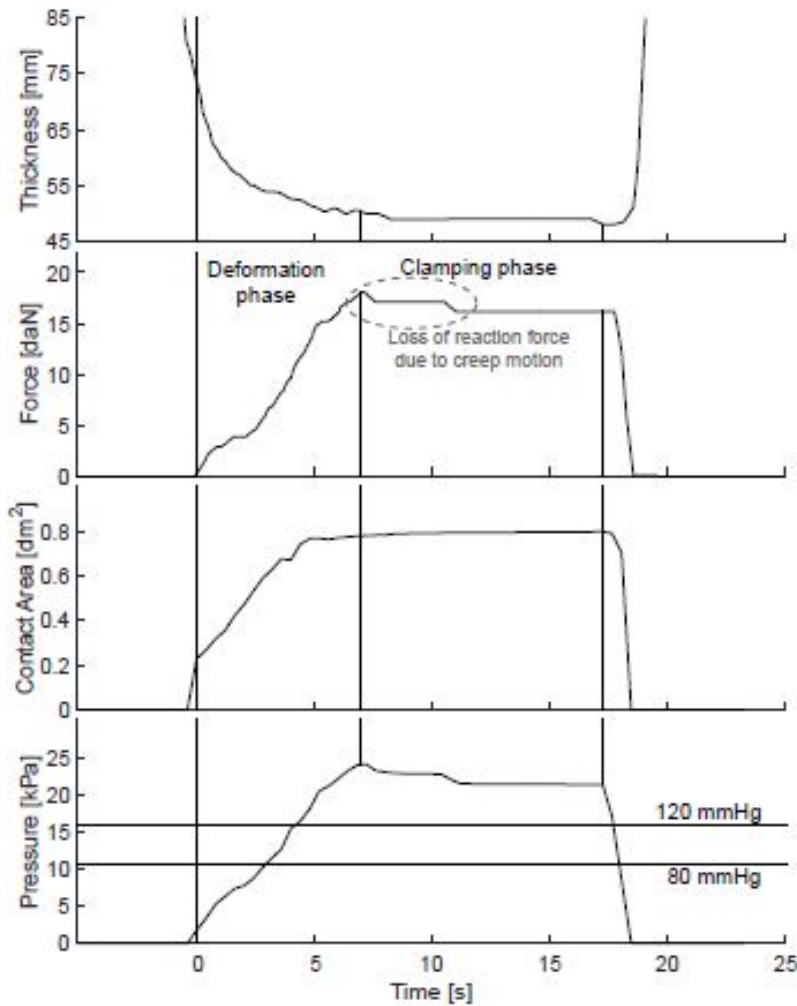


Figure 4.4: A typeical breast compression cycle. Reproduced from Groot et al. (2015)

In the same work, the author presents several characteristic patterns describing the relation between breast thickness and compression force depending on breast size and its firmness (Figure 4.5). One can see that, for a larger breast, higher compression force is needed but the overall behavior remains the same as for smaller breasts. For similar breast sizes, the final compression force range within the same values, however a firmer breast will reach faster the limiting value of breast thickness resulting in a asymptotic increase of the compression force.

Dustler et al. (2012a) have studied the areal pressure distribution patterns for MLO breast compression (55 deg tilt). The authors showed that the pressure distribution varies widely within the breasts. The obtained patterns from 131 subjects were classified into four main groups: a) skin pressure widespread over the breast (29%); b) skin pressure concentrated on the central part of the breast (8%); c) skin pressure concentrated on the juxtathoracic region (16%); d) skin pressure concentrated along a narrow zone at the

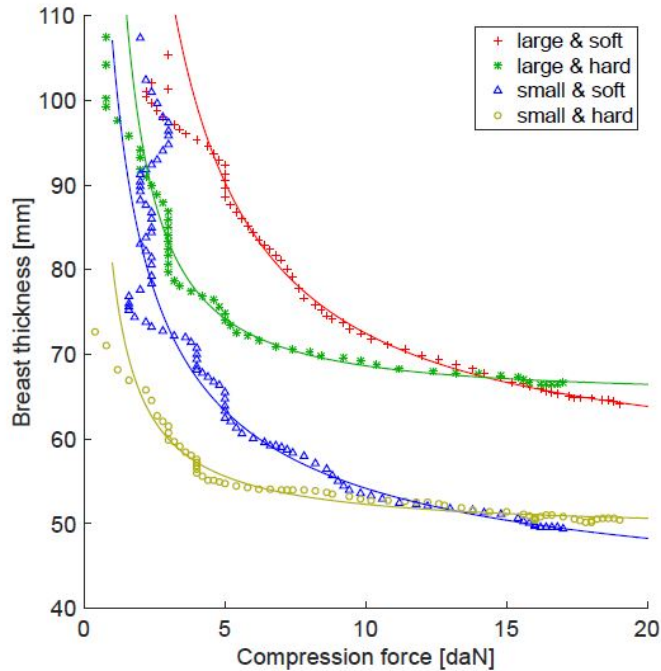


Figure 4.5: Characteristic breast flattening curve as function of the applied force. Reproduced from Groot et al. (2015)

juxtathoracic region (26%). According to their results, the pressure distribution depends on two factors: the variation on breast thickness and surrounding tissues stiffness. For example, for the groups C and D the breast anterior tissues compression is limited by the pectoral muscle which is much stiffer than the breast tissues. These results may explain the fact that, in MLO view, the breast thickness exceed the one on the CC view, despite the greater force used for MLO than the CC breast compression (Mercer et al., 2013; Helvie et al., 1994).

4.4 Compression quality metrics

A standard mammographic protocol always includes breast compression prior to image acquisition. The breast flattening improves diagnostic image quality and reduces the absorbed dose of ionizing photons. However, the discomfort and pain produced by this procedure sometimes might deter women from attending breast screening by mammography.

An important improvement concerning the patient comfort could be achieved with the emergence of digital mammography. Several studies have shown that digital mammography is better in terms of image quality (Obenauer et al., 2002) and radiation dose (Chen et al., 2012) than film-screen mammography.

Most digital mammography systems have an automatic beam quality selection mode

(automatic optimization of parameters, AOP) with an automatic exposure control (AEC). The AOP mode automatically selects the x-ray tube voltage, anode target material and filter material, in order to optimize the *contrast to dose ratio*, i.e. the appropriate amount of radiation for an acceptable low dose and an increased contrast, according to breast thickness and composition (Williams et al., 2008). Then, the required exposure time for the actual image is calculated by the AEC. The AOP control allow to compute for each patient and compression level, the X-ray spectrum that optimizes the ratio of benefits (higher image contrast) and drawbacks (higher dose). In this section, the compression quality will be measured in terms of three metrics: image quality, average dose and patient comfort. A detailed description of each metric is given below with their impact for digital mammography.

4.4.1 Image quality

Many factors may influence the quality of the mammographic image such as the knowledge and skill of the person who performed the mammographic examination, equipment, positioning technique, compressed breast thickness, type of breast cancer, and radiographic appearance of the breast tissue (de Groot et al., 2015; Andolina and Lillé, 2011). In our study, only the impact of the compressed breast thickness on image quality is analyzed.

Firstly, the breast compression facilitates the image interpretation. Higher compression leads to more spread tissues and consequently to less overlapping of clinical important structures. A thinner layer of breast tissues allows a more subtle differentiation between normal and suspension findings. Secondly, breast compression affects the image sharpness. Since the exposure time last several seconds, a proper breast immobilization leads to a less blurred images, preserving the conspicuity of abnormal lesions. Moreover, with a reduced breast thickness the primary contrast is raised due to the reduction of scatter and the improvement of the ratio of penetrating radiation to non-penetrating radiation reaching the image receptor. Finally, the breast compression leads to a better use of the detector dynamic range. With a non-uniform breast thickness, the different levels of brightness are used to describe the thickness variation, thus the detector dynamic is not used optimally for the contrast representation due to different internal structures.

It has been proved that the image quality decrease with the increasing breast thickness (Ko et al., 2013; Helvie et al., 1994; Saunders and Samei, 2008; Poulos et al., 2003). Helvie et al. (1994) analyzed the image quality for the observed breast thickness of 250 subjects using film-screen mammography. The difference in breast thickness and image quality between the MLO and CC paired images were computed. According to authors, the geometric sharpness decreased by 19% for 1cm of increased breast thickness. In addition, contrast loss was observed due to scatter augmentation and beam hardening.

Later, Saunders and Samei (2008) have studied the effect of breast compression on mass conspicuity in digital mammography using Monte Carlo based simulation framework. The simulation was done for two breast thicknesses (4cm and 6 cm) with two compression levels (standard and reduced compression 12%) and three photon flux conditions (constant flux, constant detector signal, and constant glandular dose). The results suggest that if a

particular imaging system can handle an approximately 10% increase in total tube output and 10% decrease in detector signal, breast compression can be reduced by about 12% in terms of breast thickness with little impact on image quality or dose.

1900 OLeary et al. (2011) performed a clinical study to assess the image quality in function of the applied compression force for digital mammography. The CC and MLO views of 4790 subjects were analyzed, image analysis was undertaken using perfect, good, moderate and inadequate categorization. The results have shown that the image quality is highly correlated with the applied force. The mean compression force required to produce a 1905 perfect image was found to be equal to 121.34 N for a CC view and 134.23 N for a MLO view.

4.4.2 Average glandular dose

The mammographic unit uses X-rays to obtain 2D-projection images from the tissues inside the breast. As for all X-ray exposures, the irradiation of a targeted population is accepted if the benefits are significantly higher than the risks. Therefore, the mammographic exposure have to provide a good image quality while preserving the radiation dose *as low as reasonably achievable*.

1910 To assess the quality of breast compression the risk from the X-ray exposure have to be considered. The absorbed energy from digital mammography depends on many factors 1915 such as the breast density, breast thickness, volumetric distribution of glandular tissues as well as the chosen acquisition parameters by the AOP mode.

1920 It has been proved that the glandular tissue of the breast is more vulnerable to radiation carcinogenesis than the skin, adipose tissue, or areola (Hammerstein et al., 1979). Based on these findings the average glandular dose (AGD) was defined to quantify the risk from 1925 breast irradiation and is widely accepted for regulations. The most often used methods calculate the AGD as the product of the incident air kerma at the upper surface of the breast and conversion factors called *normalized dose*. The normalized dose (DgN) is computed as a function of spectrum, breast thickness and breast density, its computation is based on Monte Carlo simulations (Dance et al., 2000; Boone, 1999).

1925 Historically, only standard rigid paddles were used for breast cancer screening. Wherefore, in numerical simulations, the breast is usually modeled as a flat semicircular phantom with a homogeneous content and surrounded by a layer of skin-representing tissue. The attenuation coefficient of the content corresponds to the breast density, the ratio of the amount of gland to total breast (Dance et al., 2000).

1930 Then a flex paddle is used, the breast thickness decreases towards the nipple side, resulting in a wedge-shaped breast. Since the AGD models assumes a flat shape, apart from general inherent uncertainties, there are additional uncertainties dues to the paddle tilt. In a clinical framework, no difference is made between the flex and rigid paddle for the AGD computation (Broeders et al., 2015). To our knowledge, the associated errors are 1935 not quantitatively described in the literature.

Recent reports have updated dose estimates from screen-film mammography and digital mammography, indicating that two-view screening with DM delivers a slightly lower dose

than does SFM . The mean average dose was estimated for different populations. A geographical classification shows that, the AGD delivered at digital breast for an European woman, on average, is higher ($1.48mGy$) than for North American ($1.42mGy$) or Asian woman ($1.42mGy$) (Geeraert et al., 2012). Østerås et al. (2018) have classified the CC and MLO view of 3819 women in two class by breast density. The authors reported a mean AGD of $1.73mGy$ for the dense breast and an AGD of $1.74mGy$ for the fatty breast. The AGD was estimated using the model proposed by Dance et al. (2000) .

1945 4.4.3 Pain and discomfort

Many women have reported discomfort or pain during mammography. A literature review over the last decades shows that the prevalence of pain varies widely, the percentage of women experiencing pain or discomfort are ranging between 16% and 72% (Keemers-Gels et al., 2000; Peipins et al., 2006; Dullum et al., 2000; Whelehan et al., 2013). This difference could be due to the interpretation of pain intensity, i.e. distinction between *pain* and *considerable pain*; but also could be attributed to differences in the instruments used to measure pain.

Pain intensity is influenced by the meaning of the pain to the patient and its expected duration. The environment also has an impact on the experience of pain, as do expectations, attitudes and beliefs. Pain is rarely caused by psychological factors but is associated with psychological and emotional effects such as fear, anxiety and depression (Williamson and Hoggart, 2005).

The three most-used pain metrics for clinical studies are the visual analogue scales, numeric rating scales and verbal rating scale (Williamson and Hoggart, 2005). The **1960 visual analogue scale** (VAS) is presented as a 10-cm continuous line together with a verbal descriptors at the line's ends ('no pain' and 'worst imaginable pain'). The patient is asked to mark on the line the pain intensity. The score is measured from the zero to the patient's mark using a millimeter scale which provide 101 levels of pain intensity. The **numerical rating scale** (NRS) is a discrete point scale were the end points are the extremes of the 1965 pain. In mammography a 6 or 11 points scale is generally used. The patient will mark the point corresponding to the pain intensity. The **verbal rating scale** (VRS) comprises a list of adjectives used to denote increasing pain intensities, such as no pain, mild pain, moderate pain and severe pain. The patient will choose the adjective corresponding to the perceived pain intensity. According to (Williamson and Hoggart, 2005) the numerical 1970 rating scale provide a best trad-off between the metric sensitivity to pain intensities and the metric repeatability.

In mammography, the pain experienced by women during the exam depends on psychological (technician behavior, patient anxiety) (Aro et al., 1996), sociological (ethnicity, education level) (Dullum et al., 2000) and physiological factors (compression level, breast size)(Poulos et al., 2003). The correlation between discomfort and several social and psychological factors was studied by Dullum et al. (2000). The study does not include physiologic breast parameters of the patient. According to the authors, the only factors that were significantly associated with discomfort were the satisfaction with care and perception of

the technologist's *roughness*. Several studies have also suggested the pain expectation and
1980 the anxiety level as ones of the main risk factors associated with the pain (Aro et al., 1996; Williamson and Hoggart, 2005; Keemers-Gels et al., 2000; Askhar and Zaki, 2017).

It has been shown that the physiological factors such as breast thickness, breast size or menstrual are positively correlated with the patient comfort (Keemers-Gels et al., 2000; Hafslund, 2000). (Poulos et al., 2003) have studied the relationship between applied compression force, breast thickness, reported discomfort and image quality. The authors reported a significant relationship between patient discomfort and breast thickness. Women who reported severe discomfort had a mean thickness of the left breast of 50.2 mm when compressed. However, no significant relationship between the reported discomfort of the procedure and the applied compression force was found. According to the authors, force
1985 does not correlate well with subject discomfort since it does not account for differences in breast size.

A painful mammography contributes to non-re-attendance, Peipins et al. (2006) reported that 25% of US women rated their experience of screening 30 months after their latest mammogram as at least moderately painful. It would thus, appear plausible that
1990 remembered pain can possibly dissuade women from attending later screening.

4.5 Summary

The breast compression it an important part of the mammographic exam. A qualitatively applied compression improves the image quality, separate better breast tissues structures and reduce the absorbed dose. In the same time, the breast positioning and compression are
2000 the main source of discomfort experienced by the patient. Because anxiety is documented to be the most important contributor to procedural pain, interventions designed to reduce both physical and psychologic discomfort are needed.

Considering the previous listed risk factors, various pain reducing techniques concerning the usual care were proposed during the last years (Miller et al., 2008). To decrease the
2005 patient anxiousness and pain expectations verbal and written information was proposed prior to mammogram. Informing the patient and accompanying them during the exam have shown to decrease the population mean pain score from 25 to 17 in a 100-mm VAS (Shrestha and Poulos, 2001). In the same time, the effect of relaxation techniques has been studied. Domar et al. (2005) compared the perceived pain from an usual mammogram to
2010 the one accompanied by music or an relaxation audiotape. The music subjects had a choice of classical music, jazz, or soft rock. The relaxation audiotape contained information that led the subject through breath focus, body scan, and meditation. According to the authors, where was no significant difference in perceived pain between the different groups.

Later, with the emergence of digital mammography, pain reducing compression techniques were proposed. Several studies (Chida et al., 2009; Saunders and Samei, 2008) suggest that the compression force may be reduced by at least 10% without a significant impact on image quality or average glandular dose. However, according to Poulos et al.
2015 (2003), the patient comfort is not related to the applied force intensity but to the com-

pressed breast thickness, which in its turn is associated with the breast size and firmness.
2020 To achieve the optimal compression considering the patient breast specific morphology, a pressure controlled compression is recommended instead of a force controlled compression (de Groot et al., 2015). The target recommended pressure is equal to 10 kPa . for a clinical integration, SegmaScreening company have proposed a new standard rigid paddle with integrated pressure control and Volpara Solutions company proposed a software computing
2025 the contact area between the breast and the compression paddle in order to extrapolate the mean applied pressure. In the same time, Dustler et al. (2012b) analyzed alternative breast positioning according to previously founded pressure distribution patterns. Because of stiff juxtathoracic structures, the authors proposed to increase the distance between the compression paddle and the chest wall by 1cm. The results have shown that within the new
2030 breast positioning, the pressure is reduced on the juxtathoracic area. The breast thickness was reduced by $4.4 \pm 2.3 \text{ mm}$ with no significant effect on force intensity. However, the six participants have identified the repositioned compression as the most painful, which, according to the authors, may be explained by the higher pressure intensities on the overall breast surface itself. The main drawback of this techniques is the exclusion of juxtathoracic
2035 tissues which may obscure small posterior cancerous tumor.

According to latter studies, several constructors started to propose different solution to reduce the physical discomfort during mammography. HOLOGIC company proposed the MammoPad cushions which is claimed to reduce the discomfort by 50%. In the review proposed by Miller et al. (2008), the radiolucent breast cushions on the equipment are
2040 presented to reduce the pain score (100mm VAS) from 35 to 20 in CC view and from 43 to 26 in MLO. GE-Healthcare company proposed a patient-controloed breast compression with the new Senographe Pristina Dueta system. This technique lets women undergoing an exam to control how much the device compresses the breasts. The breast is firstly positioned by the technologist between the compression plates and then, the patient has
2045 control in terms of how much compression she's willing to take. It have been shown that the patient-controlled compression is less painful than the techologist-controlled compression with no significant impact on image quality (Miller et al., 2008)

The breast positioning is a fastidious task for the technologist; for example, a greater amount of posterior tissue included in breast compression may results in a thicker breast
2050 at the anterior area, which in its turn may reduce the image quality and hide important clinical information. The technologist has the critical job of applying positioning methods using common sense, if the breast area is not well covered by the first two projections, an additional third projection may be necessary. The use of the flex paddles proposed by some constructors, such as American Mammographics S.O.F.T. Paddle, Ge-Healthcare
2055 Flex Paddle or Hologic FAST Paddle may increase the area of compressed tissues and thus to avoid an additional projection.

To our knowledge, there is only one study assessing the difference in image quality, average glandular dose and patient comfort between flex and rigid paddles. According to the authors the flex paddle affects the technical image quality without improving the
2060 patient experience. Because the flex paddle pulls the soft tissues towards the pectoral wall, they are less visible in the mammographyc image. It must be highlighted that, the

*CHAPTER 4. BREAST COMPRESSION
STATE OF THE ART*

study included CC and MLO projections with force-controlled compression (target force between 12-20 daN); based on the same principle as the one presented by Dustler et al. (2012b), one may guess that the breast compression with a flex paddle will results in a higher pressure over the breast surface itself (less pressure on the juxtathoracic area) which may be the origin of the pain. It may be interesting to assess the patient discomfort and the image quality with a pressure-controlled compression. Moreover, the average glandular dose is computed by neglecting the wedge form of the flex paddle, therefore it is difficult to measure the difference between flex and rigid paddle.

To better quantify the difference between flex and rigid paddles, further investigations are needed. In this scope, we have developed a simulation framework allowing to assess breast compression quality in function of breast patient specific morphology and compression paddle design. This simulation environment will allow us not only to evaluate the existing compression techniques, but also to perform a first evaluation of new, not yet conceived, paddles designs at a numerical level.

In the next chapter, we describe the breast compression by FE modeling as well as the numerical methods to assess the corresponding image quality and the average glandular dose. In a simulation framework, it is almost impossible to model the psychological patient discomfort, thus this work is focused on analyzing the patient physical discomfort which here is associated with tissues internal strain/stress due to breast compression. Ultimately, the breast compression quality for CC view is evaluates for flex and rigid paddles using 2 different breast geometries.

5

BREAST COMPRESSION & COMFORT *A comparative study*

2085 In the next chapters, a numerical simulation tool enabling the characterization of existing breast compression techniques in terms of patient comfort is developed. The latter would serve to build an optimal compression paddle considering the patient experience during mammography.

2090 In this purpose, MR images of two subjects are used to create patient specific finite elements breast models. The mechanical behavior of soft tissues under compression is computed for both subjects and for both paddle designs. The perceived pain for a given paddle design is quantitatively characterized by contact pressure, internal stress and strain distributions. After compression, three sets of macrocalcifications are inserted into breast volumes. The latter are then subject to a Monte-Carlo based simulation (CatSim) enabling 2095 to simulate the image acquisition of the compressed breast with a mammography system. Then, the diagnosis quality is assessed by measuring the signal-difference-to-noise-ratio (SDNR), signal-to-noise-ratio (SNR) and the average glandular dose (AGD).

5.1 Breast compression modeling

To asses the compression quality then using a flex or a rigid paddle FE simulations were performed. For this study, the data of both volunteer are used to develop two breast models with differences in breast geometries and mechanical properties. The realism of the simulation was verified by comparing the resulting breast thickness and compression force to the corresponding data of the last volunteer's mammogram.

5.1.1 FE modeling of compression paddles

In this study, standard paddle generally used for regular screening will be considered. Only one paddle geometry was considered based on the technical specifications from a Senograph PristinaTM mammography unit (GE-Healthcare, Buc, France). The paddle flexibility due to the material properties was neglected. The SRP was therefore defined as a fully rigid body with only one translational degree of freedom in the downwards direction. For the SFP, a rotation around the longitudinal axis is added. An additional degree of freedom was modeled using a rotational-only joint type of element.

The joint stiffness was computed by fitting the force-deflection curve of a flex paddle from a Senograph PristinaTM unit. A rigid plate was fixed at the external edge between the bucky and the SFP (Figure 5.1.a). To ensure the paddle rotation about the Oy axis only, the rigid plate was chosen to have the same length (in Oy direction) as the compression paddle. The deflection angle was measured using a digital inclinometre ($\pm 0.1\text{deg}$ accuracy). The paddle was lowered progressively, such as the deflection angle was incremented by about 0.5deg , until the maximal recommended compression force is reached ($F = 200\text{N}$). At each step, the compression force was read from the calibrated mammograph unit. The experiment was repeated 3 times. The relation between the mean compression force and the deflection angle is shown in Figure 5.1.b. The estimated second degree polinomial was used to define the joint stiffness for the FE analysis.

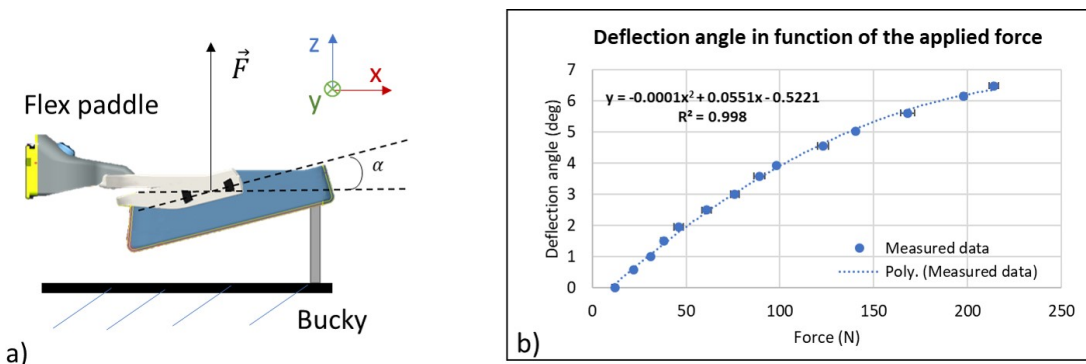


Figure 5.1: a) Experiment set-up, b) Deflection angle in function on the applied force

The interaction between the compression paddle and the breast was modeled using a

frictionless contact. The penalty algorithm was used with a penetration factor equal to 0.1
2125 and a contact stiffness equal to 1.

5.1.2 Breast compression mechanics

The compression of small breasts may be complex. Sometimes the technologist have to hold the breast between the bucky and the paddle until the compression force is high enough to preclude breast from sliding outside of the compression area. These difficulties
2130 are also meet in a simulation framework, all the more so because the technologist breast manipulation is not reproduced. To facilitate the compression task, the following breast compression tests are made on the geometry of the second volunteer.

In a clinical framework, woman breast is compressed only in a up-right or prone body position. When breast is compressed the gravity induced tissues pre-stresses can be neglected when compared to the compression induced stresses (Han et al., 2012; Ruiter et al.,
2135 2006; Sturgeon et al., 2016). Therefore, for this section, the prone breast configuration was used as reference configuration by neglecting the tissues internal pre-stresses dues to gravity loading.

Previously developed biomechanical model is implemented using the breast geometry of
2140 the second volunteer. Because of the large computation time the constitutive parameters were not addapted to the volunteer-specific mechanical behavior. Their values were taken from the literature (Han et al., 2014; Rajagopal et al., 2007; Gefen and Dilmoney, 2007), and are the following $\lambda_{breast} = 0.5kPa$, $\lambda_{muscle} = 10kPa$, $\lambda_{skin} = 10$, $\lambda_{fascia} = 160kPa$.

To simulate the cranio-caudal incidence, the bucky is positioned at the inframammary
2145 ligament level while the paddle compresses the breast by a downward movement. The compression is stopped then the target breast thickness is reached. The target thickness is given by the data obtained during the volunteers last mammogram (Table 3.1). The Figure 5.2) shows the breast thickness as function of the applied force for the flex and the rigid paddles. The breast thickness is considered constant then compressing with the SRP,
2150 and is equal to the mean thickness when compressing with the SFP.

One can see that, the total compression force at the target breast thickness (50mm) is about 10 times lower then the force measured during the volunteer's last mammography (6N versus 94.8N). Even if the used mechanical properties are not the ones corresponding to the patient data, a force of 6N remains too low when compared to the standard
2155 compression force of 120N (Chida et al., 2009). Several compression were tested (paddle closer to the juxtathoracic area, frictional contact with different friction coefficient) without observing any significant increase of the compression force.

An analysis of the literature revealed that the constitutive parameters used for modeling the breast compression are higher than the ones used for modeling the breast deformation
2160 under gravity loading. Sturgeon et al. (2016) have modeled the tissues deformation under compression considering the initial shear moduli for the Neo-Hookean potential function equal to $\mu_{skin} = 88kPa$, $\mu_{adipose} = 1kPa$ and $\mu_{glandular} = 10kPa$. Moreover, the obtained compression force versus breast thickness relation dose not show an asymptotic behaviour as described by de Groot et al. (2015). Therefore, one can conclude that, for high strains,

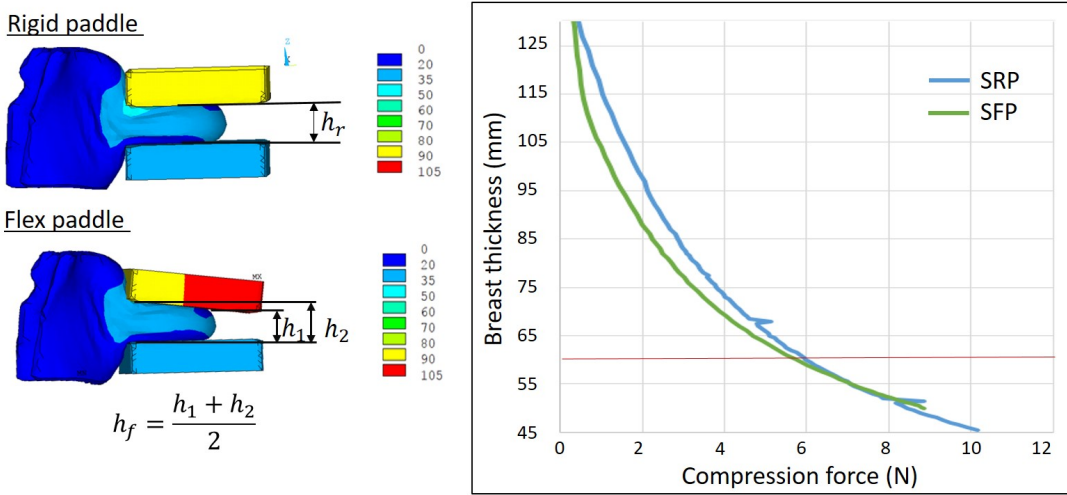


Figure 5.2: Breast flattening curve as function of the applied force for a Neo-Hookean strain energy function. SRP - standard rigid paddle, SFP -standard flex paddle

2165 the soft tissues undergo a stiffening process more rapidly than may be described by a Neo-Hookean law.

The limitations of the Neo-Hookean model to capture the mechanical response of some nonlinear materials is well known (Kaliske and Rothert, 1997). For large strain rates, the Neo-Hookean material may undergo a relaxation and therefore becomes easier to deform.
2170 Therefore, different strain energy models have to be considered for breast compression modeling.

Gent energy function

The Gent energy function (see Section 2.1.4.a) can be used as an alternative for soft tissues modeling. This energy function is characterized by three parameters (μ , K , and J_m). When 2175 $J_m \rightarrow \infty$, the Gent model is reduced to the Neo-Hookean model (Figure 5.3). Moreover, (Chagnon et al., 2004) shown that, for small deformations, the gent model is equivalent to the Neo-Hookean one regardless the J_m value. The J_m acts as a stiffening parameter and define the upper limit of the first invariant of the left Cauchy-Green deformation tensor.

These properties are particularly interesting for our simulation framework. In the previous chapter the material properties have been estimated and validated for multi-loading gravity simulations. Knowing that, the strain range due to gravity loading is smaller than the one due to breast compression. The J_m parameter may be computed such that, for relative small strain (about 80%) the Gent model will be equivalent to the Neo-Hookean model, however for larger strains ($> 80\%$) the energy function will behave asymptotically 2185 in order to approach a compression force equivalent to the standard compression force. In such case, only the third parameter of the energy function have to be estimated (J_m), assuming that the initial shear modulus (μ) and Bulk modulus (K) are already known

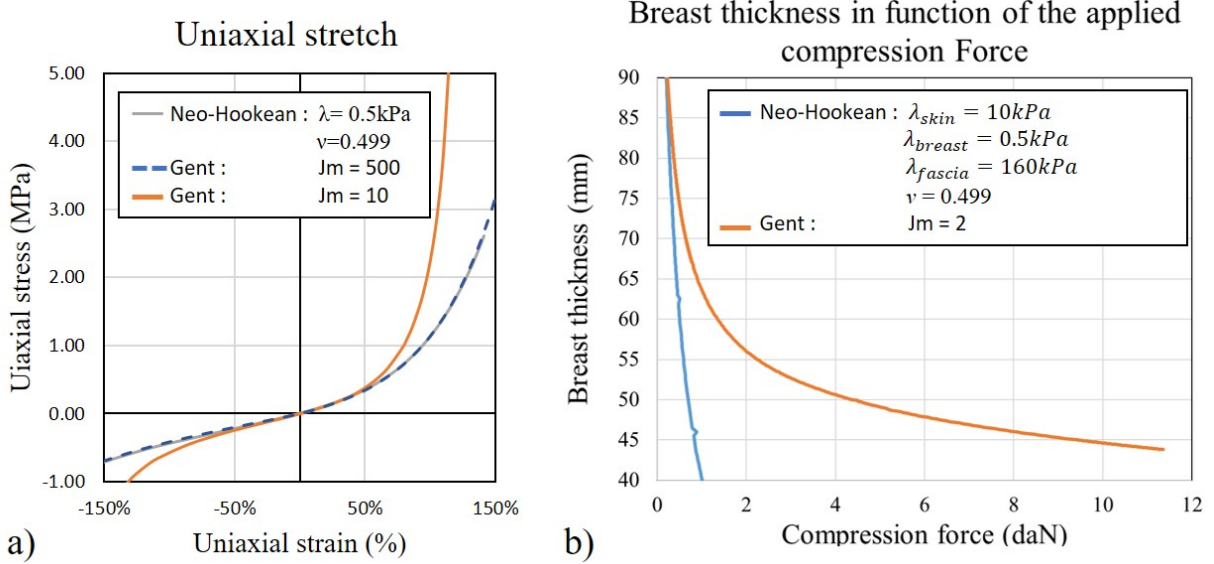


Figure 5.3: a) Stress-strain relation for Neo-Hookean and Gent energy function; b) Breast flattening curve as function of the applied force for a Gent energy function.

from the multi-loading gravity optimization process.

Figure 5.3.b shows the breast flattening curve as function of the applied force for Neo-Hookean and Gent models. One can see that, then using the Gent form the curve behavior is closer to the ones described by de Groot et al. (2015).

5.1.3 Updated material constitutive models

To compute tissues deformation under compression, the Gent energy function was used. The compression simulations were performed only on the right breast of both volunteers. The mechanical tissues properties of the first volunteer are set to the values obtained in the previous chapter ($\lambda_{breast}^r = 0.3\text{kPa}$, $\lambda_{skin} = 4\text{kPa}$, $\lambda_{fascia} = 120\text{kPa}$). As the optimization process was not performed for the second volunteer, the mechanical tissues properties are set to the values found in the literature ($\lambda_{breast} = 0.5\text{kPa}$, $\lambda_{muscle} = 10\text{kPa}$, $\lambda_{skin} = 10$, $\lambda_{fascia} = 160\text{kPa}$).

Several compression simulations using the standard rigid paddle were performed to determine the third parameter J_m . The value which results in a force-thickness relation passing through the point defined by the patient mammographic data (Section 3.1.1) is chosen. For the first volunteer, a breast thickness of 46mm with a compression force of 22N is obtained when $J_m = 1$. For the second volunteer, a breast thickness of 48mm for a compression force of 95N is obtained when $J_m = 2$. Because of convergence difficulties the Poisson ratio for these simulations was set to 0.499.

Figure 5.4 shows the breast flattening curve as function of the applied force obtained with SRP and SFP. All the simulations were performed with the new defined constitutive

parameters of the Gent model. The compression breast thickness at a given compression force is roughly equal for both paddles.

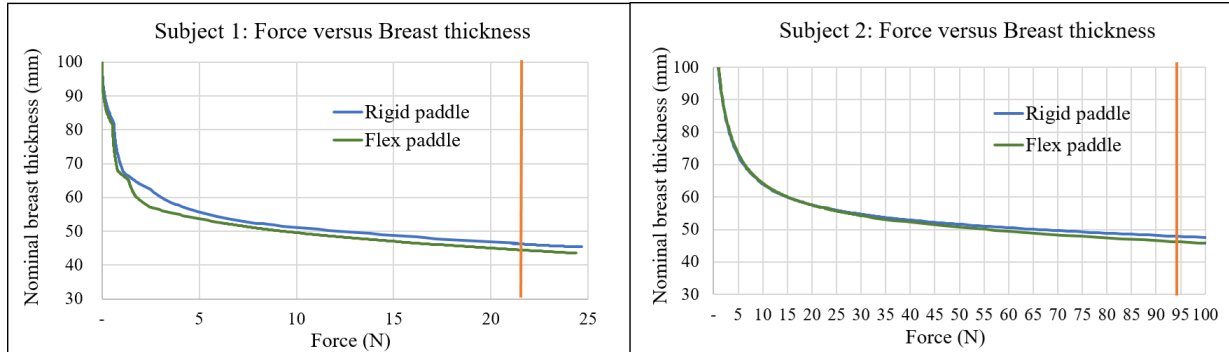


Figure 5.4: Resulting breast thickness for a given compression force

5.2 Simulation of digital images

Digital mammographyc images of the compressed breast were simulated using the CatSim simulation environment (de Carvalho, 2014). CatSim simulates the process of acquiring X-rays projections of phantom objects.

The phantoms were created by first extracting the compressed breast other shape. Then, in order to be able to asses the image quality, a set of microcalcifications were inserted into each compressed breast volume. The smallest breast volume contains 21 microcalcifications arranged in a matrix of 7 rows and 3 columns (Figure 5.5.a). The largest breast volume contains 56 microcalcifications arranged in a matrix of 7 rows and 8 columns. The matrix of calcifications is parallel with the entrance surface of the image receptor and positioned at the breast mid thickness (Figure 5.5.b). The distance between two consecutive columns or rows is equal to 10mm. The anatomical background was assumed to be a uniform breast-equivalent material composed of glandular/adipose tissue with a 20/80 ratio. Two simulations were performed for each compression considering μ_{calc} of 0.2 mm and 0.3mm in diameter.

Microcalcifications

Microcalcifications (μ_{calc}) were simulated as round-shaped surface mesh. To add irregularities and randomness, initially spherical objects were randomly deformed . The deformation consisted of two steps. First, the sphere surface was slightly deformed to a random ellipsoid along three randomly chosen axes, with maximum deformation magnitude set to five percent of the μ_{calc} diameter. Then the surface meshes were modified according to a stochastic Perlin noise to create irregularities. The Perlin noise deformation was done by locally displacing the vertices of a surface mesh in directions perpendicular to the mesh face. The displacement magnitude was set to $20\mu m$.

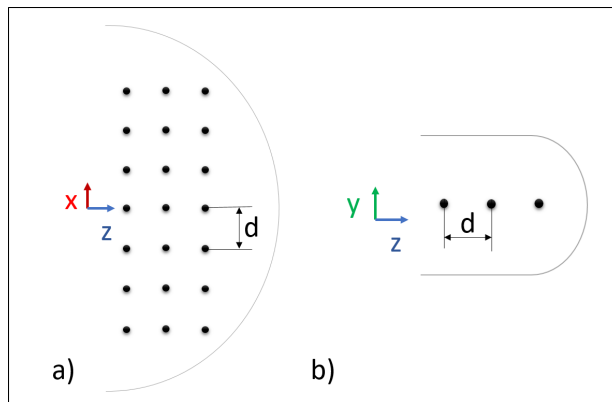


Figure 5.5: Microcalcification distribution over the smallest breast volume ($d = 10\text{mm}$): a) axial view, b) sagittal view.

2235 Microcalcifications with x-ray attenuation properties corresponding to the attenuation of aluminum (Al) at 24 keV and with a volumetric mass density corresponding to 60% of the Al density, i.e. 1.63 kgm^{-3} , were designed. The choice of 24 keV corresponded to the photon energy of the x-ray source used in our study. Al is less attenuating than the minerals 2240 composing real μ_{calc} which contain calcium carbonate, calcium oxalate or apatite. This is realistic since in real (μ_{calc}), the minerals are embedded in a protein matrix; therefore the attenuation of a (μ_{calc}) is lower than when considering only the minerals.

System topology

Topology of the DM image acquisition was modeled as follows. The source-to image distance (SID) was set to 660mm. The detector size was set to 150 mm in the x-axis direction 2245 and 170 mm in the z-axis direction. Isotropic detector pixels with size of 0.1 mm were simulated. Position of the x-ray source was modeled such that its projection along the y axis onto the detector plane falls exactly at the midpoint of the detectors left edge. The bucky and the compression paddle were modeled as two planes parallel to the detector.

Physical characteristics

2250 Physical characteristics of the imaging system were modeled as follows. A simplified mono-energetic x-ray source was used. The photon energy level was set to 24 keV, this is equivalent to the effective x-ray energy of a 34 kVp Rhodium (Rh)/Silver (Ag) target/filter spectrum used for imaging a 46 mm compressed breast. An ideal point source focal-spot was used. In order to simulate the detector unsharpness, a modulation transfer function empirically measured from the reference system was used by the simulator. X-ray scatter 2255 from the test object was not considered. Only Poisson x-ray noise was added and the electronic noise was not modeled.

A calibration was performed to match the signal-to-noise ratio (SNR) in simulated images with the SNR obtained in experimentally acquired images using the GE Senographe

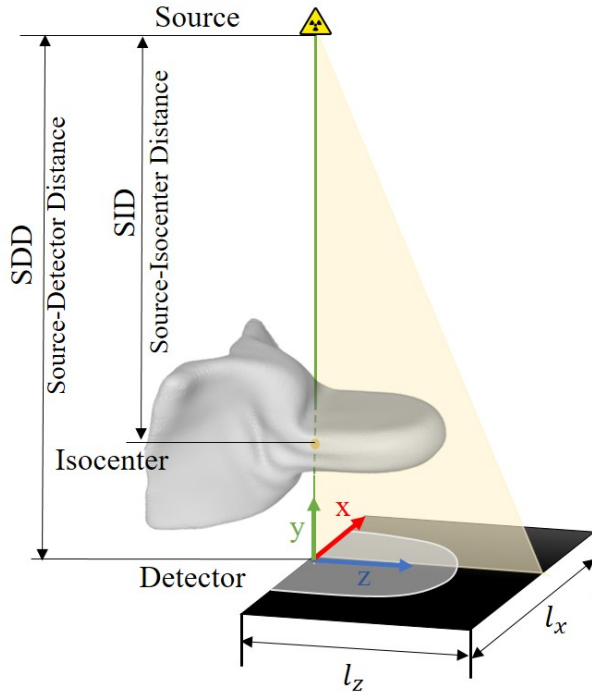


Figure 5.6: A schematic illustration og the simulated GE Senographie Pristina TM mammography unit.

2260 Pristina system with automatic optimization of parameters. The adjustment method is described as follows. On the GE Senographie Pristina system, FFDM central raw projection images were acquired from 2 phantoms (CIRS, Virginia, USA) with 100% adipose and 100% fibroglandular equivalent composition. The phantoms were positioned side-by-side on the breast positioning table. The acquisitions were repeated for five different breast thicknesses {45, 50, 60, 65, 70 (mm)}. Images of the 45mm thick phantom was acquired at 26 kVp, the images of the others four phantoms were acquired at 34 kVp. A Rh/Ag target/filter combination was used with the AOP mode. SNR values were measured in the raw projection images (processed only with the manufacturers gain, offset, and defective pixel correction), in $2\text{cm} \times 2\text{cm}$ square ROIs at 5 cm from the chest wall. SNR was defined as $\frac{\langle SI \rangle}{\sigma_{SI}}$, where $\langle SI \rangle$ is the average detected signal intensity per pixel and σ_{SI} is the standard deviation in the signal intensity. The corresponding experiments was then simulated. The mAs value in the simulation was adjusted so as SNR values in the simulated and experimentally obtained images were found similar. Due to restrictions of the x-ray simulator, it was not possible to exactly match the SNR for both 100% adipose and 100% fibroglandular regions. The mAs in the simulations was therefore adjusted till SNR differed by maximum 10% in both breast-tissue equivalent.

5.3 Compression quality metrics

5.3.1 Patient comfort

Today, the pain estimation and quantification still remains an open question. During 2280 mammography, the perceived pain, or it's interpretation, may depend on the social status, pain history or psychological condition of the patient. But can also depend on the physical parameters as the compression force, amount of deformation or pressure on the skin surface. In clinical studies the patient comfort is studied using pain scales. The repeatability of such 2285 methods are questionable, because they are based on the patient own interpretation and expertise. More quantitative measures such as pupil dilatation, heart rate are interesting in assessing the patient comfort, however they may indicate not only the pain but also the fear of pain.

In this work, only the physical pain associated with tissues deformation was considered. In this scope, the maximal stain and stress intensities as well as the maximal pressure intensity 2290 at the contact surface between the breast and the compression paddle were chosen as pain quantifiers. Their distribution over the breast volume were obtained from FE simulation of breast compression and were analyzed in order to compare the patient experience between two distinct compressions.

5.3.2 Image quality

To asses the image quality the signal-difference-to noise ratio (SDNR) per pixel of the 2295 inserted microcalcifications was measured in the raw projection images. Squared ROIs of $1cm \times 1cm$ centered on the $\mu calc$ s position were defined to compute the average detected signal per background pixel $\langle SI_{back} \rangle$ and the standard deviation in the background signal intensity σ_{back} . The SDNR is defined as follows

$$SDNR = \frac{\langle SI_{back} \rangle - \langle SI_{\mu calc} \rangle}{\sigma_{back}}, \quad (5.1)$$

were $\langle SI_{\mu calc} \rangle$ is the average detected signal per $\mu calc$ pixel.

Additionally, the SNR was computed on the same ROIs as follows

$$SNR = \frac{\langle SI_{back} \rangle}{\sigma_{back}}. \quad (5.2)$$

5.3.3 Average glandular dose

The average glandular dose was derived using the approach proposed by Dance et al. (2000) regardless the paddle type. In practice, it is very difficult to accurately measure the exact 2305 breast thickness. Thus, the nominal breast thickness was used to compute conversions factors which relate measurements of incident air kerma to the delivered mean glandular dose.

5.4 Results

With a rigid paddle, the breast under compression presents a nearly uniform thickness all over the contact surface. Contrariwise, with a flex paddle, the compressed breast thickness decreases quasi linearly from the chest wall to the nipple. Flex paddles are used to better conform the breast contours and thereby to improve compression. However, Broeders and colleagues¹¹ have shown that such compression paddle may decrease the diagnostic quality of mammograms as the breast tissues may be pushed out to the chest wall resulting in less retro-glandular tissue visible on the image.

The resulting internal stress and strain distributions, as well as contact pressure maps were derived at compressive forces of 22 N for the first volunteer (Figure 5.7) and 95 N for the second one (Figure 5.8).

As concerns the small breast volume (Figure 5.7), there is no significant difference between FCP and RCP in pressure distribution over the skin surface or in internal stress/strain intensity distributions. For both compression paddles, high pressure at the skin surface is concentrated in the juxtathoracic region with a maximum pressure of 77.7 kPa. Several clinical studies^{11,13} sustained this result of no significant difference in experienced pain when using FCP or RCP. In addition, the FE simulations confirm that in small breasts the paddle tilt is too small to impact the tissues compression in the middle part of the breast. FCP applied on large breast volumes (Figure 5.8) results in significantly lower intensities of pressure at the skin surface in contact with the compression paddle, with a maximal pressure of 37 kPa, compared to 56 kPa when using RCP. No significant difference in the measured maximal intensities of strain and stress was observed, however strain and stress distribution patterns are different. When the breast is compressed with a rigid paddle, maximal strain and stress are concentrated in the retromammary space and decrease considerably toward the nipple. When a flex paddle is used, stress and strain are more uniformly distributed over the breast volume with the highest values in the middle third of the breast. The areal pressure distribution patterns has already been demonstrated in the work by Dustler and colleagues¹³. The authors have studied the pressure distribution patterns of 103 women undergoing breast compression with a rigid paddle at different compression levels. Four groups have been differentiated: a) skin pressure widespread over the breast (29%); b) skin pressure concentrated on the central part of the breast (8%); c) skin pressure concentrated on the juxtathoracic region (16%); d) skin pressure concentrated along a narrow zone at the juxtathoracic region (26%). The pressure distribution patterns observed for our first and second volunteers correspond to the group d and a respectively.

The nominal breast thickness may vary by about 2mm between rigid and flex paddle for both volunteers (Table 5.9). Accordingly, no significant difference was found between the estimated AGD, while a dose reduction of 2% for the smaller breast and 4% for larger breast was observed.

The SNR and SDNR have been estimated and compared between flex and rigid paddles. When using a flex paddle instead of a rigid paddle on the largest breast (volunteer 2), we observe a statistically significantly higher SNR. The same trend is observed on SDNR

*CHAPTER 5. BREAST COMPRESSION & COMFORT
A COMPARATIVE STUDY*

for both 200 and 300 m microcalcifications, while not statistically significant. We did not observe any statistically significant difference in SNR or SDNR for microcalcification of any size when considering the compression of the smallest breast by a rigid or a flex paddle. Therefore, despite a breast thickness varying linearly from chest wall to nipple when the flex compression paddle is used, the image quality is preserved or improves compared to the image quality obtained with the rigid compression paddle.

*CHAPTER 5. BREAST COMPRESSION & COMFORT
A COMPARATIVE STUDY*

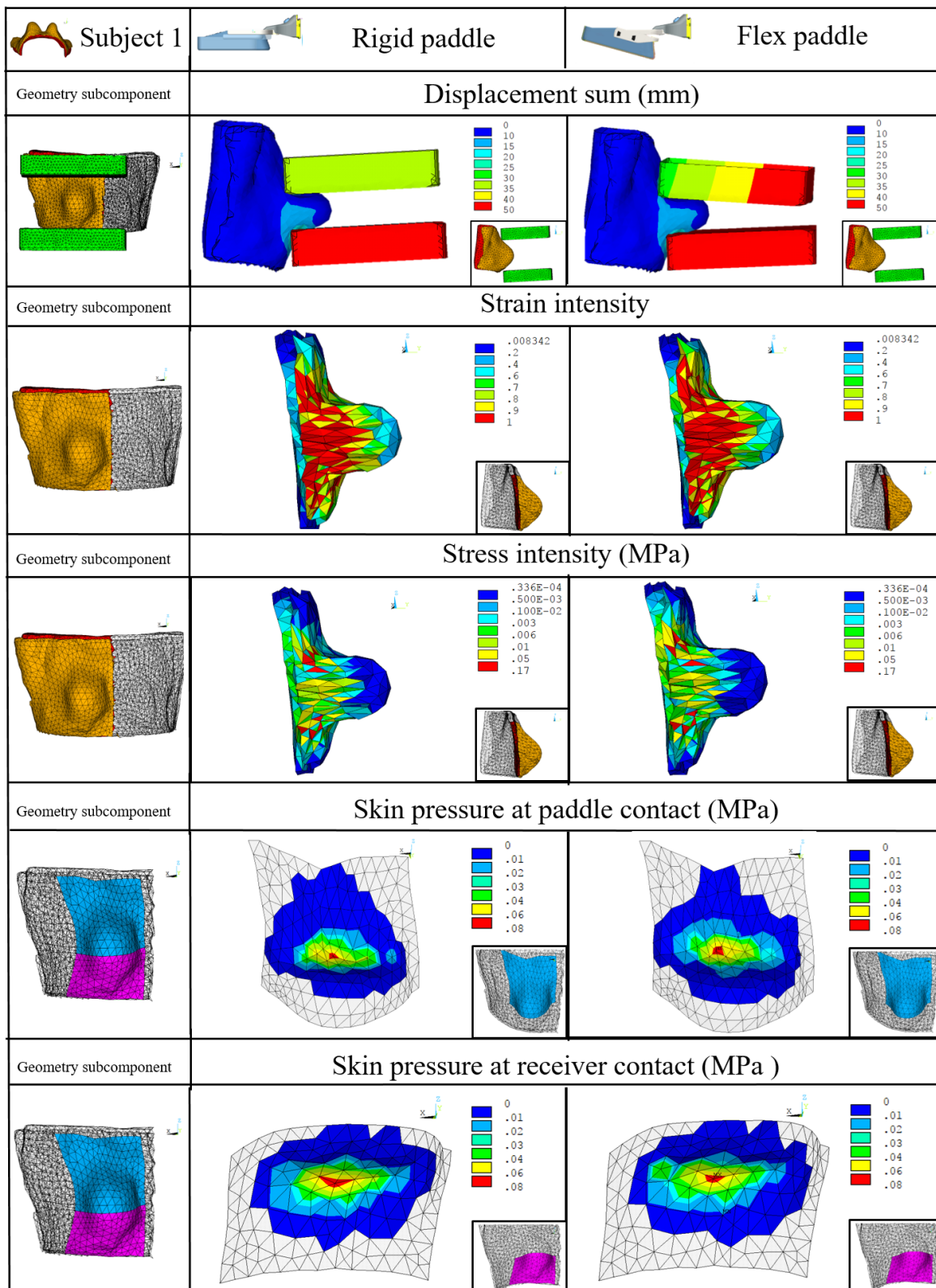


Figure 5.7: Stress, strain and contact pressure distribution for the first subject

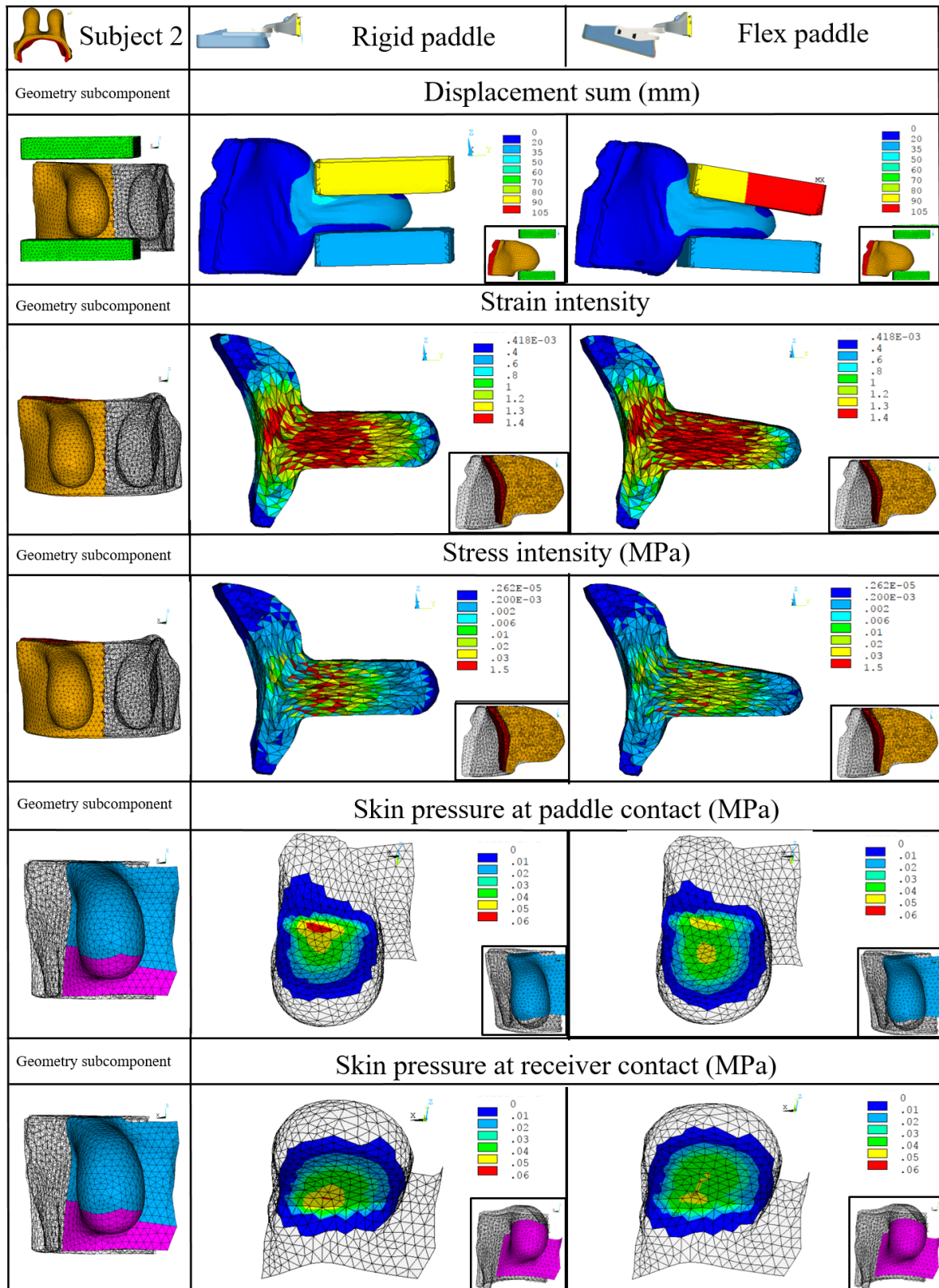


Figure 5.8: Stress, strain and contact pressure distribution for the second subject

*CHAPTER 5. BREAST COMPRESSION & COMFORT
A COMPARATIVE STUDY*

	Rigid Paddle		Flex Paddle		p-Values	Rigid Paddle		Flex Paddle	
	Mean SNR	StdDev SNR	Mean SNR	StdDev SNR		BNT (mm)	AGD (mGy)	BNT (mm)	AGD (mGy)
Volunteer 1	82.90	43.09	83.70	37.72	0.706	46	1.15	44	1.12
Volunteer 2	126.89	8.75	137.21	10.73	0.000	48	1.20	46	1.15

	200 um					300 um				
	Rigid Paddle		Flex Paddle		p-Values	Rigid Paddle		Flex Paddle		p-Values
	Mean SDNR	StdDev SDNR	Mean SDNR	StdDev SDNR		Mean SDNR	StdDev SDNR	Mean SDNR	StdDev SDNR	
Volunteer 1	0.74	0.68	0.79	0.54	0.689	2.01	1.28	1.85	1.02	0.224
Volunteer 2	1.14	0.57	1.13	0.53	0.885	2.96	0.76	3.15	0.92	0.093

Figure 5.9: Breast nominal thickness (BNT), average glandular dose (AGD), signal-to-noise-ratio (SNR) and signal-difference-to-noise (SDNR) for both volunteers and both compression paddle types

2355 **5.5 Discussions and conclusion**

Breast compression with flex and rigid paddle have been simulated using the finite elements theory applied to segmented MRI images acquired on 2 volunteers under different geometries. Applying the Gent form of strain-energy potential, instead of the Neo-Hookean form, allowed to obtain compression force magnitudes comparable with the real subject data. After simulating the breast compression, the SDNR of microcalcifications and the AGD, delivered during the acquisition of the corresponding simulated mammography, have been computed. The simulations have been repeated for two different breast volumes (cup sizes A and F) with a rigid and a flex paddle. The four configurations have been analyzed to compare patient perceived pain (measured as strain and stress) and image quality (measured as SNR, SDNR and AGD). The results of our simulations indicate that, for the smallest breast, there is no significant difference for the patient perceived pain when using the rigid or the flex paddle. The shape of the breast under compression does not present significant changes between the two paddle designs. We did not observe any statistically significant difference in SNR or SDNR for microcalcification of any size when considering the compression of the smallest breast by a rigid or a flex paddle. Therefore, our results suggest that using a flex paddle should not significantly impact image quality and delivered dose in small breasts, and should not reduce significantly the perceived pain. For the largest breast, our simulations indicate that using a flex paddle may reduce the maximal pressure intensity on the skin surface by about 30% compared to the rigid paddle. The tissue deformation is more uniformly distributed inside the breast volume, and the highest deformation is occurring in the middle breast region corresponding to the supposed location of dense tissues. Moreover, our simulations have shown that flex paddle have no significant impact on the average glandular dose and improves image quality compared to the rigid paddle. In conclusion, our simulations confirm that using the flex paddle used for breast compression may improve the patient comfort without affecting the image quality and the delivered average glandular dose. Moreover, despite a breast thickness varying linearly from chest wall to nipple, when a flex compression paddle is used on large breasts, the image quality seems to be preserved or improved compared to the image quality obtained with a rigid compression paddle

2385

CONCLUSION

KEY CONTRIBUTIONS

PERSPECTIVE

Appendices



DISTANCE MEASURES

For the sake of simplicity, only the distance between discrete 3D-surfaces represented by triangular meshes will be defined. A discrete 3D-surface is usually represented by a set of point $S = \{p^1, p^2, \dots, p^n\}$; thus, the similarity between two surfaces is measures by computing distance measures between the respective points sets.

First, the definition pf the point to point Euclidean distance is given, followed by different surface to surfaces distances derived form the Euclidean one.

Euclidean distance between two points

The Euclidian distance is defined as the shortest possible path through space between two points, also called the $L^2 - norm$. Let consider two points p and p' defined in a 3-dimensional space, the distance magnitude is defined as

$$D(p, p') = \|p - p'\|_2 = \left(\sum_{n=0}^3 |p_i - p'_i|^2 \right)^{\frac{1}{2}} \quad (\text{A.1})$$

Node to surface distance

The distance $D'(p, S')$ between the point p and the surface S' is defined as

$$D^s(p, S') = \min_{q \in S'} \|p - q\|_2 \quad (\text{A.2})$$

Minimal distance between two surfaces

The minimal distance between two surfaces S and S' is defined as

$$D_{min}^S(S, S') = \min_{p \in S} \{D^s(p, S')\} \quad (\text{A.3})$$

Maximal distance between two surfaces

The maximal distance between two surfaces S and S' is defined as

$$D_{max}^S(S, S') = \max_{p \in S} \{D^s(p, S')\} \quad (\text{A.4})$$

²⁴¹⁰ **Mean distance between two surfaces**

The mean distance between two surfaces S and S' is defined as

$$D_{mean}^S(S, S') = \frac{1}{|S|} \sum_{p \in S} D^s(p, S') \quad (\text{A.5})$$

where $|S|$ is the number of nodes bellowing the surface S .

Hausdorff distance between two surfaces

The Hausdorff distance (Huttenlocher et al., 1993) between two surfaces is defined as

$$H(S, S') = \max \{D_{max}^S(S, S'), D_{max}^S(S', S)\} \quad (\text{A.6})$$

²⁴¹⁵ **Modified Hausdorff distance between two surfaces**

The modified Hausdorff distance between two surfaces is defined as

$$H(S, S') = \max \{D_{mean}^S(S, S'), D_{mean}^S(S', S)\} \quad (\text{A.7})$$

Dubuisson and Jain (1994) have studied 24 measures to asses the similarities between two discrete surface mesh. According to the authors, Hausdorff distance have the best performance for object matching.

B

2420

MESH CONVERGENCE

In finite element modeling, a finer mesh typically results in a more accurate solution. However, as a mesh is made finer, the computation time increases. To get a mesh that satisfactorily balances accuracy and computing resources a mesh convergence study was
2425 performed

In this scope, the breast and muscle geometries was meshed with different mesh sizes; the minimal elements sizes was set to 7mm and the maximal element size was varied between $\{7\text{mm}, 10\text{mm}, 13\text{mm}, 15\text{mm}, 17\text{mm}, 20\text{mm}\}$. The compression paddles geometries were meshed with a constant element size of 1mm . The number of elements obtained
2430 for each mesh size is given in Table B.1. For the mesh size equal to 17 mm , a higher number of elements is obtained then compared to the mesh size of 15mm . As mesh size is defined by the maximal and minimal elements size, a higher number of *small* elements was needed to cover the areas smaller than the *large* elements. In such meshes the elements density is normally concentrated on the geometry's corners or narrow spaces which, in our
2435 case, dose not coincide with the region of interest.

Mesh size	20mm	17mm	15mm	13mm	10mm	7mm
Nb. of elements	8367	10897	8099	10751	18453	65785

Table B.1: Number of elements obtained for each mesh size.

As the model was conceived to model breast deformation under compression, an equivalent simulation was performed to estimate the optimal mesh size. Starting from the breast supine geometry, the gravity was applied in the posterio-anterior direction. Then, the right breast was compressed between the compression paddles (Figure B.1). The strain distribution over the breast volume as well as the compression force for each mesh size are
2440 given in the Figure B.1.

One can see, that the force intensity converges from a mesh size equal to 15mm , however the strain distribution over the breast volume have still a poor estimation when compared to the strain distribution obtained with a mesh size equal to 7mm . The visual analysis of

APPENDIX B. MESH CONVERGENCE

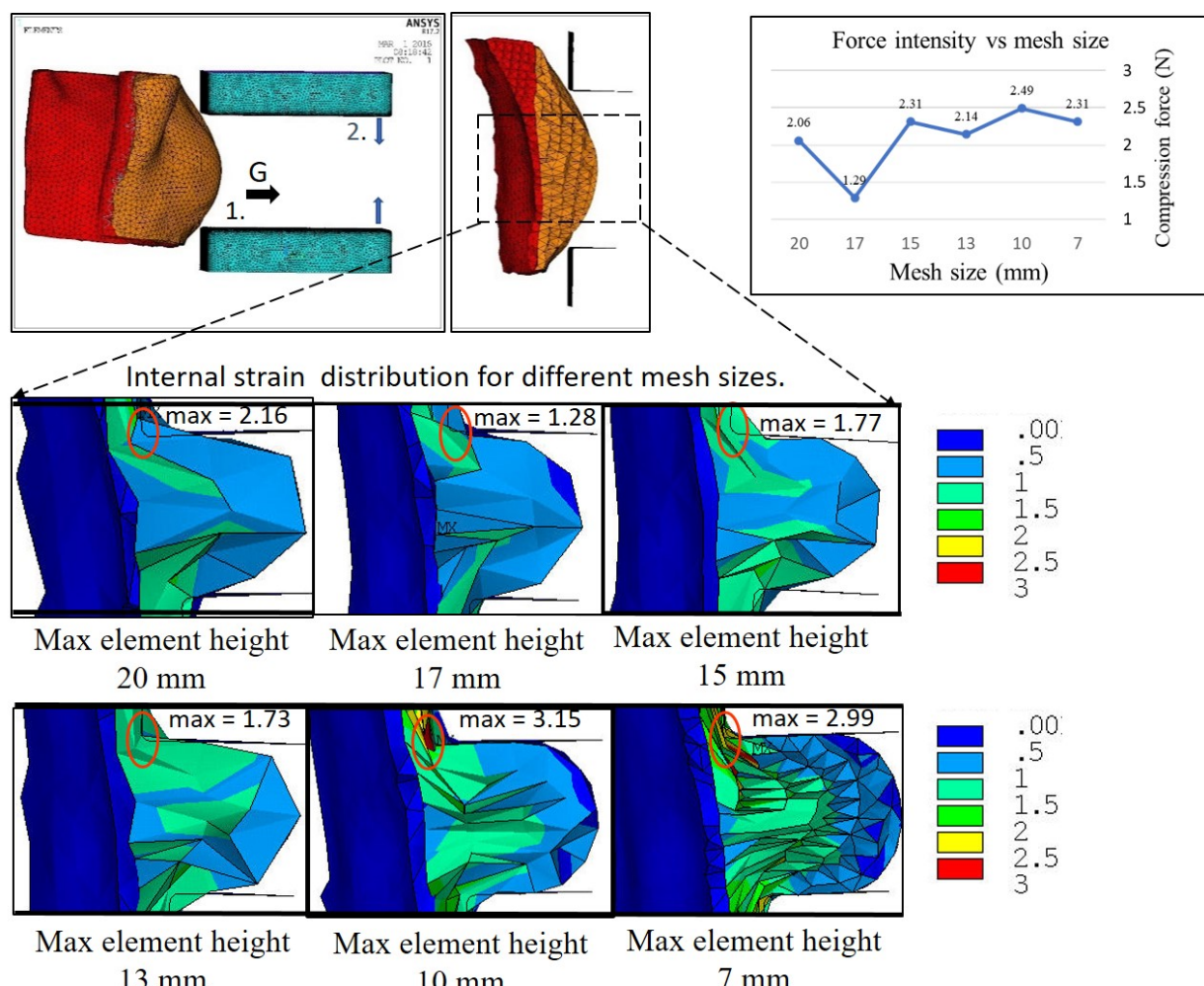


Figure B.1: Internal strain distribution in function of the elements size.

2445 the strain distribution and amount of penetration at the surface contact shows that starting from a mesh size equal to 10mm the results are well enough estimated.

C

BONDARY CONDITIONS *contact models*

The proposed biomechanical model consist of two bodies, one representing the pectoral cage and the second represents the breast soft tissues. Between the two bodies, a contact surface is defined in order to model tissues mechanics at the juncture interface.

The next sections describes the implementation of different interaction models that were tested during the implementation process. Since the breast tissues are attached to the pectoral muscle (Figure C.1), the contact surface was modeled using combinations of *bonded* and *no-separation frictional* interaction models.

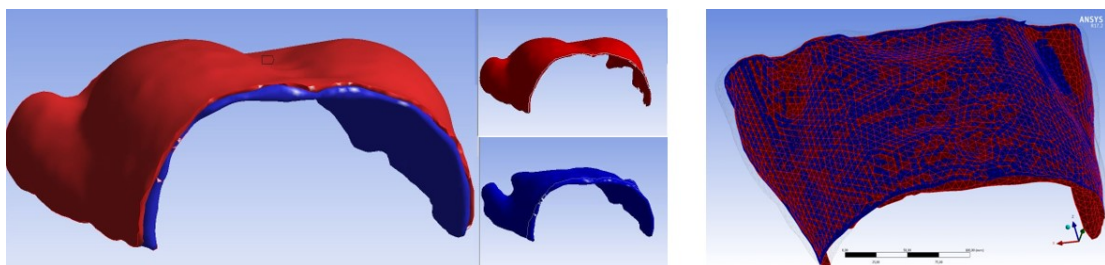


Figure C.1: The two bodies representing the thoracic cage and breast with the associated contact surface. Blue surface- the target surface, red surface - contact surface

The results for pure bonded, no-separation sliding models as well as one combined contact surface are listed bellow, with their impact on global breast deformation. For some models partial results are presented, because of important solution instabilities the deformed breast geometry is not available.

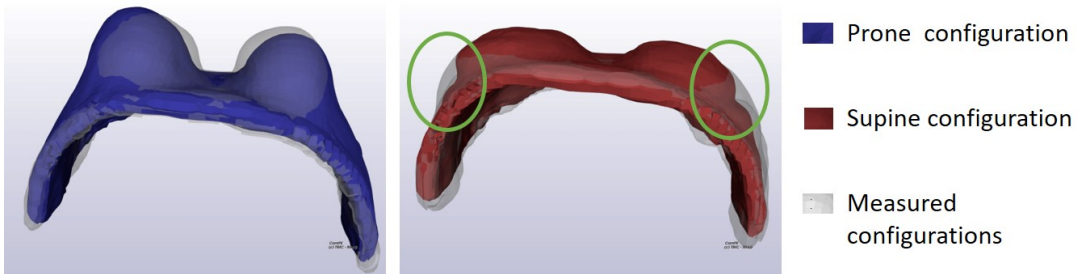


Figure C.2: Resulting breast deformation with a bonded contact model.

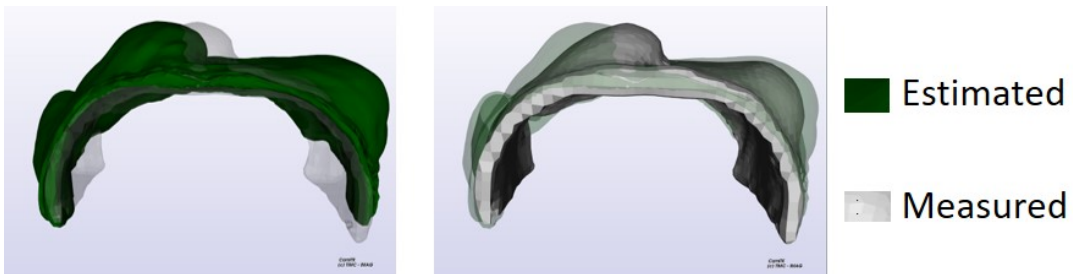


Figure C.3: Resulting breast deformation in supine tilted configuration with a sliding contact model.

2460 **Bonded contact surface**

Sliding contact surface

Mixt contact surface

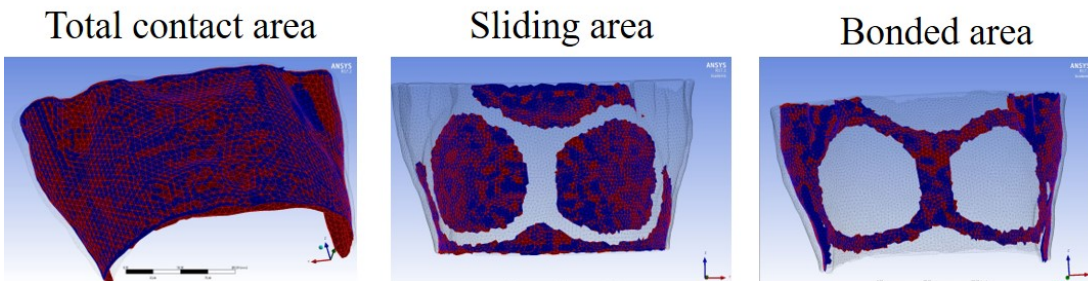


Figure C.4: The contact surface divided in two regions: sliding region and bonded region.

Sliding contact surface with ligaments

BIBLIOGRAPHY

Abeyaratne, R. (2012). *Continuum Mechanics: Volume II of Lecture Notes on The Mechanics of Elastic Solids*. Cambridge MA and Singapore. 22

Abu-Hijleh, M., Roshier, A., Al-Shboul, Q., Dharap, A., and Harris, P. (2006). The membranous layer of superficial fascia: evidence for its widespread distribution in the body. *Surgical and Radiologic Anatomy*, 28(6):606–619. 13
2470

ACS (2017). American cancer society: Types of breast cancer. <https://www.cancer.org/cancer/breast-cancer/understanding-a-breast-cancer-diagnosis/types-of-breast-cancer.html>. 15, 16

Andolina, V. and Lillé, S. (2011). *Mammographic imaging: a practical guide*. Lippincott Williams & Wilkins. 12, 13, 14, 15, 79
2475

Andrews, F. J. (2001). Pain during mammography: implications for breast screening programmes. *Journal of Medical Imaging and Radiation Oncology*, 45(2):113–117. 19

ANSYS (2017a). *ANSYS Contact Technology Guide*, 17 edition. 41, 61

ANSYS (2017b). *Theory reference for the mechanical APDL and mechanical applications*, 17 edition. 35
2480

Aro, A. R., Absetz-Ylöstalo, P., Eerola, T., Pamilo, M., and Lönnqvist, J. (1996). Pain and discomfort during mammography. *European Journal of Cancer*, 32(10):1674–1679. 2, 81, 82

Aro, A. R., De Koning, H. J., Absetz, P., and Schreck, M. (1999). Psychosocial predictors of first attendance for organised mammography screening. *Journal of Medical Screening*, 6(2):82–88. 19
2485

BIBLIOGRAPHY

- Askhar, L. K. and Zaki, Y. H. (2017). Female patients perception of pain caused by mammography in the western region of saudi arabia. *Saudi medical journal*, 38(7):768. 82
- 2490 Azar, F. S., Metaxas, D. N., and Schnall, M. D. (2002). Methods for modeling and predicting mechanical deformations of the breast under external perturbations. *Medical Image Analysis*, 6(1):1–27. 30, 45, 47, 48, 51
- Bayati, S. and Seckel, B. R. (1995). Inframammary crease ligament. *Plastic and reconstructive surgery*, 95(3):501–508. 12
- 2495 Belytschko, T., Liu, W. K., Moran, B., and Elkhodary, K. (2013). *Nonlinear finite elements for continua and structures*. John wiley & sons. 22, 34
- Boone, J. M. (1999). Glandular breast dose for monoenergetic and high-energy x-ray beams: Monte carlo assessment. *Radiology*, 213(1):23–37. 80
- 2500 Broeders, M. J., ten Voorde, M., Veldkamp, W. J., van Engen, R. E., van Lansveld-Verhoeven, C., NLt Jong-Gunneman, M., de Win, J., Droogh-de Greve, K., Paap, E., and den Heeten, G. J. (2015). Comparison of a flexible versus a rigid breast compression paddle: pain experience, projected breast area, radiation dose and technical image quality. *European radiology*, 25(3):821–829. 80
- Bucki, M., Lobos, C., and Payan, Y. (2010). A fast and robust patient specific finite element mesh registration technique: application to 60 clinical cases. *Medical image analysis*, 14(3):303–317. 59
- 2505 Calvo-Gallego, J. L., Martínez-Reina, J., and Domínguez, J. (2015). A polynomial hyper-elastic model for the mixture of fat and glandular tissue in female breast. *International Journal for numerical methods in biomedical engineering*, 31(9). 65
- 2510 Carter (2009a). *Determining material properties of the breast for image-guided surgery*. International Society for Optics and Photonics. 47, 48
- Carter, T., Han, L., Taylor, Z., Tanner, C., Beechy-Newman, N., Ourselin, S., and Hawkes, D. (2012). Application of biomechanical modelling to image-guided breast surgery. *Soft Tissue Biomechanical Modeling for Computer Assisted Surgery*, pages 71–94. 45, 60
- 2515 Carter, T. J. (2009b). *Biomechanical modelling of the breast for image-guided surgery*. PhD thesis, University of London. 43, 44, 45, 46, 48, 49
- Catanuto, G., Spano, A., Pennati, A., Riggio, E., Farinella, G. M., Impoco, G., Spoto, S., Gallo, G., and Nava, M. B. (2008). Experimental methodology for digital breast shape analysis and objective surgical outcome evaluation. *Journal of Plastic, Reconstructive & Aesthetic Surgery*, 61(3):314–318. 10
- 2520

BIBLIOGRAPHY

- Chagnon, G., Marckmann, G., and Verron, E. (2004). A comparison of the hart-smith model with arruda-boyce and gent formulations for rubber elasticity. *Rubber chemistry and technology*, 77(4):724–735. 88
- Chan, H.-P., Galhotra, S., Vyborny, C. J., MacMahon, H., Jokich, P. M., et al. (1987).
2525 Image feature analysis and computer-aided diagnosis in digital radiography. i. automated detection of microcalcifications in mammography. *Medical physics*, 14(4):538–548. 74
- Chen, B., Wang, Y., Sun, X., Guo, W., Zhao, M., Cui, G., Hu, L., Li, P., Ren, Y., Feng, J., et al. (2012). Analysis of patient dose in full field digital mammography. *European journal of radiology*, 81(5):868–872. 78
- Cheung, J. T.-M., Zhang, M., and An, K.-N. (2004). Effects of plantar fascia stiffness on the biomechanical responses of the ankle–foot complex. *Clinical Biomechanics*, 19(8):839–846. 49
- Chida, K., Komatsu, Y., Sai, M., Nakagami, A., Yamada, T., Yamashita, T., Mori, I., Ishibashi, T., Maruoka, S., and Zuguchi, M. (2009). Reduced compression mammography to reduce breast pain. *Clinical imaging*, 33(1):7–10. 82, 87
2535
- Chung, J.-H., Rajagopal, V., Nielsen, P. M., and Nash, M. P. (2008). Modelling mammographic compression of the breast. In *Medical Image Computing and Computer-Assisted Intervention MICCAI 2008*, pages 758–765. Springer. 47
- Ciocca, D. R. and Fanelli, M. A. (1997). Estrogen receptors and cell proliferation in breast cancer. *Trends in Endocrinology & Metabolism*, 8(8):313–321. 15
2540
- Clemente, C. D. (2011). *Anatomy: a regional atlas of the human body*. Wolters Kluwer-Lippincott Williams & Wilkins Health. 10, 11, 12, 60
- Conley, R. H., Meszoely, I. M., Weis, J. A., Pheiffer, T. S., Arlinghaus, L. R., Yankeelov, T. E., and Miga, M. I. (2015). Realization of a biomechanical model-assisted image guidance system for breast cancer surgery using supine mri. *International journal of computer assisted radiology and surgery*, 10(12):1985–1996. 43
2545
- Dance, D., Skinner, C., Young, K., Beckett, J., and Kotre, C. (2000). Additional factors for the estimation of mean glandular breast dose using the uk mammography dosimetry protocol. *Physics in medicine & biology*, 45(11):3225. 80, 81
- de Carvalho, P. M. (2014). *Low-Dose 3D Quantitative Vascular X-ray Imaging of the Breast*. PhD thesis, Université Paris Sud-Paris XI. 90
2550
- de Groot, J. E., Broeders, M. J., Grimbergen, C. A., and den Heeten, G. J. (2015). Pain-preventing strategies in mammography: an observational study of simultaneously recorded pain and breast mechanics throughout the entire breast compression cycle. *BMC women's health*, 15(1):26. 76, 79, 83, 87, 89
2555

BIBLIOGRAPHY

- Domar, A. D., Eyvazzadeh, A., Allen, S., Roman, K., Wolf, R., Orav, J., Albright, N., and Baum, J. (2005). Relaxation techniques for reducing pain and anxiety during screening mammography. *American Journal of Roentgenology*, 184(2):445–447. 82
- Dubuisson, M.-P. and Jain, A. K. (1994). A modified hausdorff distance for object matching. In *Pattern Recognition, 1994. Vol. 1-Conference A: Computer Vision & Image Processing., Proceedings of the 12th IAPR International Conference on*, volume 1, pages 566–568. IEEE. 107
- Dullum, J. R., Lewis, E. C., and Mayer, J. A. (2000). Rates and correlates of discomfort associated with mammography. *Radiology*, 214(2):547–552. 2, 19, 81
- Dustler, M., Andersson, I., Brorson, H., Fröjd, P., Mattsson, S., Tingberg, A., Zackrisson, S., and Fornvik, D. (2012a). Breast compression in mammography: pressure distribution patterns. *Acta Radiologica*, 53(9):973–980. 77
- Dustler, M., Andersson, I., Fornvik, D., and Tingberg, A. (2012b). The effect of breast positioning on breast compression in mammography: a pressure distribution perspective. In *Medical Imaging 2012: Physics of Medical Imaging*, volume 8313, page 83134M. International Society for Optics and Photonics. 83, 84
- Eder, M., Raith, S., Jalali, J., Volf, A., Settles, M., Machens, H.-G., and Kovacs, L. (2014). Comparison of Different Material Models to Simulate 3-D Breast Deformations Using Finite Element Analysis. *Annals of Biomedical Engineering*, 42(4):843–857. 45, 46
- Eiben, B., Lacher, R., Vavourakis, V., Hipwell, J. H., Stoyanov, D., Williams, N. R., Sabczynski, J., Bülow, T., Kutra, D., Meetz, K., et al. (2016a). Breast conserving surgery outcome prediction: A patient-specific, integrated multi-modal imaging and mechano-biological modelling framework. In *International Workshop on Digital Mammography*, pages 274–281. Springer. 45
- Eiben, B., Vavourakis, V., Hipwell, J. H., Kabus, S., Buelow, T., Lorenz, C., Mertzanidou, T., Reis, S., Williams, N. R., Keshtgar, M., and Hawkes, D. J. (2016b). Symmetric Biomechanically Guided Prone-to-Supine Breast Image Registration. *Annals of Biomedical Engineering*, 44(1):154–173. 43
- Eiben, B., Vavourakis, V., Hipwell, J. H., Kabus, S., Lorenz, C., Buelow, T., and Hawkes, D. J. (2014). Breast deformation modelling: comparison of methods to obtain a patient specific unloaded configuration. *Proc. SPIE*, 9036:903615–8. 44, 59
- Eiben, B., Vavourakis, V., Hipwell, J. H., Kabus, S., Lorenz, C., Buelow, T., Williams, N. R., Keshtgar, M., and Hawkes, D. J. (2016c). Surface driven biomechanical breast image registration. In *SPIE Medical Imaging*, pages 97860W–97860W. International Society for Optics and Photonics. 43, 49, 50, 51

BIBLIOGRAPHY

- Fanelli, M. A., Vargas-Roig, L. M., Gago, F. E., Tello, O., De Angelis, R. L., and Ciocca, D. R. (1996). Estrogen receptors, progesterone receptors, and cell proliferation in human breast cancer. *Breast cancer research and treatment*, 37(3):217–228. 15
- Feldman, A. G. (1986). Once more on the equilibrium-point hypothesis (λ model) for motor control. *Journal of motor behavior*, 18(1):17–54. 46
2595
- Fleming, P., O'Neill, S., Owens, M., Mooney, T., and Fitzpatrick, P. (2013). Intermittent attendance at breast cancer screening. *Journal of public health research*, 2(2). 19
- FNAH (2016). Cancer du sein : modalités spécifiques de dépistage pour les femmes haut risque. https://www.has-sante.fr/portail/jcms/c_1740821/fr/cancer-du-sein-modalites-specifiques-de-depistage-pour-les-femmes-a-haut-risque.
2600 16
- FRM (2017). Les chiffres du cancer du sein. <https://www.frm.org/cancer-du-sein/>. 15
- Fung, Y.-c. (2013). *Biomechanics: mechanical properties of living tissues*. Springer Science & Business Media. 63
2605
- Fung, Y.-c., Tong, P., and Chen, X. (2017). *Classical and computational solid mechanics*, volume 2. World Scientific Publishing Company. 58
- Gamage, T. P. B., Boyes, R., Rajagopal, V., Nielsen, P. M. F., and Nash, M. P. (2012). Modelling prone to supine breast deformation under gravity loading using heterogeneous finite element models. In Poul M.F. Nielsen, Adam Wittek, and Karol Miller, editors, *Computational Biomechanics for Medicine*, pages 29–38. Springer New York. 43, 47, 49, 51, 58, 63
2610
- Garcia, E., Oliver, A., Diaz, O., Diez, Y., Gubern-Merida, A., Marti, R., and Marti, J. (2017). Mapping 3d breast lesions from full-field digital mammograms using subject-specific finite element models. In *SPIE Medical Imaging*, pages 1013504–1013504. International Society for Optics and Photonics. 45, 51
2615
- Gaur, S., Dialani, V., Slanetz, P. J., and Eisenberg, R. L. (2013). Architectural distortion of the breast. *American Journal of Roentgenology*, 201(5):W662–W670. 17
- Geeraert, N., Klausza, R., Mullera, S., et al. (2012). Breast characteristics and dosimetric data in x-ray mammography a large sample worldwide survey. In *Bonn: IAEA conference*. Citeseer. 81
2620
- Gefen, A. (2003). The in vivo elastic properties of the plantar fascia during the contact phase of walking. *Foot & ankle international*, 24(3):238–244. 49
- Gefen, A. and Dilmoney, B. (2007). Mechanics of the normal woman's breast. *Technology and Health Care*, 15(4):259–271. 49, 87
2625

BIBLIOGRAPHY

- Gent, A. (1996). A new constitutive relation for rubber. *Rubber chemistry and technology*, 69(1):59–61. 70
- Gent, A. and Thomas, A. (1958). Forms for the stored (strain) energy function for vulcanized rubber. *Journal of Polymer Science Part A: Polymer Chemistry*, 28(118):625–628.
- 2630 31
- Georgii, J., Paetz, T., Harz, M., Stoecker, C., Rothgang, M., Colletta, J., Schilling, K., Schloozi-Vries, M., Mann, R. M., and Hahn, H. K. (2016). Simulation and visualization to support breast surgery planning. In *International Workshop on Digital Mammography*, pages 257–264. Springer. 43, 47, 48, 49, 51
- 2635 Govindjee, S. and Mihalic, P. A. (1998). Computational methods for inverse deformations in quasi-incompressible finite elasticity. *International Journal for Numerical Methods in Engineering*, 43(5):821–838. 44
- Griesenauer, R. H., Weis, J. A., Arlinghaus, L. R., Meszoely, I. M., and Miga, M. I. (2017). Breast tissue stiffness estimation for surgical guidance using gravity-induced excitation.
- 2640 *Physics in Medicine and Biology*, 62(12):4756. 47, 49, 58
- Groot, J. E. d., Branderhorst, W., Grimbergen, C. A., Heeten, G. J. d., and Broeders, M. J. (2015). Towards personalized compression in mammography: A comparison study between pressure- and force-standardization. *European Journal of Radiology*, 84(3):384–391. 74, 77, 78
- 2645 Hafslund, B. (2000). Mammography and the experience of pain and anxiety. *Radiography*, 6(4):269–272. 82
- Hammerstein, R. G., Miller, D. W., White, D. R., Ellen Masterson, M., Woodard, H. Q., and Laughlin, J. S. (1979). Absorbed radiation dose in mammography. *radiology*, 130(2):485–491. 80
- 2650 Han, L., Hipwell, J. H., Eiben, B., Barratt, D., Modat, M., Ourselin, S., and Hawkes, D. J. (2014). A nonlinear biomechanical model based registration method for aligning prone and supine mr breast images. *IEEE transactions on medical imaging*, 33(3):682–694. 45, 47, 48, 49, 50, 51, 58, 60, 87
- Han, L., year, J. H., Tanner, C., Taylor, Z., Mertzanidou, T., Jorge Cardoso, Sebastian Ourselin, and David J Hawkes (2012). Development of patient-specific biomechanical models for predicting large breast deformation. *Physics in Medicine and Biology*, 57(2):455–472. 43, 46, 47, 48, 87
- 2655 Helvie, M., Chan, H.-P., Adler, D., and Boyd, P. (1994). Breast thickness in routine mammograms: effect on image quality and radiation dose. *AJR. American journal of roentgenology*, 163(6):1371–1374. 78, 79

BIBLIOGRAPHY

- Hendriks, F., Brokken, D., Oomens, C., Bader, D., and Baaijens, F. (2006). The relative contributions of different skin layers to the mechanical behavior of human skin in vivo using suction experiments. *Medical engineering & physics*, 28(3):259–266. 48
- 2665 Henrot, P., Leroux, A., Barlier, C., and Génin, P. (2014). Breast microcalcifications: the lesions in anatomical pathology. *Diagnostic and interventional imaging*, 95(2):141–152. 17
- Ho, T. K. (1995). Random decision forests. In *Document analysis and recognition, 1995., proceedings of the third international conference on*, volume 1, pages 278–282. IEEE. 54
- 2670 Hofvind, S., Geller, B., Skelly, J., and Vacek, P. (2012). Sensitivity and specificity of mammographic screening as practised in vermont and norway. *The British journal of radiology*, 85(1020):e1226–e1232. 18
- 2675 Hopp, T., Dietzel, M., Baltzer, P. A., Kreisel, P., Kaiser, W. A., Gemmeke, H., and Ruiter, N. V. (2013). Automatic multimodal 2d/3d breast image registration using biomechanical fem models and intensity-based optimization. *Medical image analysis*, 17(2):209–218. 63
- Huang, S.-Y., Boone, J. M., Yang, K., Packard, N. J., McKenney, S. E., Prionas, N. D., Lindfors, K. K., and Yaffe, M. J. (2011). The characterization of breast anatomical metrics using dedicated breast ct. *Medical physics*, 38(4):2180–2191. 11
- 2680 Huttenlocher, D. P., Klanderman, G. A., and Ruckridge, W. J. (1993). Comparing images using the hausdorff distance. *IEEE Transactions on pattern analysis and machine intelligence*, 15(9):850–863. 107
- Itoh, A., Ueno, E., Tohno, E., Kamma, H., Takahashi, H., Shiina, T., Yamakawa, M., and Matsumura, T. (2006). Breast disease: clinical application of us elastography for diagnosis. *Radiology*, 239(2):341–350. 18
- 2685 Kaliske, M. and Rothert, H. (1997). On the finite element implementation of rubber-like materials at finite strains. *Engineering Computations*, 14(2):216–232. 70, 88
- Kanitakis, J. (2002). Anatomy, histology and immunohistochemistry of normal human skin. *European journal of dermatology: EJD*, 12(4):390–9. 11
- 2690 Keemers-Gels, M., Groenendijk, R., Van Den Heuvel, J., Boetes, C., Peer, P., and Wobbes, T. (2000). Pain experienced by women attending breast cancer screening. *Breast cancer research and treatment*, 60(3):235–240. 81, 82
- Kellner, A. L., Nelson, T. R., Cervino, L. I., and Boone, J. M. (2007). Simulation of mechanical compression of breast tissue. *IEEE Transactions on Biomedical Engineering*, 54(10):1885–1891. 43

BIBLIOGRAPHY

- 2695 Kemp Jacobsen, K., O'meara, E. S., Key, D., SM Buist, D., Kerlikowske, K., Vejborg, I., Sprague, B. L., and Lynge, E. (2015). Comparing sensitivity and specificity of screening mammography in the united states and denmark. *International journal of cancer*, 137(9):2198–2207. 18
- 2700 Kim, S. J., Moon, W. K., Cho, N., Cha, J. H., Kim, S. M., and Im, J.-G. (2006). Computer-aided detection in digital mammography: comparison of craniocaudal, mediolateral oblique, and mediolateral views. *Radiology*, 241(3):695–701. 74
- Ko, M.-S., Kim, H. H., Cha, J. H., Shin, H. J., Kim, J. H., and Kim, M. J. (2013). Dose reduction in automatic optimization parameter of full field digital mammography: Breast phantom study. *Journal of breast cancer*, 16(1):90–96. 79
- 2705 Kopans, D. B. (2007). *Breast imaging*. Lippincott Williams & Wilkins. 8, 9, 12, 13, 18
- Krouskop, T. A., Wheeler, T. M., Kallel, F., Garra, B. S., and Hall, T. (1998). Elastic moduli of breast and prostate tissues under compression. *Ultrasonic Imaging*, 20(4):260–274. 46, 47
- 2710 Kuhlmann, M., Fear, E., Ramirez-Serrano, A., and Federico, S. (2013). Mechanical model of the breast for the prediction of deformation during imaging. *Medical engineering \& physics*, 35(4):470–478. 44, 51
- Leong, H.-T., Ng, G. Y.-f., Leung, V. Y.-f., and Fu, S. N. (2013). Quantitative estimation of muscle shear elastic modulus of the upper trapezius with supersonic shear imaging during arm positioning. *PloS one*, 8(6):e67199. 48
- 2715 Lima, E., K. M. M., Júnior, J. F. S. C., de Albuquerque Pereira, W. C., and de Oliveira, L. F. (2018). Assessment of the mechanical properties of the muscle-tendon unit by supersonic shear wave imaging elastography: a review. *Ultrasonography*, 37(1):3. 48
- Lorenzen, J., Sinkus, R., Biesterfeldt, M., and Adam, G. (2003). Menstrual-cycle dependence of breast parenchyma elasticity: estimation with magnetic resonance elastography of breast tissue during the menstrual cycle. *Investigative radiology*, 38(4):236–240. 14, 46
- 2720 Martin, L. J. (2017). What causes breast cancer? <https://www.webmd.com/breast-cancer/guide/what-causes-breast-cancer>. 15
- Martínez-Martínez, F., Rupérez-Moreno, M., Martínez-Sober, M., Solves-Llorens, J., Lorente, D., Serrano-López, A., Martínez-Sanchis, S., Monserrat, C., and Martín-Guerrero, J. (2017). A finite element-based machine learning approach for modeling the mechanical behavior of the breast tissues under compression in real-time. *Computers in Biology and Medicine*, 90:116–124. 43, 45, 49
- 2725 McKenna, R. J. (1994). The abnormal mammogram radiographic findings, diagnostic options, pathology, and stage of cancer diagnosis. *Cancer*, 74(S1):244–255. 17

BIBLIOGRAPHY

- Mercer, C., Hogg, P., Lawson, R., Diffey, J., and Denton, E. (2013). Practitioner compression force variability in mammography: a preliminary study. *The British journal of radiology*, 86(1022):20110596. 76, 78
- Miller, D., Livingstone, V., and Herbison, P. (2008). Interventions for relieving the pain and discomfort of screening mammography. *Cochrane Database Syst Rev*, 1. 82, 83
- 2735 Mugea, T. T. and Shiffman, M. A. (2014). *Aesthetic Surgery of the Breast*. Springer. 9, 10, 12, 13, 60
- NCI (2012). Breast and adjacent lymph nodes, national cancer institute. <https://www.cancer.gov/publications/patient-education/wyntk-breast-cancer>. 14
- 2740 NHSBSP (2012). 2012 review of the uk breast screening programme. <http://www.cancerresearchuk.org/about-cancer/breast-cancer/screening/screening-2012-review>. 16
- Nordez, A. and Hug, F. (2010). Muscle shear elastic modulus measured using supersonic shear imaging is highly related to muscle activity level. *Journal of applied physiology*, 108(5):1389–1394. 46
- 2745 Obenauer, S., Luftner-Nagel, S., Von Heyden, D., Munzel, U., Baum, F., and Grabbe, E. (2002). Screen film vs full-field digital mammography: image quality, detectability and characterization of lesions. *European radiology*, 12(7):1697–1702. 78
- Ogden, R. W. (1972). Large deformation isotropic elasticity—on the correlation of theory and experiment for incompressible rubberlike solids. In *Proc. R. Soc. Lond. A*, volume 326, pages 565–584. The Royal Society. 32
- 2750 OLeary, D., Teape, A., Hammond, J., Rainford, L., and Grant, T. (2011). Compression force recommendations in mammography must be linked to image quality. In *Proceedings of the European Congress of Radiology*, pages 1–19. 80
- 2755 Olgun, D. Ç., Korkmazer, B., Kılıç, F., Dikici, A. S., Velidedeoglu, M., Aydoğan, F., Kantarci, F., and Yılmaz, M. H. (2014). Use of shear wave elastography to differentiate benign and malignant breast lesions. *Diagnostic and Interventional Radiology*, 20(3):239. 18
- Østerås, B. H., Skaane, P., Gullien, R., and Martinsen, A. C. T. (2018). Average glandular dose in paired digital mammography and digital breast tomosynthesis acquisitions in a population based screening program: effects of measuring breast density, air kerma and beam quality. *Physics in medicine and biology*. 81
- 2760 Palomar, A. P. d., Calvo, B., Herrero, J., Lpez, J., and Doblar, M. (2008). A finite element model to accurately predict real deformations of the breast. *Medical Engineering & Physics*, 30(9):1089–1097. 43, 44, 58

BIBLIOGRAPHY

- Pandya, S. and Moore, R. G. (2011). Breast development and anatomy. *Clinical obstetrics and gynecology*, 54(1):91–95. 14
- Patete, P., Iacono, M. I., Spadea, M. F., Trecate, G., Vergnaghi, D., Mainardi, L. T., and Baroni, G. (2013). A multi-tissue mass-spring model for computer assisted breast surgery. *Medical Engineering and Physics*, 35(1):47–53. 51
2770
- Pathmanathan, P., Gavaghan, D. J., Whiteley, J. P., Chapman, S. J., and Brady, J. M. (2008). Predicting tumor location by modeling the deformation of the breast. *IEEE Transactions on Biomedical Engineering*, 55(10):2471–2480. 44, 48, 49, 51
- Pechter, E. A. (1998). A new method for determining bra size and predicting postaugmentation breast size. *Plastic and reconstructive surgery*, 102(4):1259–1265. 9
2775
- Peipins, L. A., Shapiro, J. A., Bobo, J. K., and Berkowitz, Z. (2006). Impact of womens experiences during mammography on adherence to rescreening (united states). *Cancer causes & control*, 17(4):439–447. 81, 82
- Perry, N., Broeders, M., de Wolf, C., Törnberg, S., Holland, R., and von Karsa, L. (2008). European guidelines for quality assurance in breast cancer screening and diagnosis. summary document. *Annals of Oncology*, 19(4):614–622. 76
2780
- Peters, N. H., Borel Rinkes, I. H., Zuithoff, N. P., Mali, W. P., Moons, K. G., and Peeters, P. H. (2008). Meta-analysis of mr imaging in the diagnosis of breast lesions. *Radiology*, 246(1):116–124. 19
- Peto, R., Boreham, J., Clarke, M., Davies, C., and Beral, V. (2000). Uk and usa breast cancer deaths down 25% in year 2000 at ages 20–69 years. *The Lancet*, 355(9217):1822. 15
2785
- Pike, M. C., Spicer, D. V., Dahmoush, L., and Press, M. F. (1993). Estrogens progestogens normal breast cell proliferation and breast cancer risk. *Epidemiologic reviews*, 15(1):17–35. 15
2790
- Pilcher, L. S. (1917). The breast, its anomalies, its diseases and their treatment. *Annals of Surgery*, 65(4):527. 14
- Poulos, A., McLean, D., Rickard, M., and Heard, R. (2003). Breast compression in mammography: how much is enough? *Journal of Medical Imaging and Radiation Oncology*, 47(2):121–126. 2, 79, 81, 82
2795
- Rajagopal, V., Chung, J.-H., Highnam, R. P., Warren, R., Nielsen, P. M., and Martyn P. Nash (2010a). Mapping microcalcifications between 2d mammograms and 3d MRI using a biomechanical model of the breast. In Karol Miller and Poul M.F. Nielsen, editors, *Computational Biomechanics for Medicine*, pages 17–28. Springer. 47

BIBLIOGRAPHY

- 2800 Rajagopal, V. et al. (2007). *Modelling breast tissue mechanics under gravity loading*. PhD thesis, ResearchSpace@ Auckland. 51, 87
- Rajagopal, V., Lee, A., Chung, J.-H., Warren, R., Highnam, R. P., Nash, M. P., and Nielsen, P. M. (2008). Creating individual-specific biomechanical models of the breast for medical image analysis. *Academic Radiology*, 15(11):1425–1436. 44, 45, 46, 47, 49
- 2805 Rajagopal, V., Nielsen, P. M. F., and Nash, M. P. (2010b). Modeling breast biomechanics for multi-modal image analysis—successes and challenges. *Wiley Interdisciplinary Reviews: Systems Biology and Medicine*, 2(3):293–304. 45
- Riggio, E., Quattrone, P., and Nava, M. (2000). Anatomical study of the breast superficial fascial system: the inframammary fold unit. *European Journal of Plastic Surgery*, 23(6):310–315. 49
- 2810 Rivlin, R. S. and Saunders, D. (1951). Large elastic deformations of isotropic materials vii. experiments on the deformation of rubber. *Phil. Trans. R. Soc. Lond. A*, 243(865):251–288. 31
- Rohan, P.-Y., Lobos, C., Nazari, M. A., Perrier, P., and Payan, Y. (2014). Finite element modelling of nearly incompressible materials and volumetric locking: a case study. *Computer methods in biomechanics and biomedical engineering*, 17(sup1):192–193. 58
- Ruiter, N. V., Stotzka, R., MULLER, T.-O., Gemmeke, H., Reichenbach, J. R., and Kaiser, W. (2006). Model-based registration of x-ray mammograms and MR images of the female breast. *IEEE Transactions on Nuclear Science*, 53(1):204–211. 43, 58, 87
- 2820 Samani, A., Bishop, J., Yaffe, M. J., and Plewes, D. B. (2001). Biomechanical 3-d finite element modeling of the human breast using MRI data. *Medical Imaging, IEEE Transactions on*, 20(4):271–279. 46, 47
- Samani, A. and Plewes, D. (2004). A method to measure the hyperelastic parameters of ex vivo breast tissue samples. *Physics in Medicine and Biology*, 49(18):4395–4405. 47
- 2825 Samani, A., Zubovits, J., and Plewes, D. (2007). Elastic moduli of normal and pathological human breast tissues: an inversion-technique-based investigation of 169 samples. *Physics in medicine and biology*, 52(6):1565. 45
- Saunders, R. S. and Samei, E. (2008). The effect of breast compression on mass conspicuity in digital mammography. *Medical physics*, 35(10):4464–4473. 79, 82
- 2830 Shrestha, S. and Poulos, A. (2001). The effect of verbal information on the experience of discomfort in mammography. *Radiography*, 7(4):271–277. 82
- Sinkus, R., Tanter, M., Xydeas, T., Catheline, S., Bercoff, J., and Fink, M. (2005). Viscoelastic shear properties of in vivo breast lesions measured by mr elastography. *Magnetic resonance imaging*, 23(2):159–165. 47

BIBLIOGRAPHY

- 2835 Skandalakis, J. E. (2009). Embryology and anatomy of the breast. *Breast augmentation: principles and practice*. Springer, Berlin, 12. 8
- SPF (2016). Sante publique france: Cancer du sein. <http://invs.santepubliquefrance.fr/Dossiers-thematiques/Maladies-chroniques-et-traumatismes/Cancers/Donnees-par-localisation/Cancer-du-sein>. 15
- 2840 Sturgeon, G. M., Kiarashi, N., Lo, J. Y., Samei, E., and Segars, W. P. (2016). Finite-element modeling of compression and gravity on a population of breast phantoms for multimodality imaging simulation. *Medical Physics*, 43(5):2207–2217. 43, 44, 45, 49, 87
- Sutradhar, A. and Miller, M. J. (2013). In vivo measurement of breast skin elasticity and breast skin thickness. *Skin Research and Technology*, 19(1). 12, 48, 69
- 2845 Tabár, L., Vitak, B., Chen, H.-H. T., Yen, M.-F., Duffy, S. W., and Smith, R. A. (2001). Beyond randomized controlled trials. *Cancer*, 91(9):1724–1731. 16
- Tanner, C., Schnabel, J. A., Hill, D. L. G., Hawkes, D. J., Leach, M. O., and Hose, D. R. (2006). Factors influencing the accuracy of biomechanical breast models. *Medical Physics*, 33(6):1758. 45
- 2850 Treloar, L. (1943). The elasticity of a network of long-chain moleculesii. *Transactions of the Faraday Society*, 39:241–246. 31
- Ulger, H., Erdogan, N., Kumanlioglu, S., and Unur, E. (2003). Effect of age, breast size, menopausal and hormonal status on mammographic skin thickness. *Skin Research and Technology*, 9(3):284–289. 12
- 2855 Van Houten, E. E., Doyley, M. M., Kennedy, F. E., Weaver, J. B., and Paulsen, K. D. (2003). Initial in vivo experience with steady-state subzone-based mr elastography of the human breast. *Journal of magnetic resonance imaging*, 17(1):72–85. 47
- Vandeput, J. and Nelissen, M. (2002). Considerations on anthropometric measurements of the female breast. *Aesthetic plastic surgery*, 26(5):348–355. 10
- 2860 Vavourakis, V., Hipwell, J. H., and Hawkes, D. J. (2016). An inverse finite element u/p-formulation to predict the unloaded state of in vivo biological soft tissues. *Annals of biomedical engineering*, 44(1):187–201. 44
- Wellman, P., Howe, R. D., Dalton, E., and Kern, K. A. (1999). Breast tissue stiffness in compression is correlated to histological diagnosis. *Harvard BioRobotics Laboratory Technical Report*, pages 1–15. 45, 47
- 2865 Wenger, M. P., Bozec, L., Horton, M. A., and Mesquida, P. (2007). Mechanical properties of collagen fibrils. *Biophysical journal*, 93(4):1255–1263. 49

BIBLIOGRAPHY

- 2870 Whelehan, P., Evans, A., Wells, M., and MacGillivray, S. (2013). The effect of mammography pain on repeat participation in breast cancer screening: a systematic review. *The Breast*, 22(4):389–394. 19, 81
- Williams, M. B., Raghunathan, P., More, M. J., Seibert, J. A., Kwan, A., Lo, J. Y., Samei, E., Ranger, N. T., Fajardo, L. L., McGruder, A., et al. (2008). Optimization of exposure parameters in full field digital mammography. *Medical physics*, 35(6Part1):2414–2423. 79
- 2875 Williamson, A. and Hoggart, B. (2005). Pain: a review of three commonly used pain rating scales. *Journal of clinical nursing*, 14(7):798–804. 81, 82
- Yaffe, M., Boone, J., Packard, N., Alonzo-Proulx, O., Huang, S.-Y., Peressotti, C., Al-Mayah, A., and Brock, K. (2009). The myth of the 50-50 breast. *Medical physics*, 36(12):5437–5443. 11
- 2880 Yeoh, O. (1990). Characterization of elastic properties of carbon-black-filled rubber vulcanizates. *Rubber chemistry and technology*, 63(5):792–805. 32
- Youk, J. H., Gweon, H. M., and Son, E. J. (2017). Shear-wave elastography in breast ultrasonography: the state of the art. *Ultrasonography*, 36(4):300. 18
- 2885 Yushkevich, P. A., Piven, J., Cody Hazlett, H., Gimpel Smith, R., Ho, S., Gee, J. C., and Gerig, G. (2006). User-guided 3D active contour segmentation of anatomical structures: Significantly improved efficiency and reliability. *Neuroimage*, 31(3):1116–1128. 54
- Zajac, F. E. (1989). Muscle and tendon properties models scaling and application to biomechanics and motor. *Critical reviews in biomedical engineering*, 17(4):359–411. 46